The Evolution of Dislocation Density in a Higher-order Continuum Theory of Dislocation Plasticity

Stefan Sandfeld

A thesis submitted for the degree of Doctor of Philosophy.
The University of Edinburgh.
March 2010

Abstract

The growing demand for physically motivated continuum theories of plasticity has led to an increased effort on dislocation based field descriptions. Only recently rigorous techniques have been developed by T. Hochrainer for performing meaningful averages over systems of moving, curved dislocations, which can be described by a higher order dislocation density tensor. Within this thesis we rewrite this continuum theory of dislocations using exclusively standard vector and tensor calculus. This formulation is much more accessible (although still defined in a higher order configuration space) than the original formulation which uses differential forms and higher order currents. This formulation then serves as the starting point for the numerical exploration of the continuum theory where we cover simple benchmark problems, which allow for verification with analytical solutions. This already demonstrates that within this theory it is possible to predict dislocation kinematics, which cannot be predicted by classical methods based e.g. on the 'Kröner-Nye tensor'. After this verification we then apply our numerical implementation to a complex example: bending of a thin film in a double slip configuration, which yields most interesting results concerning the general concept of 'geometrically necessary' and 'statistically stored' dislocations. Another most important outcome is that nearly all important kinematic properties of single dislocation lines are still contained and numerically accessible within this averaged continuum description.

While we were pursuing the numerical exploration of the theory within this thesis, T. Hochrainer further developed his continuum theory towards a formulation which under certain simplifying assumptions does not require the higher order configuration space. This is extremely beneficial from point of view of computational cost and stability. A significant part of this thesis is concerned with verifying this simplified variant with the original formulation. The result is that in many physically relevant cases both theories yield very similar if not identical results.

In the third part of the thesis we tackle the problem of dislocation dynamics within the continuum description. We propose a suitable method for computing stresses based on the fact that a dislocation causes eigenstrain in an elastic continuum and demonstrate its versatility and applicability with examples.

Acknowledgements

I would like to express my gratitude to my supervisor at the University of Edinburgh, Prof. Michael Zaiser, whose support and guidance over the past four years were invaluable to me and the project. His expertise and patience to discuss my work with me have truly broadened my understanding of materials science and physics.

A very special thanks to Dr. Thomas Hochrainer. His 'Continuum Dislocation Dynamics Theory' provided a most interesting topic for my thesis and I consider it a special honor to be part of the theory's development group. Discussions with him have always been most interesting, enjoyable and enlightening.

This work was done in cooperation with the Karlsruhe Institute of Technology, Germany, which funded more than half of my PhD project. I would like to thank Prof. Peter Gumbsch (Institut für Zuverlässigkeit von Bauteilen und Systemen, izbs) for offering this possibility, for very interesting and helpful discussions and for providing such an inspiring work environment.

All of them I am most grateful for teaching me science and how to put these thoughts into words. It is very precious to me that they introduced me to the scientific community and made it possible that I could present my work at international conferences and meetings.

I would like to acknowledge the financial support of the European Union under the RTN SizeDepEn (MRTN-CT-2003-504634).

Thank-you to my friends and my colleagues in Edinburgh and Karlsruhe and - last but not least - to my dear family for being so very supportive and understanding all the time.

Contents

List of figures

Acronyms and abbreviations

The following acronyms are used:

CCT	classical continuum theory (Kröner)
CDD	Continuum Dislocation Dynamics (Hochrainer)
sCDD	simplified version of CDD
SSD	statistically stored dislocations
GND	geometrically necessary dislocations
DDD	discrete dislocation dynamics
FE	finite element
FEM	finite element method

The following superscripts are used:

$^{\mathrm{d}}$	indicating a *discrete* object (as opposed to a continuous object)
$^{\mathrm{pl}}$	plastic
$^{\mathrm{el}}$	elastic
$^{\mathrm{s}}$	number of slip plane
$^{\mathrm{mf}}$	mean field
$^{\mathrm{y}}$	yield
$^{\mathrm{b}}$	back stress
$^{\mathrm{l}}$	line tension

The following subscripts are used to denote the point of evaluation of e.g. a function:

$_{(\boldsymbol{r},\varphi)}$	point in the configuration space
$_{(\boldsymbol{r})}$	spatial point / spatial component of a point in the configuration space
$_{(\varphi)}$	line orientation / orientational component of a point in the configuration space

Nomenclature

a	nondimensional constant in Taylor relationship
$\boldsymbol{b}$	Burgers vector
b	modulus of the Burgers vector
B	drag coefficient
$\boldsymbol{c}$	spatial curve
$\boldsymbol{C}$	lifted curve
D	nondimensional constant for back stress
$\boldsymbol{e}_1, \boldsymbol{e}_2, \boldsymbol{e}_3$	canonical unit vectors
G	shear modulus
h	film height, height of a (subvolume of a) crystal
$\boldsymbol{J}$	dislocation current
k	mean curavture
l	length of inclined slip plane (bending)
$\boldsymbol{l}$	(average) dislocation line direction
$\boldsymbol{L}$	generalised tangent
$L_{\boldsymbol{c}}$	length of a curve $\boldsymbol{c}$
M	bending moment
$\boldsymbol{n}$	(glide plane) normal vector
r, R	radius
$\boldsymbol{r}$	distance vector
$\boldsymbol{s}$	line direction of a single dislocation line
s	arc length of a curve
$\mathcal{S}$	area
$t, \Delta t$	time, discrete time step
T	line tension force
$\boldsymbol{u}$	displacement
v	scalar velocity (in general)
$\boldsymbol{v}$	vector of scalar velocity
$v_{(r,\varphi)}$	scalar velocity (in the configuration space)
w	width of a boundary layer

$\boldsymbol{V}$	generalised velocity
x, y, z	cartesian coordinates
χ	anisotropy factor for velocity
$\boldsymbol{\alpha}$	Kröner-Nye tensor
$\boldsymbol{\alpha}^{\mathrm{II}}$	dislocation density tensor of second order
$\boldsymbol{\beta}$	distortion tensor
$\boldsymbol{\varepsilon}$	strain tensor
$\epsilon_{i,j,k}$	permutation symbol
γ	plastic slip
κ	geometrically necessary dislocation density
μ	shape factor for diffusion
ν	Poisson ratio
$\boldsymbol{\nu}$	unit normal to a curve
φ	angle of line orientation
ρ	scalar dislocation density in general
ρ_{G}	geometrically necessary dislocation density
ρ_{t}	total dislocation density
$\boldsymbol{\sigma}$	stress tensor
ϑ	rotational velocity
$\mathbb{C}$	tensor of elastic moduli
$\mathcal{M}^*$	projection tensor
$\mathcal{M}$	symmetric part of the projection tensor

Calculus notations

Throughout this thesis we use the following definitions and conventions:

Vectors and tensors are denoted by bold-face letters, whereas scalar quantities are written non-bold (e.g. $\boldsymbol{\alpha}$ as opposed to α).

Partial derivatives are abbreviated as $\partial_x(\cdot) := \frac{\partial(\cdot)}{\partial x}$, ∇ denotes the gradient operator and the divergence of a vector (tensor) field is written as div, curl denotes the curl-operator. Second partial derivatives are abbreviated by a double subscript $\partial_{xy}(\cdot) := \frac{\partial}{\partial x}\frac{\partial(\cdot)}{\partial y}$.

The vector product is denoted by $\times$. For double indices we assume the summation convention, if not stated otherwise. In $\boldsymbol{c} = \boldsymbol{a} \otimes \boldsymbol{b}$ the tensor product is denoted by $\otimes$; this operation reads for Cartesian coordinates in index notation $c_{ij} = a_i b_j$.

The symmetric part of a tensor $\boldsymbol{a}$ is denoted by $\operatorname{Sym} \boldsymbol{a} := \frac{1}{2}\left(\boldsymbol{a} + \boldsymbol{a}^T\right)$.

We denote the twofold derivative in direction of the vector $\boldsymbol{L}$ by $\nabla^2_{\boldsymbol{L}}(v)$, where v is a scalar.

Part I

Introduction and Foundations

Chapter 1
Introduction

The history of processing metals can be traced back until earlier than 5000 BC. Ever since these days man has deepened his understanding how to process metals (by e.g. forging) in order to obtain tools or weapons of ever increasing quality. However, the physical mechanisms underlying the empirical procedures could not be understood until the advent of the first 'materials scientists' in the 19th century: among them Willard Gibbs, who demonstrated that mechanical properties of metals are closely related to the thermodynamical properties of their atomic structure. This direction was followed in the early 20th century by Rutherford, who performed his famous backscattering experiment on a thin gold foil and thereby gave birth to a method which is still used for crystallographic imaging.

Up to then it was assumed that plastic deformation necessarily implies an amorphous structure, or at least the amorphisation of a material. Comparison of diffraction images of undeformed and plastically deformed metals however revealed that plastic deformation leaves the crystal lattice structure unchanged. As a consequence one had to discard the idea of 'plastic amorphisation'. Instead, the observation that the diffraction image is the same before and after plastic deformation gave rise to the idea that plastic deformation occurs by shifting lattice planes by discrete lattice vectors only: crystals deform by crystallographic slip. Attempts to explain the discrepancy between the theoretically predicted shear strength of a metal and the experimentally observed yield stresses lead to the concept of the 'dislocation' - a line-like defect inside a perfect crystal - which was proposed in the 1930s independently by Orowan (1934), Polanyi (1934) and Taylor (1934).

Quite simultaneously with Gibbs' discovery of the relationship between thermodynamics and mechanical properties of materials and also during the early 19th century, Navier developed the general theory of elasticity, which was further elaborated by Stokes, Cauchy and Poisson. Their theories were formulated in terms of an elastic *continuum*, which, if subjected to applied forces, responds with a continuous stress-strain state. In the very same spirit, Tresca, de St. Venant et al., and later in the early 20th century also von Mises (1913) extended the elastic continuum by introducing phenomenological relations to account for the observed plastic behavior of metals and described phenomena such as yielding and work hardening.

The two different approaches for predicting plastic deformation of crystalline materials - the discrete approach of condensed matter physics and the continuous approach of phenomenological plasticity theories - developed side-by-side until the 1950s when Kondo (1952), Nye (1953), Bilby *et al.* (1955) and Kröner (1958) independently formulated the classical continuum theory of dislocations. The fundamental quality of their theory is a second-rank dislocation density tensor (in the following denoted as Kröner-Nye tensor). This tensor was supposed to serve as a measure for the average plastic deformation state of a crystal and thus to link the microscopically discontinuous to a macroscopically continuous deformation state. But already the authors were well aware that the Kröner-Nye tensor only captures some aspects of plastic deformation processes (inhomogeneous deformation states associated with so-called geometrically necessary dislocations) and does not account for others (the accumulation of so-called statistically stored dislocations in homogeneous plasticity). This renders the classical dislocation density measure problematic as a foundation for a continuum theory of plasticity; it is however the first attempt to bridge the gap between the atomistic discontinuity and the macroscopic continuity of plastic deformation.

Nonetheless, dislocation-based plasticity theories have been formulated which are explicitly or implicitly based upon the classical dislocation density measure. Such theories, as for instance formulated by Acharya and co-workers (Acharya, 2001, 2003; Varadhan *et al.*, 2006) and by Sedláček and co-workers (Sedláček *et al.*, 2003; Sedláček & Werner, 2004), apply to particular situations where all dislocations are 'geometrically necessary'. In more general situations, using the classical dislocation density tensor as the basis of a plasticity theory leads to non-closed formulations which need to be 'patched up' by phenomenological assumptions. These issues are discussed in detail in Section 3.3.

Phenomenological continuum plasticity theories, on the other hand, have been very successful in a wide range of engineering applications. They operate on length scales where the properties of materials and systems are scale invariant. It is for example possible to measure the mechanical behaviour of a millimeter-sized specimen in order to predict the behaviour of a steel bridge with a length of hundred meters. This scale-invariance however breaks down at very small dimensions, say e.g. a few microns, which is a scale of growing importance due to the increasing miniaturization of medical and electronic devices. The influence of characteristic length scales of the material micro-structure becomes pronounced in small systems, giving rise to so-called 'size effects' (e.g., Ashby, 1970; Arzt, 1998), as observed in various experiments such as the micro bending of thin beams (Stolken & Evans, 1998) and thin wires (Fleck *et al.*, 1994). Phenomenological continuum theories incorporate internal length scales by introducing strain gradient terms - sometimes based on the consideration of 'geometrically necessary' dislocation densities - into their constitutive equations (e.g., Fleck *et al.*, 1994; Nix & Gao, 1998; Gurtin, 2002; Gao & Huang, 2003). Models which combine the evolution of scalar densities of so-called statistically stored with the consideration of geometrically necessary dislocations (e.g., Gao *et al.*, 1999; Ma *et al.*, 2006, and references therein) are also essentially phenomenological. Such models can be regarded as heuristic approaches towards formulating constitutive equations which allude to the physical mechanisms of dislocation microstructure evolution. However, the constitutive equations are not related to the evolution of a discrete dislocation system through systematic and mathematically meaningful averaging procedures, and the models therefore remain on the level of phenomenological expedients. For criticism of such theories, see e.g. Kubin & Mortensen (2003) and Zaiser & Aifantis (2003).

This gives rise to the question if (and how) a continuum theory of dislocations mediated plasticity can be based on physically sound assumptions and observations. Recent research in this field produced promising initial results, especially from the late 1990s on, when Groma and co-workers developed a statistical approach towards deriving not only the kinematic evolution of dislocation systems, but also their internal interactions and stress driven dynamics, from systematic averages over ensembles of discrete dislocation systems (Groma, 1997; Zaiser *et al.*, 2001; Groma *et al.*, 2003; Kratochvíl & Sedláček, 2008). This approach draws heavily on averaging techniques used in the statistical mechanics of interacting particle systems. It is therefore restricted to simplified systems of straight edge dislocations, which can be imagined as two-dimensional systems of point particles in the intersecting plane. In an average representation, these systems can be described in terms of densities of charged particles ('positive' and 'negative' dislocations distinguished by the two possible orientations of the line direction with respect to the Burgers vector). It is, however, not obvious how to generalise these methods to three-dimensional systems of connected dislocation lines, since the line-like nature of the dislocations and the continuous distribution of dislocation line directions need to be accounted for.

Already Kosevich (1979) proposed a description of three-dimensional dislocation systems in terms of higher-dimensional density measures by defining dislocation densities in a space which includes as independent variables parameters that characterise the line orientation. In the context of dislocation dynamics, a similar approach was used in El-Azab's pioneering work (El-Azab, 2000), which extended the methods of statistical mechanics to systems of curved dislocation lines by using densities that evolve in a higher dimensional state space. However, while taking into account the orientation of line segments, both Kosevich and El-Azab did not directly account for the local connectivity of the segments.

Only recently, the mathematical foundations required for transferring the methods of statistical mechanics consistently to three-dimensional systems of curved dislocations have been formulated by Hochrainer's 'Continuum Dislocation Dynamics Theory' (CDD) (see e.g. Hochrainer *et al.*, 2007). This theory relies on a geometrical description of dislocation lines and their averages, i.e. line densities, which uses the methods and formalisms of differential geometry. The theory is a direct generalisation of Kröner's classical continuum theory, which is contained as a special case. Within this theory the common distinction between 'geometrical necessary' and 'statistically stored' dislocation becomes dispensable.

Within the present thesis we reformulate this theory using exclusively standard vector calculus and explore it numerically in order to validate it and estimate the applicability towards physically meaningful problems.

The structure of the thesis is the following:

- In the first part of this thesis, Chapter 2 is dedicated to an overview over and introduction into general dislocation theory and crystal plasticity, where we briefly introduce fundamental definitions and physical relations which are used throughout this thesis. Since Kröner's classical continuum theory (CCT) is the predecessor of CDD we introduce his theory to the reader in Chapter 3 in some detail. In particular, we rewrite CCT in a form which is suitable for comparison with CDD and subsequently elucidate the limitations of CCT.
- The second part of this thesis treats Hochrainer's Continuum Dislocation Dynamics theory. In Chapter 4 we rewrite the formulation of CDD using exclusively standard vector and tensor calculus - contrary to the original formulation which was strongly based on the mathematical tools of differential forms and higher order currents. This formulation is much more accessible (although still defined in a higher order configuration space) than the original formulation. This serves as the starting point for the

numerical exploration of the continuum theory (Chapter 5) where we cover simple benchmark problems, which allow for verification with analytical solutions. These examples already demonstrate that within this theory it is possible to predict dislocation kinematics, which cannot be predicted by classical methods based e.g. on the 'Kröner-Nye tensor'. After this verification we then apply our numerical implementation in Chapter 6 to a complex example: bending of a thin film in a double slip configuration, which yields most interesting results concerning the general concept of 'geometrically necessary' and 'statistically stored' dislocations. Another most important outcome is that nearly all important kinematic properties of single dislocation lines are still contained and numerically accessible within this averaged continuum description.

- While we were pursuing the numerical exploration of the theory within this thesis, Thomas Hochrainer further developed his continuum theory towards a formulation which under certain simplifying assumptions - does not require the higher order configuration space. This is extremely beneficial from point of view of computational cost and stability. The third part of this thesis is concerned with verifying this simplified variant against the original formulation of CDD. Therefore, in Chapter 7 we derive sCDD in terms of quantities that can be compared with those used in CDD. We show by an analytical comparison with Radan Sedláček's continuum theory of dislocations that a special case of Hochrainer's simplified theory is equivalent to Sedláček's formulation. In Chapter 8 we compare CDD and sCDD using numerical test cases. The result is that in many physically relevant cases both theories yield very similar if not identical results.
- In the fourth part of the thesis we tackle the problem of dislocation dynamics within the continuum description. Therefore, we elucidate the problem of dynamical closure in a continuum context in Chapter 9. In Chapter 10 we propose a suitable method for computing stresses based on the fact that a dislocation causes eigenstrain in an elastic continuum and demonstrate its versatility and applicability with examples. In particular the 'coarse-graining' of discrete dislocations required to obtain dislocation densities is investigated with this method in Chapter 11.

Chapter 2
Dislocations and plasticity

This chapter gives an overview over observations and basic physical properties of dislocations. This is not a complete introduction; such can be found in various text books as e.g. Cottrell (1961); Hull & Bacon (2002); Hirth & Lothe (1982); Weertmann & Weertman (1982).

2.1 The concept of the dislocation

Many physical and mechanical properties of crystalline materials are strongly influenced by defects in the crystal lattice. In general, defects can be of dimension 0 (point defects), 1 (line defects), 2 (planar defects) and 3 (volume defects). In many cases one of the most important class of defects is the dislocation.

Dislocations in an elastic continuum Even before materials scientists began to ponder about dislocations in crystals Volterra (1907) and Love (1927) explored the properties of line singularities in a continuous elastic body. To create a line singularity in an elastic continuum they used the following construction: Introduce a cut along an arbitrary bounded surface into the body, displace the cut planes with respect to each other by a constant vector and finally 'glue' them back together. Volterra called this construction a 'dislocation' (cf. Fig. 2.1), where the boundary of the cut becomes (after displacement of the cut surfaces) a dislocation line. For the resulting internal stress state he could derive an analytical solution, which also holds for the stress field of the line-like defect inside a crystal outside a 'core' with size of a few lattice constants around the singular line. The cut line contained within the crystal defines the dislocation unit line vector $\boldsymbol{l}$ and the surface displacement defines the Burgers vector $\boldsymbol{b}$ which will be discussed later in more detail.

Dislocations inside a crystal When the dislocation *inside a crystal* was discovered (or rather postulated - it had not been observed until then) this was done to close the gap be-

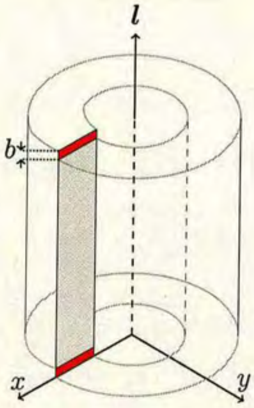

Figure 2.1: *Creation of a screw dislocation by a 'Volterra cut' and subsequent displacement of the cut faces*

tween the experimentally observed yield stresses of real crystals and the theoretically predicted stresses that would be required to slide two planes of atoms over each other in an ideal lattice: the latter was firstly calculated by Frenkel in 1926 and turned out to be several orders of magnitude higher than the experimentally observed yield stress. Orowan (1934), Polanyi (1934) and Taylor (1934) independently explained this discrepancy by the concept of the dislocation, in particular the *edge dislocation*, which is one of two fundamental dislocation types. It was not before the early 1950s, though, that dislocations were observed experimentally.

Dislocation types There are two fundamental types of dislocations both of which involve a characteristic distortion of the originally perfect crystal in particular regions. The 'center' of those regions is called the 'dislocation core' and defines the dislocation line. In all other places, the perfect crystal structure is preserved. Depending on the deformation state w.r.t. to the dislocation line one gets either a screw dislocation - atoms are shifted parallel to the line direction - or an edge dislocation - the direction of displacement is perpendicular to the line (Fig. 2.2). An additional visualisation of the relative displacement of atoms above and below the plane within which the dislocation is contained is shown in Fig. 2.3(a) and Fig. 2.3(b).

For all angles in between parallel and perpendicular to the line direction the dislocation has mixed screw and edge character, which is the case when dislocations form closed loops. Then there are sequences of pure edge – mixed edge/screw – pure screw dislocations etc with smooth transitions in between. Fig. 2.3(c) gives a visualization.

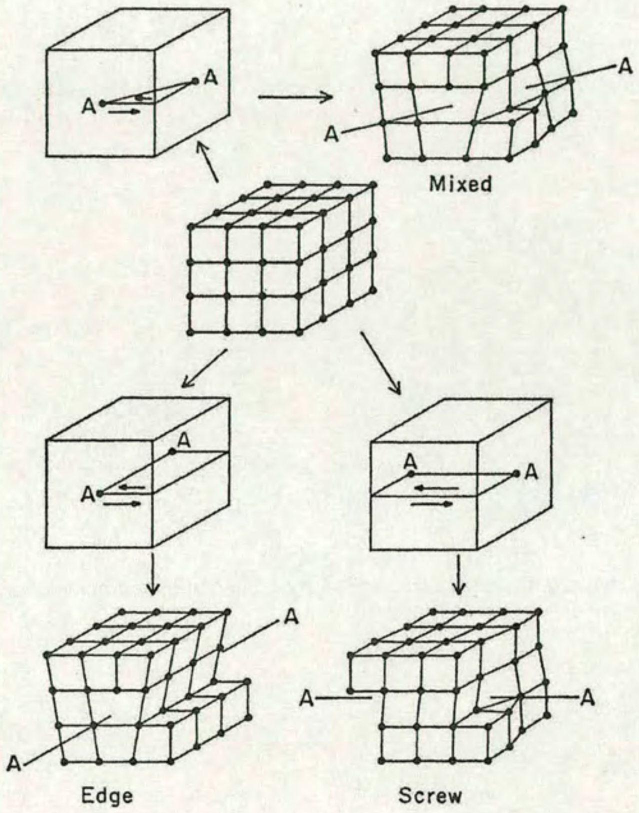

Figure 2.2: *Dislocation line direction for screw and edge dislocation. The dislocation line is given by the line A-A (Weertmann & Weertman, 1982)*

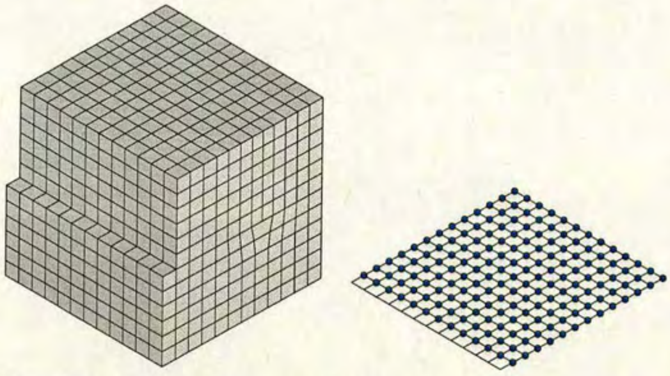

(a) An edge dislocation entered the crystal at the left side and is now located at the center. This leaves the upper half of the crystal 'dislocated' w.r.t. to the lower half.

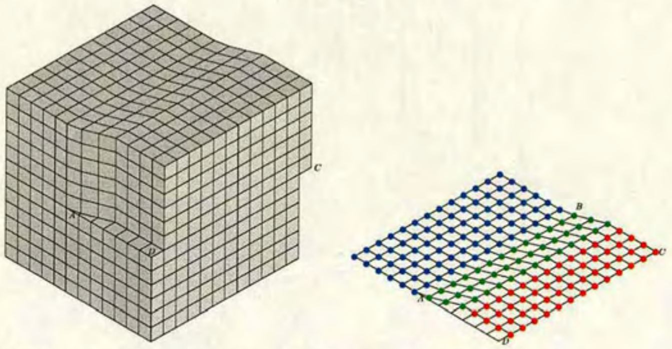

(b) A screw dislocation entered the crystal and is located in the center of the crystal (line A-B).

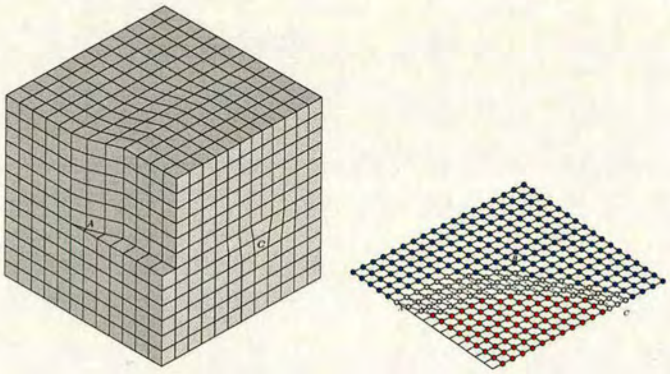

(c) A segment of a dislocation loop consisting of mixed edge and screw components: C: edge, A: screw, B: mixed.

Figure 2.3: *Dislocation types. The pictures on the left visualise the crystal lattice whereas the pictures on the left show the atoms in the plane within which the dislocation is contained.*

2.2 Burgers circuit, Burgers vector and plastic slip

Burgers circuit/Burgers vector To fully characterise a dislocation it is necessary to introduce the *Burgers circuit*. The Burgers circuit is a closed path around a dislocation. If the same path (i.e. with the same number of inter-atomic steps) is done in a perfect crystal it would not become a closed circuit. The *Burgers vector* $\boldsymbol{b}$ closes the gap and points from the end point of the circuit to its beginning.

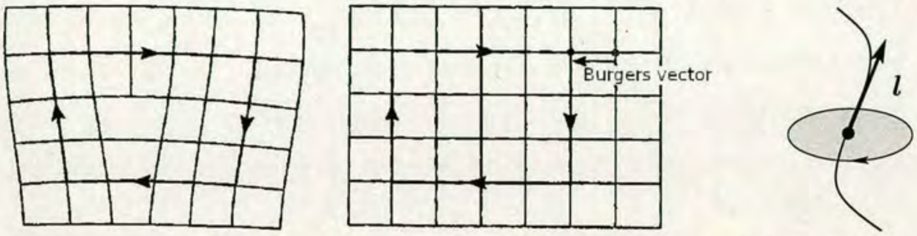

(a) Burgers circuit around an edge dislocation.

(b) The same Burgers circuit (i.e. with the same number of inter atomic steps) as in Fig.2.4(a) but in a perfect crystal. The vector required to close the circuit is the Burgers vector $\boldsymbol{b}$.

(c) Definition of line tangent vector $\boldsymbol{l}$ follows the convention of Burgers circuit direction ('left hand rule')

Figure 2.4: *Definition of the Burgers vector and the line direction*

Obviously, the direction of the Burgers vector depends on the direction of the Burgers circuit. This can be chosen arbitrarily and is a matter of convention[1]. We will define the circuit direction w.r.t. the dislocation line tangent: the positive Burgers circuit direction is clockwise if the line tangent vector would come out of the paper plane (left hand rule), Fig. 2.4(c).

The above definitions fully define the Burgers vector in direction and magnitude. In particular for the direction it follows that the Burgers vector of an edge dislocation is necessarily perpendicular to the dislocation line direction ($\boldsymbol{b} \cdot \boldsymbol{l} = 0$), the Burgers vector of a screw dislocation is parallel to the dislocation line direction ($\boldsymbol{b} \cdot \boldsymbol{l} = \pm b$, where the sign depends on the direction of the screw). In fact, these properties can be used to define screw and edge dislocations.

Although the dislocation line can change its direction and has changing (possibly mixed) character it is important to notice that the Burgers vector of a dislocation line is conserved along the line.

---

[1] In fact, in the literature both directions can be found.

The slip plane and plastic deformation A dislocation can be envisaged as the boundary of an area on a lattice plane which has 'slipped' (i.e. been displaced with respect to the adjacent lattice plane) by one Burgers vector. As the dislocation moves through the crystal, the slipped area expands (or contracts), which implies a shear deformation of the crystal. We note that during motion the dislocation needs to break atomic bonds along a line only and not within a plane, which is energetically more favorable.

We only consider dislocation lines that stay within a *slip plane* during motion (the analogon is the Volterra cut plane). Other forms of movement (e.g. so-called climb) are not considered throughout this thesis. The slip plane is spanned by the Burgers vector and the dislocation line direction. If dislocations move by glide only, this plane is a unique plane of the crystal lattice.

If a dislocation traverses the boundary of the crystal a slip step stays behind (Fig. 2.5). The surface step caused on entering and exiting has the magnitude of the Burgers vector $b = |\boldsymbol{b}|$.

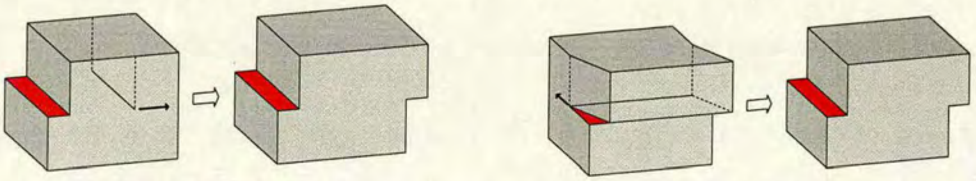

(a) edge dislocation

(b) screw dislocation

Figure 2.5: *Plastic deformation after an edge and screw dislocation moved through the crystal. The direction of movement of a edge/screw dislocation is perpendicular to the line direction. The direction of movement is indicated by the little arrow.*

These quantities can be used to define the plastic slip γ as

$$\gamma := \frac{b}{h}, \tag{2.1}$$

where h is the height of the crystal and b the width of the red area in Fig. 2.5. With this definition γ can be interpreted as the average plastic shear angle.

2.3 Small strain crystal plasticity

Leaving behind the length scale of discrete dislocations we now consider the continuum scale where one cannot distinguish between single dislocations anymore. Hence, we assume that the relevant physical quantities are continuous displacement fields, which evolve in a smooth manner in space and time.

Small-strain elasto-plasticity

The fundamental object of continuum elasto-plasticity is a smooth vector field of displacements $\boldsymbol{u}$. The gradient $\nabla \boldsymbol{u}$ is called the distortion tensor and is in the following denoted by $\boldsymbol{\beta}$:

$$\boldsymbol{\beta} := \nabla \boldsymbol{u}, \tag{2.2}$$

which describes the result of a compatible distortion[2]. The symmetric part of the distortion tensor in Eq. (2.2) is called the strain tensor $\boldsymbol{\varepsilon}$:

$$\boldsymbol{\varepsilon} := \mathrm{Sym}\, \boldsymbol{\beta} = \mathrm{Sym}\, \nabla \boldsymbol{u}. \tag{2.3}$$

In small-strain elasto-plasticity the distortion tensor is additively decomposed into a stress-free or plastic part $\boldsymbol{\beta}^{\mathrm{pl}}$ and an elastic part $\boldsymbol{\beta}^{\mathrm{el}}$. Accordingly, the strain is additively decomposed into

$$\boldsymbol{\varepsilon} = \boldsymbol{\varepsilon}^{\mathrm{el}} + \boldsymbol{\varepsilon}^{\mathrm{pl}} = \mathrm{Sym}\, \boldsymbol{\beta}^{\mathrm{el}} + \mathrm{Sym}\, \boldsymbol{\beta}^{\mathrm{pl}}. \tag{2.4}$$

The local stress $\boldsymbol{\sigma}$ is related to the elastic part of the strain tensor by the constitutive law

$$\boldsymbol{\sigma} = \mathbb{C} : \boldsymbol{\varepsilon}^{el} = \mathbb{C} : (\boldsymbol{\varepsilon} - \boldsymbol{\varepsilon}^{pl}), \tag{2.5}$$

where $\mathbb{C}$ denotes the fourth order tensor of elastic moduli and ':' the doubly contracted tensor product, in Cartesian coordinates $\sigma_{ij} = C_{ijkl}\varepsilon_{kl}^{el}$. To fully describe the elastic continuum the last equation is accompanied by balance equations for momentum and angular

---

[2] A deformation is called 'compatible' if the deformed body stays compact. This notion will be discussed in more detail in Section 3.1

momentum, which in the absence of body and inertial forces read

$$\operatorname{div}\boldsymbol{\sigma} = \mathbf{0} \quad \text{and} \quad \boldsymbol{\sigma} = \boldsymbol{\sigma}^{\mathrm{T}}, \tag{2.6}$$

respectively.

Crystallographic slip

As we consider dislocation glide only, plastic displacements occur within glide planes spanned by the dislocation line and Burgers vectors. A set of slip planes with common unit normal vector $\boldsymbol{n}$ and a Burgers vector $\boldsymbol{b}$ (normal to $\boldsymbol{n}$) define a *glide system.* The plastic distortion $\boldsymbol{\beta}^{\mathrm{pl}}$, if produced by dislocation glide, can be expressed as a sum over contributions from all active slip systems:

$$\boldsymbol{\beta}^{\mathrm{pl}} = \sum_{\mathrm{s}} \gamma_{\mathrm{s}} \mathcal{M}^{*}_{\mathrm{s}}, \quad \text{with} \quad \mathcal{M}^{*}_{\mathrm{s}} = \frac{1}{b}\left(\boldsymbol{n}_{\mathrm{s}} \otimes \boldsymbol{b}_{\mathrm{s}}\right), \tag{2.7}$$

where s denotes the number of the slip system (the summation convention does not apply for double indices there), γ_{s} is the plastic slip of the slip system, b is the modulus of the Burgers vector and $\mathcal{M}_{\mathrm{s}}$ is the symmetrised projection tensor accounting for the orientation of the slip system. Accordingly, the plastic strain $\boldsymbol{\varepsilon}^{\mathrm{pl}}$ is the symmetrised result of the accumulated plastic slip of each of those glide planes

$$\boldsymbol{\varepsilon}^{\mathrm{pl}} = \sum_{\mathrm{s}} \gamma_{\mathrm{s}} \mathcal{M}_{\mathrm{s}}, \quad \text{with} \quad \mathcal{M}_{\mathrm{s}} = \frac{1}{2b}\left(\boldsymbol{b}_{\mathrm{s}} \otimes \boldsymbol{n}_{\mathrm{s}} + \boldsymbol{n}_{\mathrm{s}} \otimes \boldsymbol{b}_{\mathrm{s}}\right). \tag{2.8}$$

The (average) plastic slip in a volume ΔV can be related to the area ΔF_{s} swept by dislocations of a given slip system: $\gamma_{\mathrm{s}} = \Delta F_{\mathrm{s}} b / \Delta v$, or in differential form: $\dot{\gamma}_{\mathrm{s}} = \rho b v$ where ρ is the dislocation line length per unit volume and v the (average) dislocation velocity.

Chapter 3

The classical continuum theory of dislocations

The purpose of constitutive modelling in plasticity theory is to derive evolution equations for the plastic distortion β^{pl} based on the current stress state and possibly various internal variables of the material. β^{pl} has a key role since it serves as the fundamental object characterising the mechanical response on the continuum level. An early attempt to link this with the dislocation picture of plasticity is Kröner's 'classical' continuum theory of dislocations (Kröner, 1958), in the following abbreviated by CCT. This theory is the predecessor of Hochrainer's Continuum Dislocation Dynamics theory, abbreviated by CDD, which we explore and apply within this thesis. To clarify why CDD is needed, we firstly introduce Kröner's theory along with some important notions.

3.1 The classical dislocation density tensor

The reason why one seeks to formulate a theory of the dynamics of dislocations in terms of density-like quantities as a measure of the dislocation state of a crystal is threefold: first, describing each dislocation inside a crystal separately quickly becomes extremely expensive from a computational point of view, while in the case of a density the number of represented objects does not have any influence on the computational cost. Second, a continuum theory of plasticity can - unlike discrete models of dislocation systems - be straightforwardly connected to a continuum description of the elastic stress and strain states, thus making the powerful tool of finite element calculation available for efficient computational modelling. Third, by basing such a theory on the actual physical processes of dislocation motion, one can hope to escape the arbitrariness of phenomenological guesswork which besets much of constitutive modelling in micro-plasticity. Defining such a density-like object requires some averaging, which occurs in the classical theory through considering the resulting Burgers vector of a set of dislocations: the net Burgers vector.

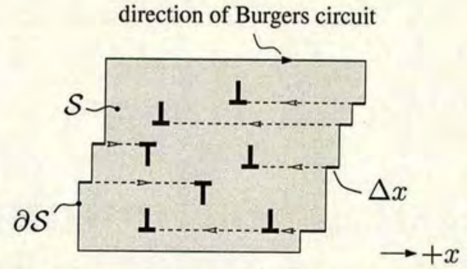

Figure 3.1: *Edge dislocations and a Burgers circuit: $\mathcal{S}$ denotes the area through which the dislocations thread and $\partial\mathcal{S}$ is the (closed) boundary. Each dislocation entering the volume leaves behind a (signed) surface step Δx_i.*

The net Burgers vector From the basic definition of the Burgers circuit the net Burgers vector of dislocations threading an area $\mathcal{S}$ (as in Fig. 3.1) can be evaluated as the integral of the plastic distortion over the boundary $\partial\mathcal{S}$

$$\boldsymbol{b} = \oint\limits_{\partial\mathcal{S}} \boldsymbol{\beta}^{\mathrm{pl}}\,\mathrm{d}s \quad \text{or} \quad b_j = \oint\limits_{\partial\mathcal{S}} c_i\beta^{\mathrm{pl}}_{ij}\,\mathrm{d}s, \tag{3.1}$$

where $\boldsymbol{c}$ is the tangent to the boundary curve with c_i the i-th component of $\boldsymbol{c}$. For the system in Fig. 3.1 for instance we then find $b = \sum\limits_i \Delta x_i = -5\Delta x + 2\Delta x = -3\Delta x$. To describe the dislocation state in $\mathcal{S}$ one may then introduce a dislocation density tensor $\boldsymbol{\alpha}$ which similarly measures the net Burgers vector flux through the area $\mathcal{S}$:

$$\boldsymbol{b} = \int\limits_{\mathcal{S}} \boldsymbol{\alpha}\boldsymbol{n}\,\mathrm{d}\mathcal{S} \quad \text{or} \quad b_j = \int\limits_{\mathcal{S}} \alpha_{ij}n_i\,\mathrm{d}\mathcal{S}, \tag{3.2}$$

with n_i the i-th component of the surface normal $\boldsymbol{n}$ of $\mathcal{S}$. From Eq. (3.1) and Eq. (3.2) it follows that

$$\boldsymbol{b} = \oint\limits_{\partial\mathcal{S}} \boldsymbol{\beta}^{\mathrm{pl}}\mathrm{d}s = \int\limits_{\mathcal{S}} \boldsymbol{\alpha}\boldsymbol{n}\,\mathrm{d}\mathcal{S}. \tag{3.3}$$

Applying Stokes' theorem we immediately get the fundamental equation

$$\boldsymbol{\alpha} = \operatorname{curl}\boldsymbol{\beta}^{\mathrm{pl}} \quad \text{or} \quad \alpha_{ij} = \epsilon_{ijk}\partial_{x_i}\beta^{\mathrm{pl}}_{kj}, \tag{3.4}$$

which Kröner (1958) used for defining the dislocation density tensor $\boldsymbol{\alpha}$. In Eq. (3.4), the curl operator acts on the first indices of a tensor in the same way as it acts on a vector, e.g $\alpha_{12} = \partial_{x_2}\beta^{\mathrm{pl}}_{32} - \partial_{x_3}\beta^{\mathrm{pl}}_{22}$. A different but equivalent definition - based on the lattice curvature - was given by Nye (1953). From the definition of the Kröner-Nye tensor Eq. (3.4) it immediately follows by the Gauss theorem for closed surfaces ∂S that

$$\operatorname{div} \boldsymbol{\alpha} = 0, \tag{3.5}$$

which reflects the physical fact that dislocations cannot start or end inside a crystal.

The notion of compatible distortions Alternatively, the Kröner-Nye tensor can be envisaged through the notion of 'compatibility' of distortions. Deformations are called 'compatible' if they distort the volume elements of a body in such a way that the body stays compact. For instance, imagine the crystal to consist of small volume elements. Then for example purely elastic deformations are compatible since they do not introduce internal discontinuities. Each compatible distortion $\boldsymbol{\beta}$ can be written as a gradient of the displacement field, $\nabla \boldsymbol{u}$. Hence, $\operatorname{curl} \nabla \boldsymbol{u}$ is always vanishing. An example for an incompatible deformation is the stress-free deformation state created by inhomogeneous shear along a set of parallel planes as shown in Fig. 3.2. Compatible distortions $\boldsymbol{\beta}$ in general are characterized by a vanishing curl ($\operatorname{curl} \boldsymbol{\beta} = 0$). While every purely elastic distortion is compatible, not every plastic distortion is incompatible; more details are given e.g. by Kröner (1958) and Kröner (1980). Kröners' definition of the dislocation density tensor Eq. (3.4) can now be considered from a different point of view: assume an incompatible plastic distortion $\boldsymbol{\beta}^{\mathrm{pl}}$ which necessitates an elastic distortion $\boldsymbol{\beta}^{\mathrm{el}}$ such that the body remains compact ($\operatorname{curl} \boldsymbol{\beta} = 0$). Then it is $\operatorname{curl} \boldsymbol{\beta}^{\mathrm{pl}} \neq 0$ (and also necessarily $\operatorname{curl} \boldsymbol{\beta}^{\mathrm{el}} \neq 0$). The deviation from zero, and thus Kröner's dislocation density tensor, measures the plastic incompatibility.

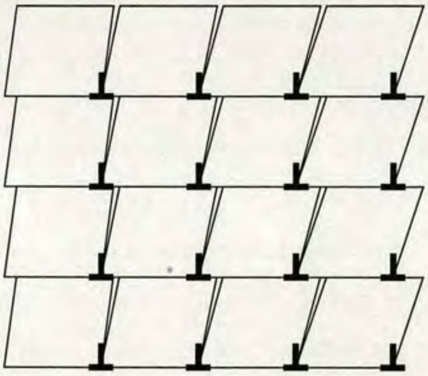

Figure 3.2: *A plastic distortion without elastic distortion may cause incompatible deformations such that the body is no longer compact. The gaps between the volume elements can be closed by introducing dislocations.*

When analyzing the information about the dislocation system that is contained in the Kröner-

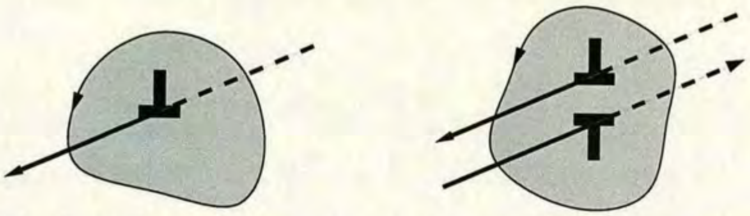

(a) only one 'geometrically necessary' dislocation

(b) a so-called dipole: two 'statistically stored' dislocations with opposite line direction

Figure 3.3: *Two systems of edge dislocations: Only in case 3.3(a) the Kröner-Nye tensor is not vanishing. In case 3.3(b) the two opposite oriented lines cause the net Burgers vector (and thus the Kröner-Nye tensor) to vanish.*

Nye tensor, it is important to specify the spatial resolution with which the plastic distortion is described. This is not always recognized in the literature, as the very concept of 'spatial resolution' seems odd when we are talking about a continuum theory. If in Fig. 3.3(b) the spatial resolution of a model is such that each of the two dislocations is resolved separately, we can use the Kröner-Nye tensor to describe the system. If the resolution is such that only the net Burgers vector is seen then the situation in Fig. 3.3(b) cannot be distinguished from an empty crystal. In order to understand the strengths and limitations of the classical continuum theory of dislocations it is indispensable to analyse how the information content expressed by the fundamental dislocation density measure changes as we move across scales. We start this analysis on the smallest scale on which a continuum theory can be used, i.e., we use continuous fields to describe the distortion of the crystal but assume that these fields are known with sufficient resolution such that individual dislocations can be 'seen' as singular lines.

3.2 Dislocation density tensor for a discrete dislocation system

If the spatial resolution of the theory is such that all dislocation lines are captured separately by the curl operation, the Kröner-Nye tensor completely characterises the dislocation system. In this case $\boldsymbol{\alpha}$ can be explicitly related to the configuration of the discrete dislocation lines. We envisage a dislocation line as an oriented curve $\boldsymbol{c}(s)$ which we assume to be parametrised by arc length s, i.e. $\mathrm{d}\boldsymbol{c}/\mathrm{d}s$ is the unit tangent vector to the dislocation line. Furthermore we assume that all dislocations share the same Burgers vector $\boldsymbol{b}$. In situations where dislocations of several slip systems are present, the following considerations hold for each slip system separately, and the total dislocation density tensor is obtained by summing over all slip systems.

We formally define a density measure along the dislocation line by

$$\delta_{\boldsymbol{c}}(\boldsymbol{r}) = \int_0^{L_c} \delta(\boldsymbol{c}(s) - \boldsymbol{r})\mathrm{d}s, \tag{3.6}$$

where $L_{\boldsymbol{c}}$ is the total length of curve $\boldsymbol{c}$ and $\delta(\boldsymbol{r})$ is the standard Dirac measure ('delta function') in three-dimensional space. Using this measure, we may write the discrete (indicated by superscript 'd') Kröner-Nye tensor as

$$\boldsymbol{\alpha}^{\mathrm{d}} = \sum_{\boldsymbol{c}} \delta_{\boldsymbol{c}} \frac{\mathrm{d}\boldsymbol{c}}{\mathrm{d}s} \otimes \boldsymbol{b}, \tag{3.7}$$

where the sum runs over all dislocation lines in the system. The local rate of plastic distortion is given by Orowan's relation which in tensorial form reads

$$\partial_t \boldsymbol{\beta}^{\mathrm{pl,d}} = -\sum_{\boldsymbol{c}} \delta_{\boldsymbol{c}}\, v\, \boldsymbol{n} \otimes \boldsymbol{b} = -\boldsymbol{v} \times \boldsymbol{\alpha}^{\mathrm{d}}. \tag{3.8}$$

Here, $\boldsymbol{v} = v\boldsymbol{\nu}$ is the local dislocation velocity, with v being the scalar velocity, and $\boldsymbol{\nu}$ the unit vector in the dislocation glide direction. In writing down (3.8), we used that the glide plane normal is given by $\boldsymbol{n} = \boldsymbol{\nu} \times \frac{\mathrm{d}\boldsymbol{c}}{\mathrm{d}s}$.

Defining the discrete dislocation current by

$$\boldsymbol{J}^{\mathrm{d}} = \boldsymbol{v} \times \boldsymbol{\alpha}^{\mathrm{d}} \tag{3.9}$$

$$= \sum_{\boldsymbol{c}} \boldsymbol{v} \times \delta_{\boldsymbol{c}} \frac{\mathrm{d}\boldsymbol{c}}{\mathrm{d}s} \otimes \boldsymbol{b} \tag{3.10}$$

and using the definition of the Kröner-Nye tensor yields a kinematically closed evolution equation[1] for $\boldsymbol{\alpha}^d$:

$$\partial_t \boldsymbol{\alpha}^{\mathrm{d}} = -\operatorname{curl} \boldsymbol{J}^{\mathrm{d}} = -\operatorname{curl}\left(\boldsymbol{v} \times \boldsymbol{\alpha}^{\mathrm{d}}\right). \tag{3.11}$$

We now attempt to use these relations for constructing a coarse-grained theory. In doing

---

[1] We speak of a kinematically closed equation as we assume the dislocation velocity $\boldsymbol{v}$ at this point to be a given quantity. In general, $\boldsymbol{v}$ is a function of the local stress, which in turn depends on the dislocation arrangement. Hence, a mathematically closed theory requires additional relationships between the dislocation state, as expressed by $\boldsymbol{\alpha}$, and the dislocation velocity $\boldsymbol{v}$. If v is a function of stress and line direction only, these relationships may be derived from Kröner's theory of eigenstresses (Kröner, 1958). The problem of closure will be discussed in more detail in Chapter 9.

so, we ask whether or not (and under which circumstances) direct coarse graining of the classical dislocation density measure leads to a loss of essential information.

3.3 Statistical averaging

We denote by $\langle(\dots)\rangle_{V,\boldsymbol{r}} := (1/V)\int\limits_{V_{\boldsymbol{r}}}(\dots)\mathrm{d}^3r$ the spatial average over some small volume $V_{\boldsymbol{r}}$ of size V centered at $\boldsymbol{r}$ (for convenience of notation, the subscripts V and $\boldsymbol{r}$ will be dropped in the following). A scalar measure of the average dislocation density is given by the dislocation line length within $V_{\boldsymbol{r}}$, divided by the averaging volume:

$$\begin{aligned}\rho_{\mathrm{t}} &= \frac{1}{V}\sum_{c}\int\limits_{c\cap V} 1\mathrm{d}s\\ &= \frac{1}{V}\sum_{c}\int\limits_{V}\int\limits_{0}^{L_c}\delta(\boldsymbol{c}(s)-\boldsymbol{r}')\mathrm{d}^3r'\mathrm{d}s = \left\langle\sum_{c}\delta_c\right\rangle.\end{aligned} \tag{3.12}$$

This measure characterises the *total dislocation density*. Similarly, we define the average dislocation density tensor by

$$\boldsymbol{\alpha} = \langle\boldsymbol{\alpha}^{\mathrm{d}}\rangle = \left\langle\sum_{c}\delta_{\boldsymbol{c}}\frac{\mathrm{d}\boldsymbol{c}}{\mathrm{d}s}\otimes\boldsymbol{b}\right\rangle, \tag{3.13}$$

The average line direction is given by the unit vector

$$\boldsymbol{l} = \frac{\langle\sum_{\boldsymbol{c}}\delta_{\boldsymbol{c}}\frac{\mathrm{d}\boldsymbol{c}}{\mathrm{d}s}\rangle}{\|\langle\sum_{\boldsymbol{c}}\delta_{\boldsymbol{c}}\frac{\mathrm{d}\boldsymbol{c}}{\mathrm{d}s}\rangle\|}, \tag{3.14}$$

and we define the *geometrically necessary dislocation density* ρ_{G} by

$$\rho_{\mathrm{G}} = \left\|\left\langle\sum_{c}\delta_{\boldsymbol{c}}\frac{\mathrm{d}\boldsymbol{c}}{\mathrm{d}s}\right\rangle\right\|. \tag{3.15}$$

The ratio $\rho_{\mathrm{G}}/\rho_{\mathrm{t}}$ is always smaller equal than 1 because of the triangular inequality. The average dislocation density tensor can be written in terms of ρ_{G} and $\boldsymbol{l}$ as

$$\boldsymbol{\alpha} = \rho_{\mathrm{G}}\boldsymbol{l}\otimes\boldsymbol{b}. \tag{3.16}$$

Here, the averaging volume may contain dislocations of all orientations. Hence, e.g. tangent vectors of dislocations with opposite directions will cancel out. In the extreme case of a purely statistically isotropic distribution all tangent vectors in an averaging volume cancel out. For the same reason, the average dislocation density tensor Eq. (3.16) does *not* fulfill the equation

$$\partial_t \boldsymbol{\beta}^{pl} = -\boldsymbol{v} \times \boldsymbol{\alpha}, \tag{3.17}$$

if we interpret $\boldsymbol{v}$ as the point wise vectorial average of the velocities along the dislocation lines.

By use of Eq. (3.8) together with averaging of Eq. (3.11), we can attempt to obtain an evolution equation for the averaged tensor. Writing this out, we obtain

$$\partial_t \boldsymbol{\alpha} = -\operatorname{curl}\left\langle \sum_{c} \delta_{c} \boldsymbol{v} \times \frac{\mathrm{d}c}{\mathrm{d}s} \otimes \boldsymbol{b} \right\rangle. \tag{3.18}$$

The threefold product within the average cannot directly be interpreted is terms of meaningful physical quantities. However, if, and only if, all dislocations within the averaging volume share the same tangent vector $\boldsymbol{l} = \mathrm{d}c/\mathrm{d}s$ and velocity $\boldsymbol{v}$ the average of the product can be written as a product of averages. This is possible either if only one dislocation is present (the discrete case) or if the dislocations form smooth line bundles. In these cases, $\rho = \rho_{\mathrm{G}}$, $\boldsymbol{\alpha} = \rho \boldsymbol{l} \otimes \boldsymbol{b}$, and Eq. (3.11) holds both on the local and on the averaged scale and we obtain the identity

$$\partial_t \boldsymbol{\alpha} = -\operatorname{curl}\left\langle \sum_{c} \delta_{c} \boldsymbol{v} \times \frac{\mathrm{d}c}{\mathrm{d}s} \otimes \boldsymbol{b} \right\rangle = -\operatorname{curl} \sum_{c} \left(\langle \delta_{c} \boldsymbol{v} \rangle \times \left\langle \frac{\mathrm{d}c}{\mathrm{d}s} \right\rangle \otimes \boldsymbol{b} \right). \tag{3.19}$$

In the general case, however, the averaging volume contains dislocations of different orientations. Thus, averaging leads to a reduced dislocation density $\rho_{\mathrm{G}} < \rho$, and the dislocation density tensor does not obey Eq. (3.11) with $\boldsymbol{v}$ understood as the average velocity. Instead, additional terms appear in the evolution equation. The necessity of accounting for such terms, which have the formal structure of correlators between the dislocation density and velocity/line direction, has been recognized in the literature (see e.g. Acharya *et al.* (2005)). However, the derivation and closure of a higher-order theory which properly accounts for such terms requires a formidable theoretical effort. Until now, published attempts either remain at the level of declarations-of-intention, or provide phenomenological patches which do not really resolve the underlying theoretical problems. We therefore pursue a different approach which generalises the classical dislocation density tensor such as to simplify the closure problem.

Part II

Continuum Dislocation Dynamics (CDD)

Chapter 4
Theoretical background of CDD

In Chapter 3 we introduced the classical continuum theory of dislocations which is based on the definition of the Kröner-Nye tensor. We concluded that this theory is not complete in the sense that only 'geometrically necessary' dislocations are considered. Furthermore, the notion of an average dislocation velocity turned out to be problematic. Recently, a proposal how to overcome these difficulties was made by Hochrainer, cf. e.g. Hochrainer (2006); Hochrainer *et al.* (2007). In the following we will refer to this theory as the 'Continuum Dislocation Dynamics theory', abbreviated CDD.

4.1 Introductory remarks

CDD distinguishes dislocation lines in a given spatial point $\boldsymbol{r}$ according to their line direction $\boldsymbol{l}$. As long as we are on the level of a discrete description, this is simply redundant. However, the physical rationale for this distinction becomes evident when we average over a mesoscopic volume: While it is in general unrealistic to assume that all dislocations contained in a mesoscopic volume have the same direction and move with the same velocity in response to an acting stress, it is much more realistic to assume that those dislocations which *do* have the same direction move in a similar manner.

If dislocations move by glide only, their motion is confined to a fixed glide plane and the line direction can be parametrised by a scalar variable, for instance the angle φ between line direction and Burgers vector. A point in configuration space is thus denoted by $(\boldsymbol{r}, \varphi)$, where $\boldsymbol{r}$ is a vector in the dislocation glide plane[1]. With regard to the numerical examples treated subsequently, we restrict ourselves to introducing CDD only for this situation. We note, however, that the theory is not restricted to this case but can be generalized to include out-of-plane dislocation motion and multiple slip systems (cf. Hochrainer *et al.* (2007)). This would however necessitate the use of CDD in its original formulation, which draws heavily on the use of differential geometry and especially on differential forms and currents.

---

[1] The theory may depend parametrically on the coordinate perpendicular to the glide plane. Such a parametric dependence does not change the equation of motion and is in the following omitted

In the following sections we rewrite Hochrainer's theory for the afore mentioned special case of dislocations moving by glide, where it can be formulated using standard vector and tensor calculus.

4.2 Definition of the second order dislocation density tensor

To define the dislocation density tensor and its averages in the three-dimensional (recall $(\boldsymbol{r}, \varphi)$) configuration space we proceed in close analogy to the classical theory. Unlike in the classical case, however, we consider averages over so-called lifts of dislocation lines to the configuration space instead of averages over the spatial dislocation lines themselves. In order to introduce the concept of lifted curves we define a coordinate system such that the 1-direction points into the direction of the Burgers vector and the glide plane is spanned by the 1- and 2-directions. To each point $\boldsymbol{c}(s) = (c^1(s), c^2(s))$ of a dislocation line we assign the angle φ between the tangent $\mathrm{d}\boldsymbol{c}/\mathrm{d}s$ and the Burgers vector, that is

$$\varphi(s) = \arctan\left(\frac{\frac{\mathrm{d}c^2}{\mathrm{d}s}}{\frac{\mathrm{d}c^1}{\mathrm{d}s}}\right). \tag{4.1}$$

We define the lift $\boldsymbol{C}$ of a given planar curve $\boldsymbol{c}$ to a three dimensional configuration space as

$$\boldsymbol{C}(s) = (C^1(s), C^2(s), C^3(s)) := (c^1(s), c^2(s), \varphi(s)). \tag{4.2}$$

Figure 4.1 gives a visualisation of this concept. We note that the tangent to the lifted curve,

$$\frac{\mathrm{d}\boldsymbol{C}}{\mathrm{d}s} = \left(\frac{\mathrm{d}c^1}{\mathrm{d}s}, \frac{\mathrm{d}c^2}{\mathrm{d}s}, \frac{\mathrm{d}\varphi}{\mathrm{d}s}\right) = \left(\frac{\mathrm{d}\boldsymbol{c}}{\mathrm{d}s}, k(s)\right), \tag{4.3}$$

contains as third coordinate the curvature $k(s)$ of the curve at $\boldsymbol{c}(s)$. As a consequence of this implicit definition of a metric the lifted curves $\boldsymbol{C}$ are *not* parametrised by arc length in the configuration space[2].

By transferring the definition of $\delta_{\boldsymbol{c}}$ to the lifted curve $\boldsymbol{C}$ as

$$\delta_{\boldsymbol{C}}(\boldsymbol{r}) = \int_{\boldsymbol{C}} \delta(\boldsymbol{C}(s) - (\boldsymbol{r}, \varphi))\mathrm{d}s, \tag{4.4}$$

---

[2] It is worth noting that the definition of the second order dislocation density tensor does not necessarily require a metric or volume element. However, an invariant definition requires the use of advanced mathematical concepts as e.g. differential forms. We refrain from introducing these concepts in this thesis and refer the interested reader to Hochrainer *et al.* (2007) and especially Hochrainer (2006) for a more thorough treatment.

we define the averaged dislocation density tensor of second order in complete analogy to the classical one (cf. Eq. (3.7)) as

$$\alpha^{\mathrm{II}}_{(r,\varphi)} = \left\langle \sum_{C} \delta_C \frac{\mathrm{d}C}{\mathrm{d}s} \otimes \boldsymbol{b} \right\rangle . \tag{4.5}$$

The sum is again taken over all dislocations in the system, and the averages are taken over a volume element in configuration space which is centered at $\boldsymbol{r}$ and φ.

It is illustrative to express also $\boldsymbol{\alpha}^{\mathrm{II}}$ as the product of a density function $\rho_{(r,\varphi)}$ and a generalised tangent which we denote by $\boldsymbol{L}_{(r,\varphi)}$. The definition of these two objects is not completely analogous to the classical ones. The density function is defined as

$$\rho_{(r,\varphi)} = \left\| \left\langle \sum_{C} \delta_C \frac{\mathrm{d}C}{\mathrm{d}s} \right\rangle \right\|_r , \tag{4.6}$$

where $\| \cdot \|_r$ measures the length of the spatial projection of a vector in the configuration space. The tangents to the lifted curves have the property

$$\left\| \frac{\mathrm{d}C}{\mathrm{d}s} \right\|_r = \left\| \frac{\mathrm{d}c}{\mathrm{d}s} \right\| = 1. \tag{4.7}$$

In Eq. (4.6), the averaging volume - a volume element in configuration space - contains dislocations of one orientation only. Hence, there is no cancellation - e.g. of dislocations of opposite directions - during averaging of the spatial tangent vectors. Therefore, the norm $\| \cdot \|_r$ may be interchanged with the averaging. We thus find that $\rho_{(r,\varphi)}$ gives the spatial line length per volume (of the configuration space) of dislocations at $\boldsymbol{r}$ with direction $\boldsymbol{l}(\varphi) = (\cos\varphi, \sin\varphi)$. The generalised tangent is defined as

$$\boldsymbol{L}_{(r,\varphi)} = \frac{\left\langle \sum_{C} \delta_C \frac{\mathrm{d}C}{\mathrm{d}s} \right\rangle}{\rho_{(r,\varphi)}} . \tag{4.8}$$

We note that the first two components of $\boldsymbol{L}_{(r,\varphi)}$ are just the canonical spatial direction at φ and the third component contains the average curvature $k_{(r,\varphi)}$, that is

$$\boldsymbol{L}_{(r,\varphi)} = (\cos\varphi, \sin\varphi, k_{(r,\varphi)}) = (\boldsymbol{l}(\varphi), k_{(r,\varphi)}). \tag{4.9}$$

From the definitions (Eq. (4.5)), (Eq. (4.6)) and (Eq. (4.8)) we easily find

$$\boldsymbol{\alpha}^{\mathrm{II}}_{(r,\varphi)} = \rho_{(r,\varphi)} \boldsymbol{L}_{(r,\varphi)} \otimes \boldsymbol{b}. \tag{4.10}$$

The averaged classical dislocation density tensor α can be evaluated from the density function $\rho_{(r,\varphi)}$ as

$$\boldsymbol{\alpha}_{(r)} = \int\limits_{0}^{2\pi} \rho_{(r,\varphi)} \boldsymbol{l}_{(\varphi)}) \,\mathrm{d}\varphi \otimes \boldsymbol{b} \tag{4.11}$$

and reads - explicitly stating the coefficient matrix:

$$\boldsymbol{\alpha}_{(r)} = \begin{pmatrix} b^1 \int\limits_0^{2\pi} \rho_{(r,\varphi)} \cos\varphi \,\mathrm{d}\varphi & b^2 \int\limits_0^{2\pi} \rho_{(r,\varphi)} \cos\varphi \,\mathrm{d}\varphi \\ b^1 \int\limits_0^{2\pi} \rho_{(r,\varphi)} \sin\varphi \,\mathrm{d}\varphi & b^2 \int\limits_0^{2\pi} \rho_{(r,\varphi)} \sin\varphi \,\mathrm{d}\varphi \end{pmatrix}. \tag{4.12}$$

$$\tag{4.13}$$

The second order dislocation density tensor may be represented by a 3×2 matrix which reads

$$\begin{aligned} \boldsymbol{\alpha}^{\mathrm{II}}_{(r,\varphi)} &= \rho_{(r,\varphi)} \begin{pmatrix} b^1 \cos\varphi & b^2 \cos\varphi \\ b^1 \sin\varphi & b^2 \sin\varphi \\ b^1 k_{(r,\varphi)} & b^2 k_{(r,\varphi)} \end{pmatrix} \\ &= \rho_{(r,\varphi)} \begin{pmatrix} \cos\varphi & 0 \\ \sin\varphi & 0 \\ k_{(r,\varphi)} & 0 \end{pmatrix} b, \end{aligned} \tag{4.14}$$

where the latter follows from the chosen coordinate system for which we took the 1-direction parallel to the Burgers vector and hence find $\boldsymbol{b} = (b, 0)$.

We remark that in analogy to Eq. (3.5) also the generalised divergence of $\boldsymbol{\alpha}^{\mathrm{II}}$ must vanish (cf. Hochrainer *et al.* (2007)), which likewise reflects the physical fact that dislocation lines do not start or end inside a crystal. With Eq. (4.14) this condition reads

$$\cos\varphi \partial_x \rho + \sin\varphi \partial_y \rho + \partial_\varphi (\rho k) = 0. \tag{4.15}$$

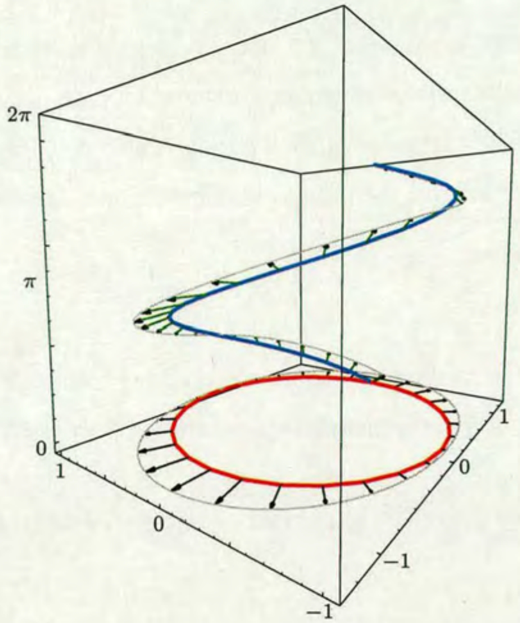

Figure 4.1: *Continuous lifted curve in the configuration space. The lower, closed loop is the spatial loop, the upper line is the 'lifted loop' with additional orientation information. The arrows attached to the lower loop indicate the spatial velocity, the arrows attached to the upper curve indicate the generalised velocity along the line. The rotational velocity ϑ is the vertical component of the generalised velocity.*

Finally, the total dislocation density ρ_t can be obtained from the scalar density by integration

$$\rho_t(x, y) = \int_0^{2\pi} \rho_{(r,\varphi)} \, \mathrm{d}\varphi. \tag{4.16}$$

4.3 The generalised dislocation velocity

In the preceding section we defined the dislocation density tensor α^{II} as an average of density functions characterising discrete lifted curves. In order to obtain the evolution of α^{II}, we need to consider the velocity of the lifted curves in the configuration space. As may be seen in Fig. 4.1 the velocity of a lifted curve contains, besides the spatial (horizontal) velocity $\boldsymbol{v}$ orthogonal to the spatial dislocation line, also a component in the φ direction which accounts for the rotation of line segments during dislocation motion.

It is straightforward to show that the pseudo-scalar rotation velocity ϑ of a moving curve parametrised by arc length s is determined by the change of velocity along the line. For the pseudo-scalars v, k and ϑ we use the following sign convention: We consider the pseudo-scalar velocity of a positively oriented loop as positive if the loop expands (compare Fig. 4.2). The curvature of such a loop is also considered as positive. From this sign convention it follows that the pseudo-scalar rotational velocity is

$$\vartheta(s) = -\frac{\mathrm{d}v(s)}{\mathrm{d}s}. \tag{4.17}$$

For a derivation of the explicit components of ϑ please refer to Appendix A. Using these conventions, we define the generalised velocity at a point $\boldsymbol{C}(s)$ of a lifted discrete curve as

$$\boldsymbol{V}^{\mathrm{d}}(s) = \big(v \sin\varphi(s), -v\cos\varphi(s), \vartheta(s)\big). \tag{4.18}$$

We note that unlike the spatial velocity, which is orthogonal to the dislocation line, the generalised velocity is in general not orthogonal to the lifted curve.

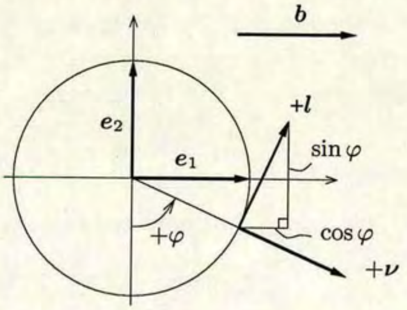

Figure 4.2: *Sign convention for the line orientation φ, tangent $\boldsymbol{l}$ and normal $\boldsymbol{\nu}$ on the parametrised unit circle*

The evolution of $\boldsymbol{\alpha}^{\mathrm{II}}$

In analogy with the classical definition, Eq. (3.10), we define the generalised (discrete) dislocation current

$$\boldsymbol{J}^{\mathrm{II,d}} = \sum_{C} \boldsymbol{V}^{\mathrm{d}} \times \delta_C \frac{\mathrm{d}\boldsymbol{C}}{\mathrm{d}s} \otimes \boldsymbol{b}. \tag{4.19}$$

The evolution of the averaged dislocation density tensor of second order is obtained in analogy to Eq. (3.18):

$$\partial_t \boldsymbol{\alpha}^{\mathrm{II}}_{(r,\varphi)} = -\operatorname{curl}\left\langle \boldsymbol{J}^{\mathrm{II,d}} \right\rangle_{(r,\varphi)}. \tag{4.20}$$

This equation differs from Eq. (3.18) describing the evolution of the classical dislocation density tensor because in Eq. (4.20) the average dislocation current Eq. (4.19) can be understood as a product of averages under much weaker assumptions regarding the dislocation configuration. The most important assumption in this respect is that nearby dislocations of the same line direction have the same curvature, which is reasonable in quasi-static situations, where the curvature essentially balances the local stress. Under this assumption, the average dislocation current can be written as

$$\boldsymbol{J}^{\mathrm{II}} = \boldsymbol{V}_{(r,\varphi)} \times \boldsymbol{\alpha}^{\mathrm{II}}_{(r,\varphi)}, \tag{4.21}$$

where the average velocity $\boldsymbol{V}_{(r,\varphi)} = \langle \boldsymbol{V}^{\mathrm{d}} \rangle$ can be expressed in terms of the average pseudo-scalar velocity $v_{(r,\varphi)} = \langle v \rangle$ and rotation velocity $\vartheta_{(r,\varphi)} = \langle \vartheta \rangle$ as

$$\boldsymbol{V}_{(r,\varphi)} = \left(v_{(r,\varphi)} \sin\varphi, -v_{(r,\varphi)} \cos\varphi, \vartheta_{(r,\varphi)} \right). \tag{4.22}$$

Consequently, the evolution equation for the dislocation density tensor of second order is obtained as

$$\partial_t \boldsymbol{\alpha}^{\mathrm{II}}_{(r,\varphi)} = -\operatorname{curl}\left(\boldsymbol{V}_{(r,\varphi)} \times \boldsymbol{\alpha}^{\mathrm{II}}_{(r,\varphi)} \right). \tag{4.23}$$

4.4 Evolution equations for the scalar field variables and plastic distortion

As we saw in Eq. (4.14), in the single glide situation under consideration, $\boldsymbol{\alpha}^{\mathrm{II}}$ is completely defined by the two scalar fields $\rho_{(r,\varphi)}$ and $k_{(r,\varphi)}$. Hence, the evolution equation for $\boldsymbol{\alpha}^{\mathrm{II}}$ can be formulated in terms of two coupled evolution equations for these functions. As the derivation of these evolution equations involves either abstract methods or simple but lengthy calculations we only give the result and refer the reader to Hochrainer *et al.* (2007) for details:

$$\partial_t \rho = -\left(\operatorname{div}(\rho \boldsymbol{v}) + \partial_\varphi(\rho\vartheta) \right) + \rho v k, \tag{4.24}$$

$$\partial_t k = -v k^2 - \nabla^2_{\boldsymbol{L}}(v) - \nabla_{\boldsymbol{V}}(k). \tag{4.25}$$

Here, $\nabla^2_{\boldsymbol{L}}$ and $\nabla_{\boldsymbol{V}}$ denote the second derivative along the generalised line direction and the first derivative along the generalised velocity direction, respectively. To avoid cumbersome notation we dropped the index ${}_{(r,\varphi)}$. In the following if no indices occur we always imply that all quantities are evaluated at the point $(\boldsymbol{r}, \varphi)$ in the configuration space $\mathbb{R} \times \mathbb{R} \times [0, 2\pi)$.

The transport terms in Eq. (4.24) can also be written by use of a 'generalised divergence' Div, which consists besides the spatial also of an angular component

$$\mathrm{Div}(\rho \boldsymbol{V}) := \mathrm{div}(\rho \boldsymbol{v}) + \partial_\varphi(\rho \vartheta). \tag{4.26}$$

The evolution equation for the plastic distortion $\boldsymbol{\beta}^{\mathrm{pl}}$ takes a similar form as Eq. (3.8) in the classical formulation:

$$\partial_t \boldsymbol{\beta}^{\mathrm{pl}} = \int_0^{2\pi} \rho_{(r,\varphi)} v_{(r,\varphi)} \mathrm{d}\varphi \; \boldsymbol{n} \otimes \boldsymbol{b}. \tag{4.27}$$

This quantity provides the link to the material response on the continuum level as introduced in Section 2.3. CDD is an example of a theory where the evolution of the plastic distortion $\boldsymbol{\beta}^{\mathrm{pl}}$ is expressed in terms of internal variables which represent statistical averages over the discrete dislocation pattern within the crystal.

Chapter 5

Exploration of the CDD Evolution Equations

In this section we explore the components of the evolution equations numerically by demonstrating the specific role of the different terms for various special cases. Although we do not aim to use the evolution equations for simulating the kinematic behaviour of discrete objects, it is crucial that discrete objects can be evolved properly: they serve as important testing cases to elucidate numerical problems that may occur in simulating arbitrary density distributions since they are (i) numerically challenging (the distributions studied are near-singular) and (ii) often simple analytical solutions can be obtained from directly analysing the dynamics of the singular lines. For these purposes only we investigate the evolution of quasi-discrete dislocations. We make several simplifying assumption; in particular we assume the dislocation velocity to be prescribed. Furthermore we do not consider interactions between dislocations. Thus, these systems should be considered as model systems only that serve to explore the kinematic consistency and numerical implementation of the CDD equations.

5.1 Numerical Implementation

Geometry

As in the preceding section we assume that all dislocations are moving on a single glide system with glide plane normal $\boldsymbol{n} = \boldsymbol{e}_3$ and Burgers vector $\boldsymbol{b} \equiv b\boldsymbol{e}_1$. The system is assumed homogeneous in the $\boldsymbol{e}_3$ direction, i.e., we consider a statistically homogeneous assembly of active glide planes.

Discretisation of the problem

We define a discrete time step $\Delta t := t^{i+1} - t^{i}$ with $i \in \mathbb{N}^{+}$. A forward Euler scheme is used for numerical time integration of the evolution equations. Hence, only values at step t^{i} are needed to compute the new values at step t^{i+1}; no additional history variables need to be stored. This is beneficial for the required computer memory, which is an issue as the multi-dimensional structure of the configuration space requires a large amount of information to be stored for multiple fields. Furthermore, we use a fixed mesh which demands a relatively fine space discretisation with corresponding large storage requirements.

The forward Euler time integration scheme is an unstable scheme which is only first order accurate and suffers from dispersion. Our main reason for using this scheme is that its simple explicit structure allows for an easy identification of the separate effects stemming from the different terms in the evolution equations. Implicit time integration schemes, on the other hand, require additional linearization steps along with the iterative solution of the resulting difference equations. It is then not straightforward to distinguish effects stemming e.g. from the discretisation, the initial values, the approximative nature of the Newton linearisation or the partial differential equations themselves. For the explicit Euler scheme used together with a compatible choice of numerical derivatives, we could identify a 'working regime' within which this integration method was numerically reliable and could be used to 'test' more fundamental aspects of the numerical implementation[1].

The 3-dimensional configuration space is discretised by a uniform mesh. It turned out that a resolution in the angular direction of in between 60 and 120 nodes is sufficient to discretise the density objects under consideration. In the case of quasi-discrete lines we use a discrete Gaussian distribution to approximate the Dirac delta function. Since we use a fine spatial resolution for this representation (e.g. about 60 nodes to discretise the part of the Gauss function which is $> 0.1\%$ of the peak value), dispersive effects can be neglected.

Derivatives w.r.t. the configuration space are approximated by finite differences. Derivatives which govern transport were approximated by an upwind scheme. This is a numerical scheme which uses information about the flow direction (e.g. the direction of propagation

---

[1] In our case, we pragmatically consider a numerical scheme to be well-behaved within the 'working regime' if a positive half-wave can be propagated for more than 10000 steps with a velocity $v = 1.0$, the mesh width $h = 1.0$ and a time step $\Delta t = 0.1$, such that the amplitude of spurious oscillations caused by the numerical scheme is negligible by comparison with the peak of the wave (e.g. less than 0.1% of the wave amplitude).

of a wave) to determine whether to use a forward or backward difference stencil, such that only information from upstream of the flow is used. Similar schemes are widely used to solve hyperbolic partial differential equations in computational fluid dynamics and reduce oscillations in direction of wave travel (see Harten (e.g. 1987))[2].

The upwind method based on first order forward and backward differences is oscillation-free but at the cost of a very strong 'smearing-out' effect in direction of wave travel caused by a large amount of 'numerical viscosity'. We therefore use a scheme based upon second order accurate forward and backward differences, which is of much better quality than the first order scheme but slightly oscillatory (Strikwerda, 2004). As a very simple remedy against the undershoot effect causing the oscillations, we cut off the (unphysical) negative density values and distribute this negative amount over all nodes with positive density. This procedure causes a steepening gradient on the downstream side of the wavefront and a slight increase of the wave's maximum - both of which are only minor effects in the cases we study.

All derivatives for nonconvective (e.g. diffusion) terms were approximated by central difference schemes of second order accuracy.

To determine the time step size we use the Courant-Friedrichs-Lewy condition (Morton, 1996)

$$\left| v\frac{\Delta t}{\Delta x} \right| \leq 1, \tag{5.1}$$

which serves as a (necessary) stability criterion for purely advective equations of the form

$$\partial_t \rho + v \partial_x \rho = 0 \tag{5.2}$$

that are solved by explicit time integration schemes such as the forward Euler scheme. In our simulations we accordingly choose $\Delta t \approx 0.1 \Delta x / \hat{v}$ where $\hat{v}$ is the largest occurring velocity.

---

[2] Alternative methods exist and have been used for similar problems: e.g. Roy & Acharya (2004) and Varadhan *et al.* (2006) use an explicit least-squares finite element formulation to solve their dislocation density transport problem. Schwarz (2007) uses a Lagrangian concept as a robust numerical method. In fluid dynamics and electro dynamics discontinuous Galerkin methods are used as conservative schemes. In our case, however, it is the coupling between the evolution equations for ρ and k which makes a straightforward application of the aforementioned methods difficult.

5.2 Test Cases

In this section we investigate several examples, all of which are simple enough such that we still can easily predict the outcome while exploring the CDD evolution equations. The first example treats a homogeneous distribution of circular loops. This case, which can be solved analytically, illustrates some basic properties of the theory. The second example treats a single quasi-discrete circular dislocation loop. This serves to illustrate and address issues related to the numerical discretisation of the system in a higher-dimensional configuration space. Thereafter, we elucidate the function and importance of the rotational velocity and its special role in the vicinity of impenetrable boundaries.

Homogeneous distribution of expanding loops

For a homogeneous distribution of equidistant loops with the same initial radius r_0 in an unbounded glide plane, all derivatives of ρ, k and v w.r.t. the configuration space vanish. Then the system of evolution equations Eq. (4.24) and Eq. (4.25) reduces to

$$\partial_t \rho = \rho v k, \tag{5.3}$$

$$\partial_t k = -v k^2. \tag{5.4}$$

Eq. (5.3) only consists of a production term, which yields the change of line length during expansion of the loops, while Eq. (5.4) governs the change of curvature $k(t) = 1/r(t)$ due to the expansion. Note that here ρ and v are independent of φ. Thus, we can directly obtain the evolution of the plastic distortion from Eq. (4.27) as

$$\partial_t \beta^{pl} = 2\pi \rho b v. \tag{5.5}$$

We could have obtained the same evolution equation for the curvature by considering the change of radius of a loop with initial radius r_0 which expands with the velocity v:

$$k = \frac{1}{r(t)} = \left(\frac{1}{k_0} + vt\right)^{-1} \tag{5.6}$$

$$\Rightarrow \partial_t k = -v \left(\frac{1}{k_0} + vt\right)^{-2} = -v k^2. \tag{5.7}$$

The evolution equation for the scalar density can then be obtained by considering homogeneously distributed loops with mean center-to-center spacing d and initial radius r_0. The density is the line length $2\pi r(t)$ per volume, i.e. in terms of k

$$\rho = \frac{2\pi}{k}\frac{1}{d^3}. \tag{5.8}$$

We obtain the evolution equation as time derivative of Eq. (5.8):

$$\partial_t \rho = \frac{2\pi}{d^3}\partial_t\left(\frac{1}{k}\right) = -\rho\frac{\partial_t k}{k} = \rho v k. \tag{5.9}$$

Hence, the case of a homogeneous distribution of equidistant, expanding or shrinking loops with the same initial radius is correctly represented by the theory.

This may seem a trivial example. However, an essential shortcoming of previously proposed continuum theories, such as those of Kosevich and El-Azab is manifested precisely by the fact that the kinematic behavior of a distribution of straight dislocation lines is not distinguished from that of a distribution of loops. CDD on the other hand reproduces the correct increase of line length for the evolving system of distributed loops, while for the case of the straight line distribution the theory yields pure advection without change in line length.

Quasi-discrete expanding circular loop

We again assume constant velocity and curvature such that there is no rotational velocity and no change of curvature along the line but this time we consider the evolution of a dislocation density distribution representing a *single* expanding loop (cf. Fig. 5.1(a)). As all derivatives of v and k are zero the evolution equations now simplify to

$$\partial_t \rho = -\operatorname{div}(\rho \boldsymbol{v}) + \rho v k, \tag{5.10}$$

$$\partial_t k = -v k^2. \tag{5.11}$$

The first part of the evolution equation for ρ governs spatial transport, whereas the second part accounts for changes in line length due to expansion or shrinkage of curved dislocation segments (here forming a circular loop). The change of curvature which goes along with the expansion or shrinkage of segments is determined by the evolution equation for k.

Numerical results: The problem of line fragmentation

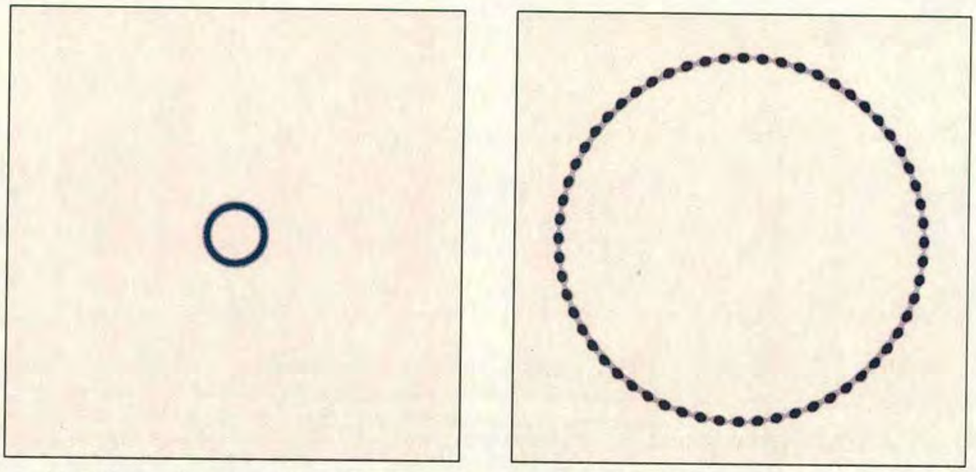

(a) Initial configuration ($R = 30$ nodes)

(b) Expanded loop after 3500 steps with $\Delta t = 0.1$ and $v = 1.0$ ($R = 3800$ nodes)

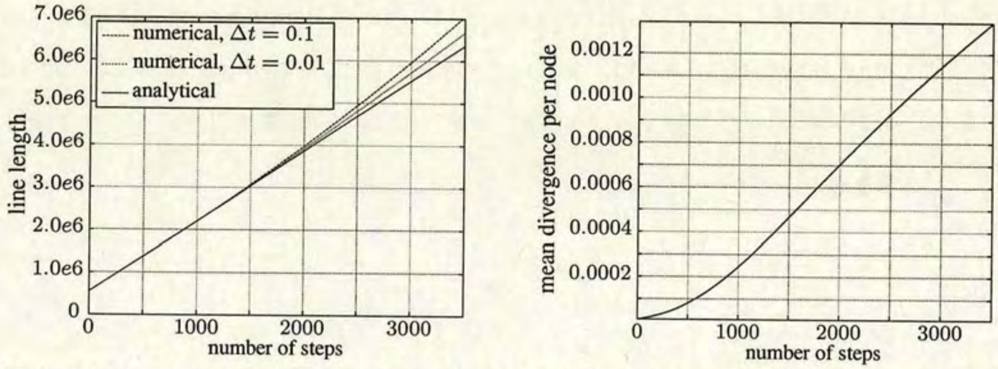

(c) Temporal evolution of the systems' total line length

(d) Temporal evolution of the mean divergence of $\boldsymbol{\alpha}^{\mathrm{II}}$ per node, $(1/N_{\mathrm{nodes}}) \sum || \operatorname{div} \boldsymbol{\alpha}^{\mathrm{II}} ||$

Figure 5.1: *Evolution of the (spatial) total dislocation density for an expanding loop as obtained from solving Eq. (5.10) and Eq. (5.11). The loop was discretised with 60 nodes in φ-direction: (a) initial configuration, (b) end configuration, (c) total amount of density integrated over the plane and analytical prediction, (d) evolution of the divergence of $\boldsymbol{\alpha}^{II}$.*

As an approximation to a discrete dislocation loop we generate a continuous density function by replacing the δ-distribution in Eq. (4.4) with a Gaussian distribution. The spatial projection of the initial distribution, that is the total dislocation density, is depicted in Fig. 5.1(a). Time integration of the evolution equations Eq. (5.10) and Eq. (5.11) leads to a spatial density distribution as shown in Fig. 5.1(b). The growth of the total dislocation line length, as expressed by the volume integral of the density function over the configuration space, is described correctly (Fig. 5.1(c)), except for a small deviation which is caused by discretisation errors. However, the density distribution gets spatially fragmented as the loop expands (Sandfeld *et al.*, 2009a). This fragmentation is directly related to a growing divergence of $\boldsymbol{\alpha}^{\mathrm{II}}$. As the time derivative of $\boldsymbol{\alpha}^{\mathrm{II}}$ is a curl (compare Eq. (4.23)) the evolution equations themselves conserve the solenoidality of $\boldsymbol{\alpha}^{\mathrm{II}}$. However, finite difference schemes in general can not guarantee that the discrete curl- and div- operators fulfill the relation $\operatorname{div}\operatorname{curl} = 0$. This shortcoming manifests itself in an strong increase of the mean divergence $(1/N_{\mathrm{nodes}})\sum \|\operatorname{div}\boldsymbol{\alpha}^{\mathrm{II}}\|$ as shown in Fig. 5.1(d). This increase mirrors the visible fragmentation of the dislocation density distribution during expansion of the loop. This fragmentation is unphysical. Moreover, in the case of inhomogeneous velocity fields the temporal evolution depends on derivatives of the density along the generalised line direction. The numerical evaluation of these derivatives becomes completely inaccurate if loop fragmentation becomes pronounced.

We note that other authors also have considered similar test problems, e.g. Sedláček and co-workers treated in Sedlacek *et al.* (2007) the problem of expansion of concentric dislocation loops. Additionally, we would like to remark that using polar coordinates would be advantageous for us in the sense that this would avoid fragmentation since density is being distributed properly due to the discretisation. On the other hand this approach can be used only for the special case of loops with the coordinate origin at their center, and not for the evolution of general distributions. The remainder of this section deals with generic strategies that avoid fragmentation within the framework of the chosen finite difference scheme.

Direct relaxation of the dislocation density tensor $\boldsymbol{\alpha}^{\mathrm{II}}$

A straightforward method to maintain solenoidality of the density distribution is to minimize the divergence of $\boldsymbol{\alpha}^{\mathrm{II}}$ by means of a sequence of 'relaxation' steps following each time step. This process ensures iteratively that $\operatorname{div}\boldsymbol{\alpha}^{\mathrm{II}}$ as a measure of fragmentation is kept below a given tolerance. We minimise the total divergence of $\boldsymbol{\alpha}^{\mathrm{II}}$ using the iteration formula

$$\boldsymbol{\alpha}^{\mathrm{II}}_{\mathrm{new}} \Leftarrow \boldsymbol{\alpha}^{\mathrm{II}}_{\mathrm{old}} + \lambda\operatorname{grad}\operatorname{div}(\boldsymbol{\alpha}^{\mathrm{II}}), \tag{5.12}$$

where λ is a factor controlling the step size, which can be adjusted to achieve efficient relaxation while avoiding 'overshoots'. However, this method has clear drawbacks: The operators $\operatorname{grad}\operatorname{div.}(\cdot)$ introduce second derivatives which have a diffusive effect and suppress fragmentation by homogenizing the dislocation density distribution along the dislocation line. However, the diffusive effect also acts in the perpendicular direction and causes a broadening of the line. Furthermore, the iteration scheme (Eq. (5.12)) conserves α^{II} and not ρ, causing unphysical changes in dislocation density during the relaxation step. An improved relaxation scheme which conserves the total density and avoids diffusive 'flattening' of the dislocation density distribution is obtained by modifying Eq. (5.12) such that ρ is relaxed only along the line:

$$\rho_{\text{new}} \Leftarrow \rho_{\text{old}} + \lambda \nabla_l^2 \rho, \tag{5.13}$$

where the relaxation is again carried out to minimize $\sum \| \operatorname{div} \boldsymbol{\alpha}^{\mathrm{II}} \|$.

Irrespective of the method used, relaxation of the system is computationally expensive. Achieving a well-relaxed configuration requires multiple relaxation steps, each of which is computationally about as expensive as one time integration step for the evolution equations. To obtain a computationally more efficient method for preserving solenoidality we take a closer look at the mechanism that leads to the fragmentation and devise a remedy which restores the unfragmented state without introducing an additional iterative process.

Correction of line fragmentation by tangential diffusion

To better understand loop fragmentation from a geometrical point of view, we consider a curved dislocation line in the configuration space (for simplicity we envisage a circular loop but the argument extends to any curved line). To obtain a continuous and differentiable density distribution we need to approximate the Dirac δ-function representing the discrete line in terms of continuous and differentiable functions. Doing this on a discrete grid amounts to a discrete convolution with an approximation function, i.e., we map (a subset of) $\mathbb{R}$ to (a subset of) $\mathbb{N}$. For poor resolution in φ-direction and a better resolution in x and y direction, Fig. 5.2 shows the density distribution obtained with Gaussian functions. It is important to realize that due to the mapping, each of the 'blobs' representing segments of the dislocation line is located on a particular φ-plane. As all points of the blob move into the same direction $\boldsymbol{v}$, which is perpendicular to the spatial line direction $\boldsymbol{l}(\varphi)$, the blobs are drifting apart during loop expansion and the line becomes fragmented.

We consider the effect of loop expansion at two successive time steps t^i and t^{i+1} and its impact on the change of arc length of a line segment s^i for the case of a continuous lifted loop and for a lifted loop with discretised orientations. Fig. 5.3 shows the geometrical

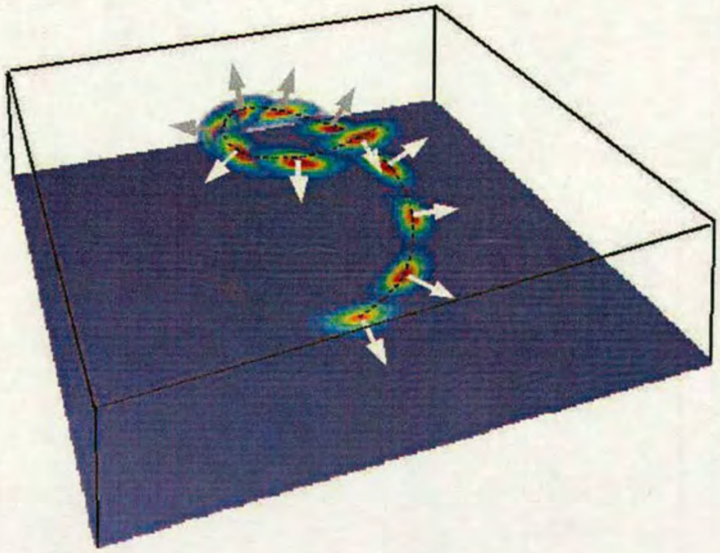

Figure 5.2: *Discrete density distribution which corresponds to a lifted line for a bad resolution in φ-direction (12 nodes only) chosen deliberately for demonstration purposes. Each of these blobs moves as a whole along the direction indicated by the arrows.*

relations between these two cases. To understand how the differences affect dislocation density evolution, we may then think of a single lifted line as a bundle of parallel lines with partial Burgers vectors and characterize the bundle by a space-dependent density ρ.

Let us first consider the expansion of a continuous lifted loop. As the loop expands in the spatial plane a circle segment s^i with cone angle $\Delta\varphi$ gets elongated to s^{i+1} (cf. Fig. 5.3(a)). Expressing this relation in terms of the curvature we get

$$k^i = \frac{\Delta\varphi}{s^i} \qquad \text{and} \qquad k^{i+1} = \frac{\Delta\varphi}{s^{i+1}}. \tag{5.14}$$

The increment of spatial arc length Δs from step i to step $i+1$ then is defined through

$$\Delta s := s^{i+1} - s^i = \Delta\varphi \left(\frac{1}{k^{i+1}} - \frac{1}{k^i} \right). \tag{5.15}$$

The arc length increase stems from the fact that the line orientation along the circle segment varies between $\varphi_0 - \frac{\Delta\varphi}{2}$ and $\varphi_0 + \frac{\Delta\varphi}{2}$, cf. Fig. 5.3(a), leading to divergent trajectories and a separation of the endpoints of the segment. For a bundle of lines, the local density within the bundle remains unchanged while the overall density increases as the bundle occupies more space.

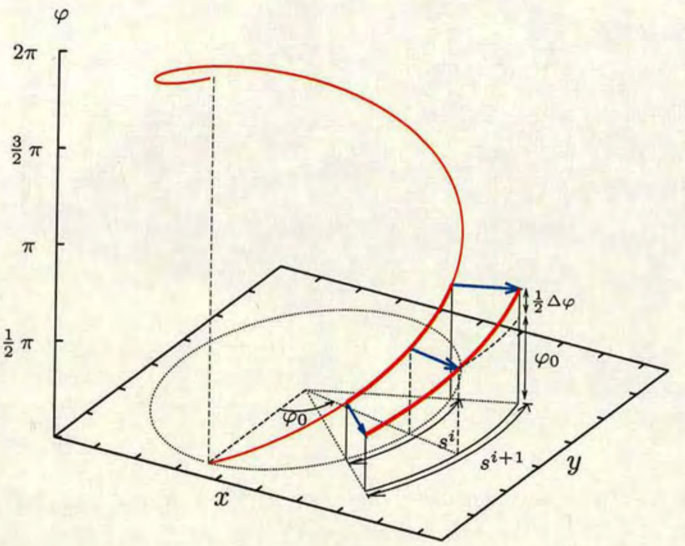

(a) line segment during ideal mathematical expansion of a lifted loop

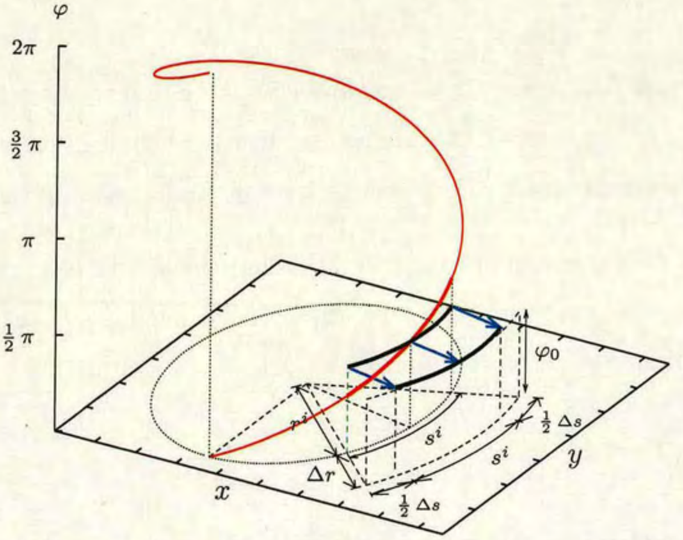

(b) line segment during numerically approximated lifted loop expansion

Figure 5.3: *Expansion of a continuous loop and the effect due to numerical discretisation: A lifted loop with radius r^i expands by Δr affecting the line inclination (the curvature) and its length. In the case of the continuous loop expansion the line segment gets rotated (by reduction of curvature) and stretched. The numerical scheme takes care of the rotation by an evolving curvature (not shown) but otherwise can only translate the segment without stretching.*

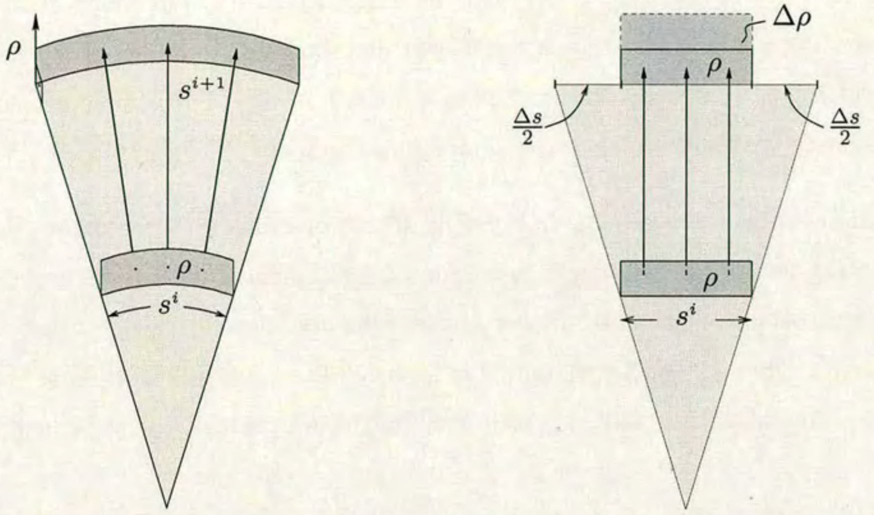

(a) continuous line segment bundle during expansion of a loop with continuous orientation

(b) line segment bundle during expansion of a loop with discretized orientation before correction

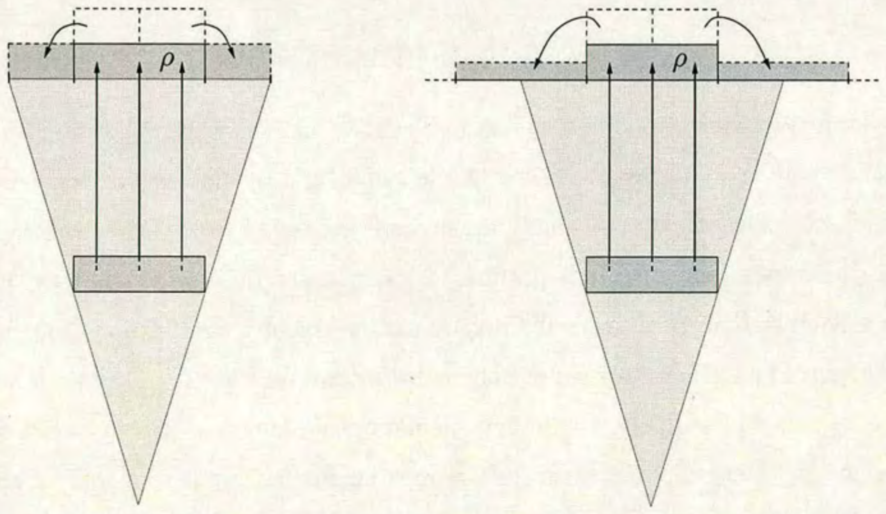

(c) density redistribution to 'stretch' the segments to the correct length and restore continuity

(d) diffusive density redistribution

Figure 5.4: *Diagrams illustrating schematically the density evolution of a bundle of expanding dislocation loops of (a) loops with continuous segment orientation and (b)-(c) loops with discretized orientation*

The numerically discretised loop, on the other hand, consists of 'straight' line segments (the orientation is constant within each segment). Hence, each point of the segment translates into the same direction and no increase in line length Δs can take place (thick black lines in Fig. 5.3(b)). However, CDD is based on the description of continuous lifted lines and therefore its equations are constructed to generate the correct additional *amount* of density (which is governed by the production term $\rho v k$ of Eq. (4.24)). Unfortunately, after discretization the transport terms fail to locate this amount in the right place.

The consequences are illustrated in Fig. 5.4: In case of a bundle of continuous lifted lines, Fig. 5.4 (a), additional line length is introduced by stretching the curved segments while the number of lines represented by the density remains constant. In case of a bundle with discrete orientations, Fig. 5.4(b), on the other hand, the segment length remains constant, leading to fragmentation, while the additional line length causes an increase in density,

$$\Delta\rho = \left(\frac{s^{i+1}}{s^i} - 1\right)\rho = \frac{\Delta s}{s^i}\rho. \tag{5.16}$$

This suggests to remedy the situation by redistributing the additional density along the line.

The intuitively obvious method to do this is shown in Fig. 5.4(c): We might remove the added density $\Delta\rho$ and distribute it to the left and right of the original segments, such as to extend these segments by exactly the amount needed to restore connectivity. Unfortunately, numerical implementation of this idea is not straightforward since we are working with a fixed spatial grid where the notation of 'segment length' is not defined. Instead, we implement a diffusive spreading scheme: We continue each segment along its direction into a sequence of segments of similar orientation and length as shown in Fig. 5.4(d), and distribute the excess density on its two nearest neighbors in this sequence. Conversely, if these neighbors already carry density (and thus produce additional density $\Delta\rho$ during loop expansion) half of the newly generated density from both neighbors is distributed back onto the original segment.

Thus, at each time step the density at $\boldsymbol{r}$ is diminished by the newly created density $\Delta\rho(\boldsymbol{r})$

but increased by the contributions $\Delta\rho_{\mathrm{L}}(\boldsymbol{r})$ and $\Delta\rho_{\mathrm{R}}(\boldsymbol{r})$ from the neighbors at $\boldsymbol{r} \pm s^i\boldsymbol{l}$,

$$\Delta\rho_{\mathrm{L}}(\boldsymbol{r}) = \frac{\Delta s}{2s^i}\rho(\boldsymbol{r} - s^i\boldsymbol{l}), \tag{5.17}$$

$$\Delta\rho_{\mathrm{R}}(\boldsymbol{r}) = \frac{\Delta s}{2s^i}\rho(\boldsymbol{r} + s^i\boldsymbol{l}). \tag{5.18}$$

The total density change due to this diffusive re-distribution is then given by

$$\Delta\rho^{\mathrm{diff}}(\boldsymbol{r}) = \frac{\Delta s}{2s^i}\left[\rho(\boldsymbol{r} - s^i\boldsymbol{l}) + \rho(\boldsymbol{r} + s^i\boldsymbol{l}) - 2\rho(\boldsymbol{r})\right]. \tag{5.19}$$

Taylor expansion around $\boldsymbol{r}$ of first two density terms on the right-hand side yields

$$\rho(\boldsymbol{r} - s^i\boldsymbol{l}) \approx \rho(\boldsymbol{r}) - s^i\nabla_{\boldsymbol{l}}\rho(\boldsymbol{r}) + \frac{(s^i)^2}{2}\nabla_{\boldsymbol{l}}^2\rho(\boldsymbol{r}), \tag{5.20}$$

$$\rho(\boldsymbol{r} + s^i\boldsymbol{l}) \approx \rho(\boldsymbol{r}) + s^i\nabla_{\boldsymbol{l}}\rho(\boldsymbol{r}) + \frac{(s^i)^2}{2}\nabla_{\boldsymbol{l}}^2\rho(\boldsymbol{r}), \tag{5.21}$$

where $\nabla_{\boldsymbol{l}}$ and $\nabla_{\boldsymbol{l}}^2$ are the first and second derivatives along the spatial direction of the line. Inserting the above two equations into Eq. (5.19) yields

$$\partial_t\rho^{\mathrm{diff}}(\boldsymbol{r}) = \lim_{\Delta t \to 0}\left(\frac{\Delta s}{\Delta t}\frac{1}{2}s^i\nabla_{\boldsymbol{l}}^2\rho(\boldsymbol{r})\right), \tag{5.22}$$

which is the general formulation of the diffusive correction term.

As fragmentation is related to orientation space discretisation in the presence of curvature, it is useful to express the correction in terms of the respective parameters. We use the identity

$$\frac{\Delta s}{s^i} = -\frac{\Delta k}{k^i} = -\Delta t\frac{\partial_t k}{k^i} \quad \text{for} \quad \Delta t \to 0 \tag{5.23}$$

and observe that the segment length s^i is related to the curvature and orientation space discretisation parameters by $s^i = \Delta\varphi/k^i$. This allows us to rewrite Eq. (5.22) as

$$\partial_t\rho^{\mathrm{diff}} = -\mu^2\left(\frac{\Delta\varphi}{k}\right)^2\frac{\partial_t k}{k}\,\nabla_{\boldsymbol{l}}^2\rho. \tag{5.24}$$

In this expression we have introduced μ as a shape factor to account for the fact that, while our argument is based on considering the lifted line as a sequence of segments of a parallel line bundle, a numerical discretization of the line in terms of Gaussian functions is more akin to a sequence of rounded 'blobs'. In practice, we determine this factor from

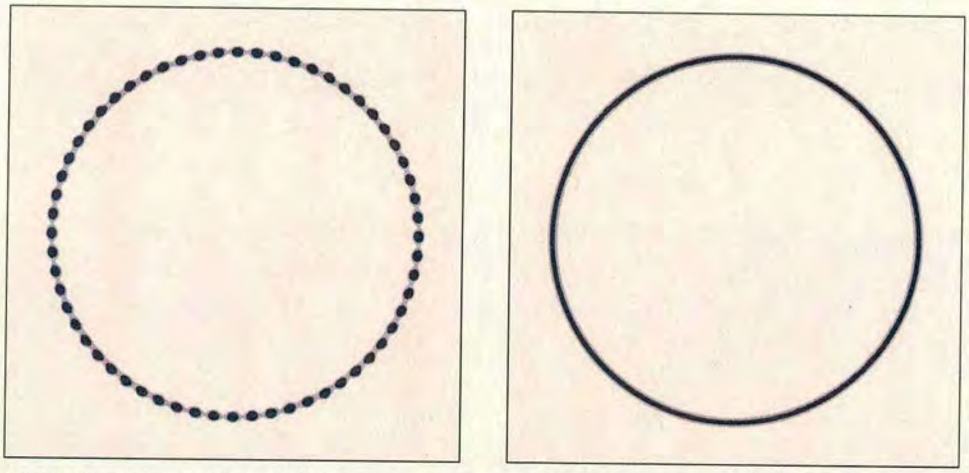

(a) Expanded loop *without* diffusive correction term after 3500 steps with $\Delta t = 0.1$ and $v = 1.0$ ($R = 380$ nodes)

(b) Expanded loop *with* diffusive correction term after 3500 steps with $\Delta t = 0.1$ and $v = 1.0$ ($R = 380$ nodes)

Figure 5.5: *Expansion of a circular loop with 60 nodes in φ-direction: projection of the density $\rho_{(r,\varphi)}$ into the spatial plane. The initial configuration was the same as in Fig. 5.1(a).*

numerical experiments to achieve an optimum balance between the dual requirements that (a) fragmentation should be efficiently suppressed and (b) the density profile of the line bundle should be preserved, i.e., no additional dispersion in the glide direction should be introduced. For the chosen discretisation of 60 nodes in angular direction an optimal value for μ can be identified as

$$\mu_{\text{opt}} \approx 0.3. \tag{5.25}$$

For larger values $\mu > \mu_{\text{opt}}$ the diffusive effect introduces a significant reduction in peak density and smearing out of the line profile, whereas for $\mu < \mu_{\text{opt}}$ the violation of $\operatorname{div} \boldsymbol{\alpha}^{\text{II}} = 0$ is still appreciable. In Fig. 5.5(b) one can observe the mending effect of the correction term.

In Fig. 5.6 the temporal evolution of the sum of the mean absolute value of $\operatorname{div} \boldsymbol{\alpha}^{\text{II}}$ is shown for different correction methods. Ideally, the sum of $\operatorname{div} \|\boldsymbol{\alpha}^{\text{II}}\|$ would be zero for all steps. Due to the numerical approximation, however, it is non-zero right from the beginning and always increases. A larger amount of diffusion decreases the sum of $\|\operatorname{div} \boldsymbol{\alpha}^{\text{II}}\|$ by comparison. The optimum amount of diffusion obtained for μ_{opt} is a trade-off between minimizing $\|\operatorname{div} \boldsymbol{\alpha}^{\text{II}}\|$ and maintaining the correct peak density value. Relaxation of ρ along the dislocation line proves the most effective method, however, carrying out the relaxation to achieve the shown accuracy requires between 10 and 30 relaxation steps after each time step, which causes an increase of the overall computation time by a factor of more than 10. Evaluating the diffusive correction, on the other hand, can be done 'on the fly' and does not cause a notable increase in computation time. For a geometry factor of $\mu = 0.3$, we observe an efficient supression of loop fragmentation.

We finally note that the same considerations as above also hold for the shrinkage of a loop. In this case the diffusion coefficient becomes negative which allows the loop to localise.

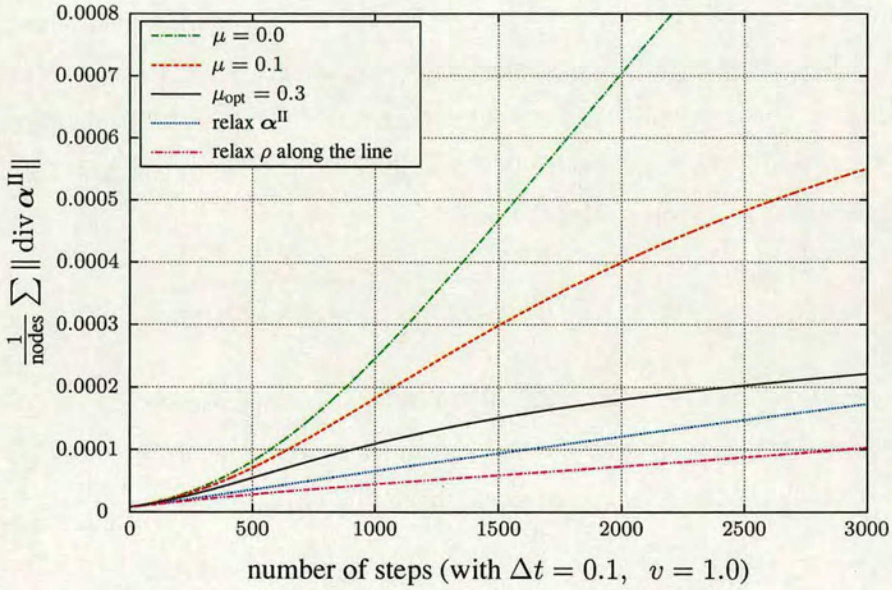

Figure 5.6: *Temporal evolution of the sum of the absolute values of* $\operatorname{div} \alpha^{II}$ *for different diffusive correction terms.*

Homogeneous distribution of expanding loops with anisotropic velocity

In the previous test cases all non-spatial terms (i.e. terms containing derivatives w.r.t. the line orientation φ) vanished in the evolution equations for the scalar density Eq. (4.24) and mean curvature Eq. (4.25). In the following, we will show that these terms play an important role when it comes to studying non-trivial density distributions and system geometries.

Anisotropic dislocation velocity When we assume an anisotropic velocity law, where v explicitly depends on φ, the velocity is no longer a constant for a fixed spatial point (x, y) as it changes with line orientation φ. As a consequence, those terms in the evolution equations which are related to the angular velocity ϑ contribute to the system evolution. One possible form for a simple anisotropic velocity law is

$$v_{(r,\varphi)} = v_0 \sqrt{(1-\chi)\sin^2\varphi + (1+\chi)\cos^2\varphi}, \tag{5.26}$$

where $\chi \in [0 \ldots 1[$ is a factor governing the velocity anisotropy in φ-direction ($\chi = 0$ gives no anisotropy) and v_0 is a constant velocity parameter. This particular mobility law is such that it expands a circular loop into elliptical shape (Fig. 5.7).

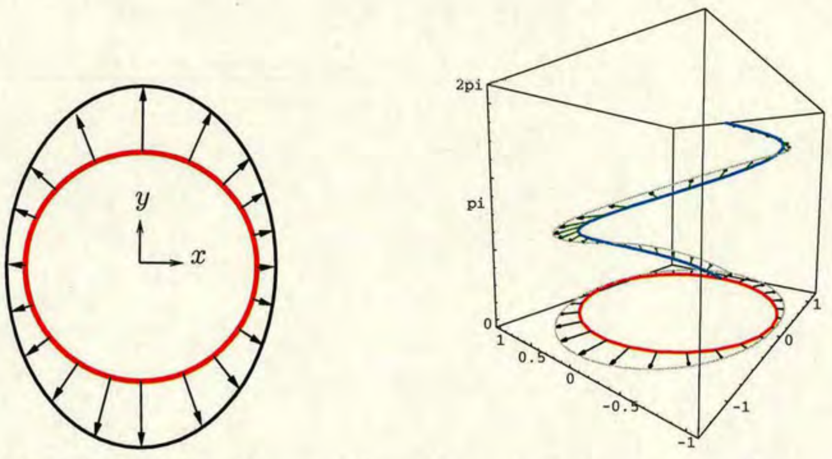

(a) circular dislocation loop with velocity in the spatial plane

(b) same loop and velocity as in Fig. 5.7(a) in the configuration space

Figure 5.7: *Dislocation loop with anisotropic velocity function. The angular velocity shows as a vertical component of the velocity along the lifted loop in Fig. 5.7(b).*

Fig. 5.7 schematically shows a sketch of this type of velocity function. The rotational velocity ϑ (as defined in Eq. (4.17)) can be written as

$$\vartheta = -\nabla_L v = -\cos\varphi \partial_x v + \sin\varphi \partial_y v + k \partial_\varphi v, \tag{5.27}$$

which simplifies for the velocity law Eq. (5.26) to

$$\vartheta = k \partial_\varphi v. \tag{5.28}$$

Curvature evolution Let us assume as initial condition a homogeneous distribution of dislocation loops with the same initial radius, and thus $k(t = 0, \boldsymbol{r}, \varphi) \equiv k_0$. The evolution of curvature due to the anisotropic velocity law occurs along the φ-direction only and reads

$$\partial_t k = -vk^2 - \nabla_L^2 v - \nabla_V k = -vk^2 - k^2 \partial_\varphi \vartheta \tag{5.29}$$

as the spatial derivatives vanish. Change of curvature occurs only due to curvature production during expansion/shrinkage of loops (the first term of Eq. (5.29)) and rotation of adjacent line segments with different rotation velocity.

Analytical solution for the curvature For the special case of an elliptical loop we can write the minimum and maximum curvature (i.e. the curvature at the intersection points of the ellipse with its minor and major axes) as

$$k_{(\varphi=0)} = \frac{b}{a^2} \quad \text{and} \quad k_{(\varphi=0.5\pi)} = \frac{a}{b^2}, \tag{5.30}$$

where a and b denote the length of minor and major axis respectively. The time evolution of a and b can be easily obtained by considering the initial radius $1/k_0$, expansion velocity v and elapsed time t:

$$a = 1/k_0 + v_{(\varphi=0)} t \quad \text{and} \quad b = 1/k_0 + v_{(\varphi=0.5\pi)} t. \tag{5.31}$$

In Fig. 5.8 the numerical solution of Eq. (5.29) is compared with the analytical solution for the evolution of curvature for two points of minimum and maximum curvature as given by Eq. (5.30) and Eq. (5.31).

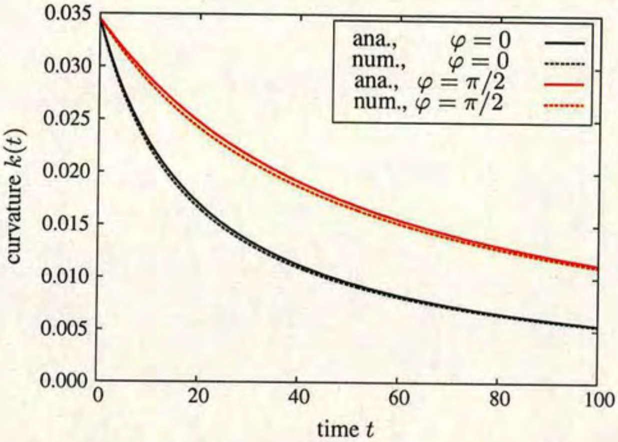

Figure 5.8: *Ananlytical and numerical curvature evolution for the line orientation* $\varphi = 0$ *(upper curves) and* $\varphi = 0.5\pi$ *(lower curves) for an anisotropy factor* $\alpha = 0.3$, $v_0 = 1$, *and an initial loop radius* $r_0 = 1/k_0 = 29$ *as parameter.*

Quasi-discrete expanding loop with anisotropic mobility law

Now we apply the same elliptical velocity law to the density distribution corresponding to a single, quasi-discrete loop. This problem differs from Section 5.2 since the second term of $\partial_t \rho$ in Eq. (4.24), which governs the transport of density in angular direction, now no longer vanishes. For the velocity law under consideration, this term is given by $\partial_\varphi(\rho\vartheta) = \partial_\varphi(\rho k \partial_\varphi v)$, and the set of evolution equations then reads

$$\partial_t \rho = -\big(\mathrm{div}(\rho \boldsymbol{v}) + \partial_\varphi(\rho k \partial_\varphi v)\big) + \rho v k \tag{5.32}$$

$$\partial_t k = -v k^2 - k^2 \partial_{\varphi\varphi} v. \tag{5.33}$$

Density transport in angular direction corresponds to the rotation of line segments. An illustration of the coupled spatial and angular transport of a discrete line segment is given in Fig. 5.9.

The prescribed velocity function is such that a circular loop should become elliptical in shape. Fig. 5.10 shows the evolution of an initially circular density distribution in the configuration space. The ability to rotate segments is a key feature of the field equations, which proves crucial for a correct description of plasticity in constrained systems (cf. Chapter 6).

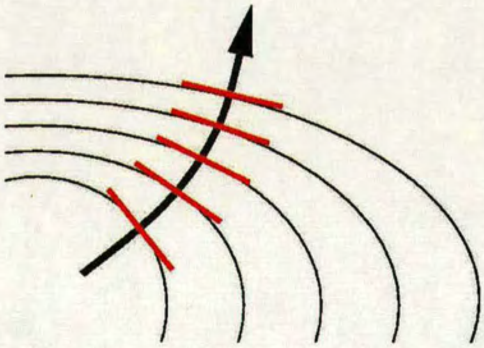

Figure 5.9: *A line segment during loop expansion gets rotated because it moves perpendicular to its line direction with an anisotropic velocity law.*

Initial density distribution:

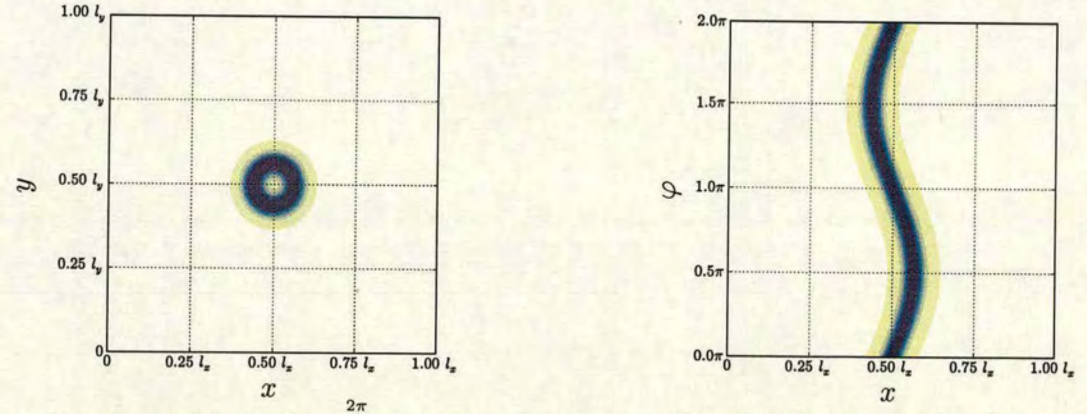

(a) scalar density $\rho_t(x,y) = \int\limits_0^{2\pi} \rho_{(r,\varphi)}\,\mathrm{d}\varphi$ at $t = 0$

(b) projected density $\rho(x,\varphi) = \int_y \rho_{(r,\varphi)}\mathrm{d}y$ at $t = 0$

Evolved density distribution:

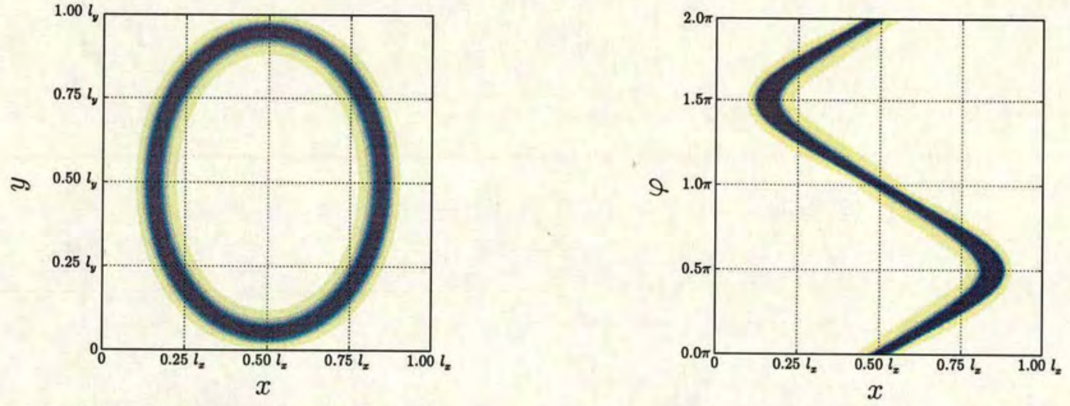

(c) scalar density $\rho_t(x,y)$ at $t = 180$

(d) projected density $\rho(x,\varphi)$ at $t = 180$

Figure 5.10: *Temporal evolution of an initially circular density distribution with anisotropic velocity (Eq. (5.26)) with $\chi = 0.3$ and velocity $v_0 = 1$. The left column shows the projection of the lifted density on the spatial plane, while the right column shows the projection on the $x - \varphi$ plane.*

Distribution of loops in a constrained channel geometry

By assuming a homogeneous distribution of initially circular dislocation loops in a constrained channel, we can study a case where all components of the evolution equations become relevant. In the following we assume a system that is homogeneous in y direction and confined by boundaries that are impenetrable for dislocations at $x = 0$ and $x = l_x$. (cf. Fig. 5.2).

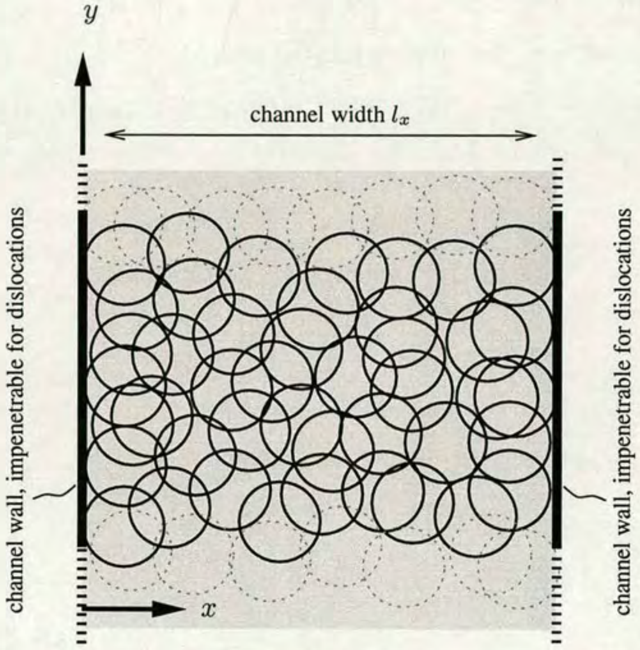

(a) channel geometry

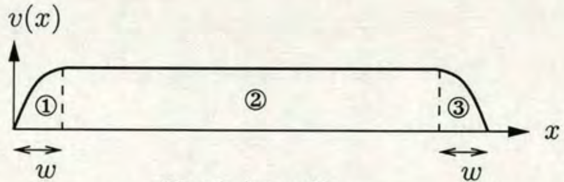

(b) velocity profile

Figure 5.11: *Slip channel geometry with sketch of initial distribution of loops with same radius. In our numerical simulation, though, those are represented by the dislocation density and mean curvature. The system is homogeneous in y-direction. The profile below shows schematic a velocity profile: ① and ③ are the 'boundary layers' with width w, ② is the 'field'.*

Initial values for our numerical simulation are obtained by summing up the density fields of quasi-discrete loops (as e.g. in Fig. 5.1(a) where the density was obtained as Gauss function representing the line) for all admissible positions such that no loops intersects the boundary walls of the channel.

$$\rho_{(r,\varphi)} = \sum_{i=1}^{\#\text{loops}} \rho^{i}_{(r,\varphi)}. \tag{5.34}$$

This has the effect that the density in the configuration space near the boundaries takes a wavy shape as shown in Fig. 5.12(a) (if the density had a constant value for all (x, φ) this would imply that some loops had to penetrate the wall).

The mean curvature values have to be obtained during this summation as well. For each quasi discrete loop we obtain the curvature as the inverse distance from the loop center. We first sum up ρk

$$(\rho k)_{(r,\varphi)} = \sum_{i=1}^{\#\text{loops}} \rho^{i}_{(r,\varphi)} k^{i}_{(r,\varphi)} \tag{5.35}$$

because k is not well defined for regions with vanishing density. If we numerically ensure that ρ is non-zero for all $(\boldsymbol{r}, \varphi)$ by e.g. adding a very small number ϵ we can obtain the mean curvature by

$$k_{(r,\varphi)} = \frac{(\rho k)_{(r,\varphi)}}{\sum_{i=1}^{\#\text{loops}} \rho^{i}_{(r,\varphi)}}. \tag{5.36}$$

With this procedure we ensure that the initial values are as close to the 'divergence-free'-state as possible, thus ensuring the solenoidality of α^{II}. The curvature for the loop distribution shown above takes a very similar form as the density and is shown in Fig. 5.12(b).

Boundary conditions are modeled by a prescribed velocity function, which smoothly decays to zero inside a thin layer - the *boundary layer* - directly at the walls (cf. Farrell *et al.* (2000) for more mathematical details). For each boundary we use the positive half of a sigmoidal function, e.g.

$$p(x) = \frac{2}{1 + e^{-x}} - 1 \tag{5.37}$$

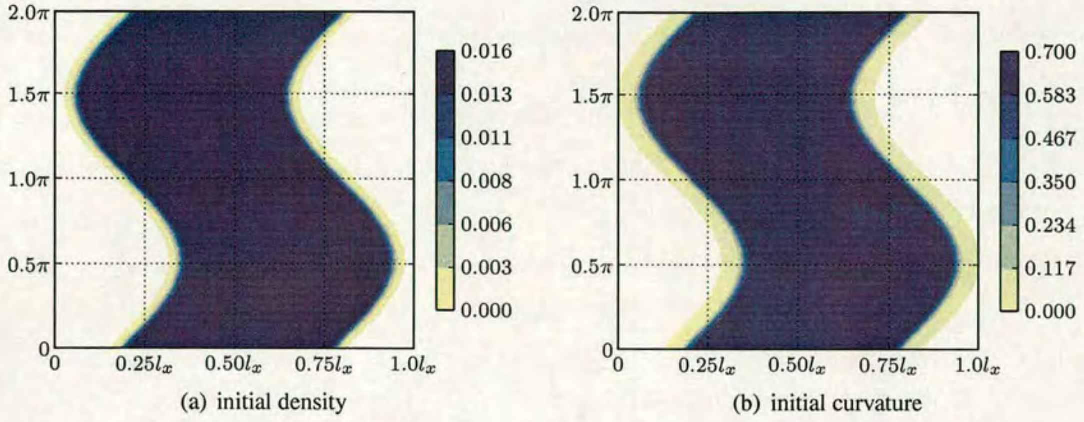

(a) initial density

(b) initial curvature

Figure 5.12: *Initial value distributions corresponding to the sketch in Fig. 5.2. The initial loops radius is* $0.3l_x$.

for the left boundary layer. $p(x)$ is 0 for $x = 0$ and approaches 1 for $x > 0$. Then the velocity has the form

$$v(x, \varphi) = v_0\, p(x)\, p(l_x - x), \tag{5.38}$$

which is independent of the line orientation[3]. To analyse these boundary conditions we study the motion of a segment with initial position x_0 and orientation φ_0:

$$x(t) = x_0 + \int_0^t v^x \mathrm{d}\tilde{t} = x_0 + t\, \cos\varphi v \tag{5.39}$$

$$\varphi(t) = \varphi_0 + \int_0^t \vartheta \mathrm{d}\tilde{t} = \varphi_0 + t\, (\cos\varphi \partial_x v + k\partial_\varphi v) \tag{5.40}$$

$$= \varphi_0 + t\, \cos\varphi\partial_x v. \tag{5.41}$$

Here, v^x denotes the velocity component in x direction, ϑ is the velocity component in φ direction.

Eq. (5.41) shows that it is the spatial velocity gradient which is responsible for the change of orientation: with the sign convention from Fig. 4.2 it can be seen that only dislocations with orientation $\varphi = \frac{1}{2}\pi$ or $\varphi = \frac{3}{2}\pi$ do not experience any further rotation since then the cos term vanishes and $\varphi(t)$ becomes static. All other line segments get rotated, either towards $\frac{1}{2}\pi$ or $\frac{3}{2}\pi$, respectively. The gradient of v as well as the deviation from the static

---

[3] v needs not necessarily to be independent of φ; in general v is defined on the same space $\mathbb{R} \times \mathbb{R} \times \mathbb{S}$ as also ρ and k.

orientation define the magnitude of change in orientation.

To visualise this mechanism we track the path of an infinitesimal line segment on its way through the boundary layer inside the configuration space, i.e. in mathematical terms we construct the integral curves of the vector field $\boldsymbol{v}(x,\varphi) = (v^x, \vartheta)$. This is, strongly magnified, shown in Fig. 5.13 for the left boundary layer.

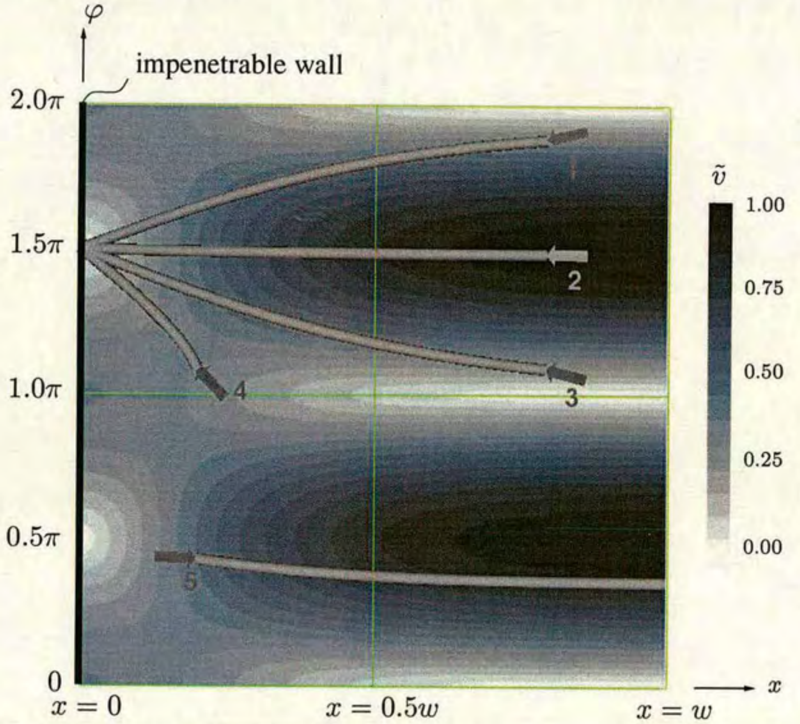

Figure 5.13: *Streamlines of an infinitesimal line segment in the boundary layer. $\tilde{v}$ is a normalised velocity and represents a resulting velocity in the configuration space. The underlying velocity function $v(x,\varphi)$ (not shown in the plot) is constant in orientation direction and decays from right ('field area') to left (boundary) towards zero.*

In the plot the background colors represent a normed velocity $\tilde{v} = \|\boldsymbol{v}\|_{\mathbb{R}\times\mathbb{S}}$, where the norm is defined by

$$\|\cdot\|_{\mathbb{R}\times\mathbb{S}} = T\sqrt{\left(\frac{v^x}{w}\right)^2 + \left(\frac{\vartheta}{2\pi}\right)^2}, \tag{5.42}$$

with w the width of the boundary layer and T a proportionality factor of unit time such that $\max\|\boldsymbol{v}_{(x,\varphi)}\| = 1$. The motivation for this norm is to obtain a measure for a velocity in the configuration space by scaling all velocity components to the same orders of magnitude.

We observe that all line segments with orientation $\pi < \varphi < 2\pi$ are moving towards the left impenetrable boundary. On their way they get rotated such that when touching the wall they are indeed oriented parallel to the wall ($\varphi = 1.5\pi$).

Considering the lower half of Fig. 5.13 , i.e. orientations inbetween 0 and π one may ask whether the 'outflux' (line 5) can be physically interpreted? Assuming a loop distributions as for instance in Fig. 5.2 one would not expect any dislocation density in the lower half of the boundary layer. The reason is that generally speaking one assumes the boundary layer width to be 'small' such that its width does not have a strong influence on the system. 'Small' however, can only be defined w.r.t. to the channel geometry and the dislocations, i.e. their loop radius. The closest a line segment with orientation $\pi/2$ gets to the *left* wall is twice its radius. In the following we always will assume that the boundary layer width is considerably smaller than this (the lower limit is given by the number of discrete nodes required to represent this smoothly differentiable jump function)[4]. The limit case of straight dislocation segments with orientation $\varphi = 0.5\pi$ (parallel to the wall) results in horizontal streamlines. Hence, either there is no outflux because there is no density or the outflux is physically reasonable. In both cases also the lower half of Fig. 5.13 is reasonable.

Temporal evolution: The effect of the boundary conditions on the initial distributions can be observed in Fig. 5.14. The dislocation loops homogeneously expand in the velocity field, leading to an increase in overall dislocation density. Once the line segments (or oriented density respectively) reach the boundary layer they get rotated towards parallel orientation along integral curves similar to those shown in Fig. 5.13. Density of only one orientation is accumulating at the impenetrable walls.

The four smallish dark spots in the S-shaped band of the curvature, Fig. 5.14(d), are curvature maxima representing the kink that a threading dislocation (stemming from an expanded loop) would have: at boundary = line parallel to the boundary, outside boundary area = line mostly perpendicular to boundary, in between a growing kink. We elucidate this effect in Section 5.2 where we treat a single loop in a channel.

The four large dark curvature areas in regions where no density is present are a numerical artefact. One could use the evolution equations for α^{II} instead of those for ρ and k in order

---

[4] Ideally, the boundary layer width tends towards zero width, which leads to extremely steep velocity gradients inside the boundary layer. To minimize discretization error one could use discretizations of different coarseness for the boundary layer and field (Farrell *et al.*, 2000). For the benchmarks problems under consideration it is sufficient to employ a fine but uniform mesh.

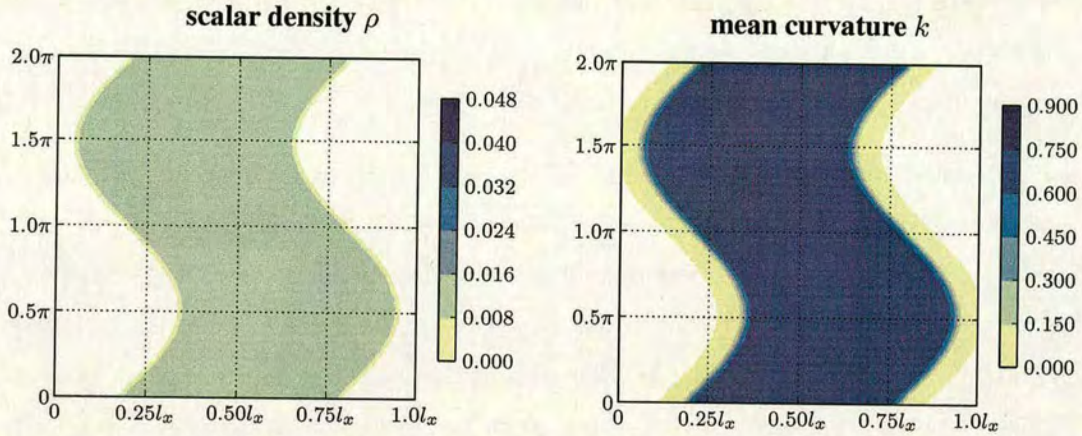

(a) initial density

(b) initial curvature

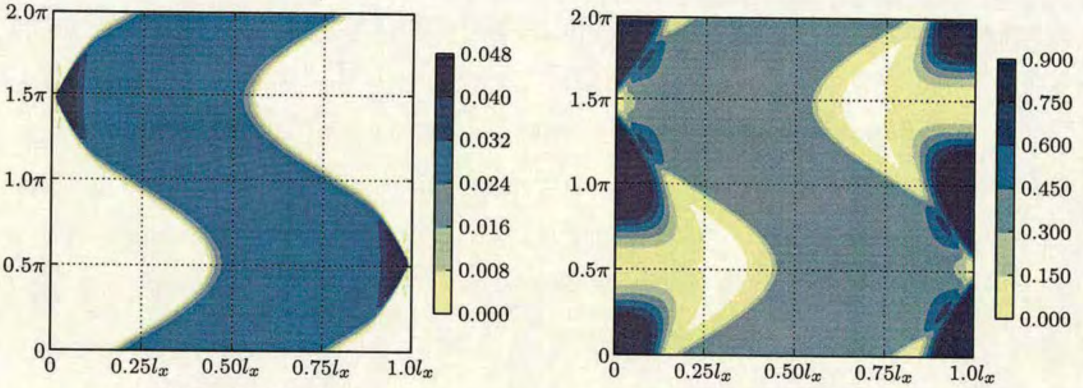

(c) evolved density

(d) evolved curvature

Figure 5.14: *Temporal evolution of density and curvature distribution in a constrained channel with impenetrable boundaries.*

to avoid having to divide by ρ. Instead of $\partial_t k$ one would then have to integrate $\partial_t(\rho k)$ and therefore could avoid the diverging behavior of the curvature in regions with vanishing density. However, k (and not ρk) is required for the transport term in φ direction in $\partial_t \rho$.

Directly at the wall the curvature is zero for orientation parallel to the wall: straight line segments get deposited.

Quasi-discrete loop in constrained channel geometry

To comprehend the evolution of the density in the constrained shear channel with continuous density distribution one can again look at the behaviour of a discrete dislocation loop by prescribing the initial density as in Fig. 5.15(a).

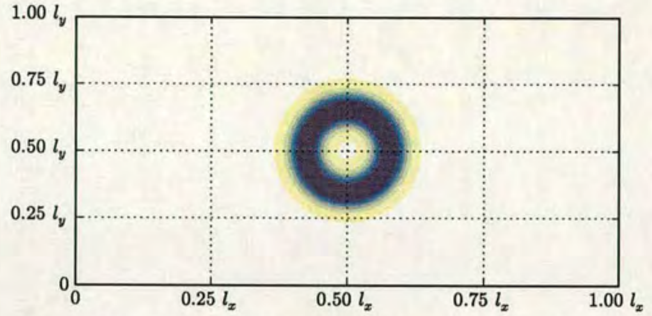

(a) initial state

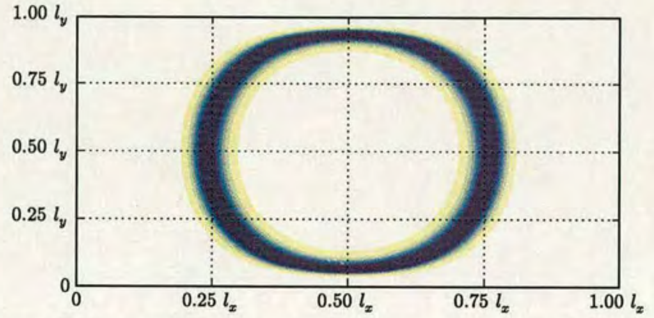

(b) loop is under influence of the boundary layer and gets partially slowed down

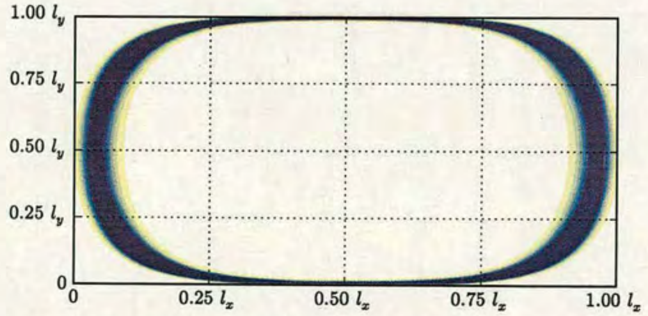

(c) density parallel to the wall gets disposed, adjacent segments get rotated towards horizontal orientation

Figure 5.15: *Evolution of a loop in constrained channel. The lower and upper walls of the channel are impenetrable; the prescribed velocity decays to zero. The system is not constrained in horizontal direction.*

The evolving system shows accumulation of density at the impenetrable boundaries at $y = 0$ and $y = l_y$. One of the key mechanisms that can be observed here is that the loop is not 'torn into parts'. The line production term $\rho v k$ is responsible for this effect.

Chapter 6

Application to Microbending

To investigate the performance of our CDD simulation scheme in a physically relevant situation, we consider the problem of micro-bending of a free-standing thin film (Sandfeld *et al.*, 2009b, 2010). This problem has several interesting features: (i) One is dealing with an intrinsically heterogeneous deformation state where the 'composition' of the dislocation arrangement changes over time due to the growing strain gradients; (ii) these strain gradients are associated with pronounced size effects that have been studied extensively using various dislocation-based models (e.g. Gao *et al.*, 1999; Zaiser & Aifantis, 2003; Sedláček, 2005b; Zaiser *et al.*, 2007; Schwarz *et al.*, 2007); (iii) the presence of an elastic core at the center of the specimen leads to the spontaneous emergence of large curvatures in the dislocation system, and hence provides an interesting test case for the numerical accuracy of our computations in a situation where all terms in the evolution equations Eq. (4.24) and Eq. (4.25) make appreciable contributions to the evolution of the dislocation system.

6.1 Model Geometry and Stress State

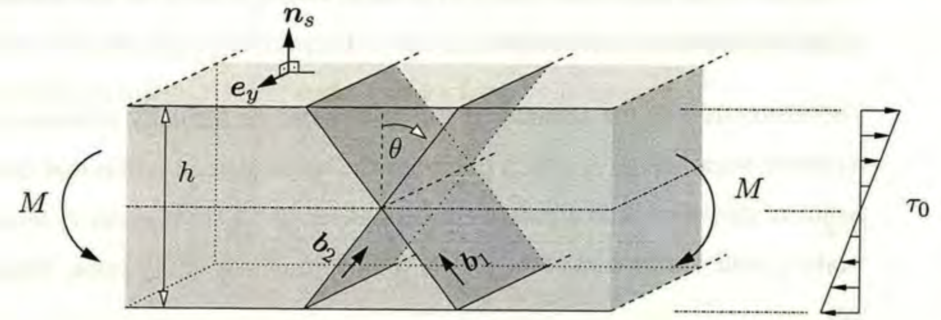

Figure 6.1: *Microbending simulations: Investigated slip geometry. τ_0 is the bending stress (resolved shear stress in the slip systems) in the absence of plastic deformation.*

We consider bending of a free standing thin film of thickness h. The normal vector of the free surfaces is denoted by n_s, and we assume without loss of generality that n_s is perpendicular to the y axis of a Cartesian coordinate system. The dimensions of the film in where $a \approx 0.4$ is a non-dimensional constant characterising the strength of dislocation-forest interactions and ρ_t is the total dislocation density as defined in Eq. (4.16).

In our constitutive model we neglect effects of large-scale dislocation curvature on the dislocation velocity (line tension as considered by Sedláček (2005a) and Zaiser *et al.* (2007)). We also neglect back stresses resulting from the 'piling up' of dislocations of the same sign (Zaiser *et al.*, 2007), which are also implemented in DDD simulations of microbending (Yefimov *et al.*, 2004; Cleveringa *et al.*, 1999). Consistent with our assumption that dislocation motion is controlled by forest interactions, we do not impose specific boundary conditions to account for image effects at the free surfaces. Instead, we allow dislocations of all orientations to enter or leave freely, simply extrapolating the dynamics inside the film across the boundary (similar to the 'natural' outflow boundary conditions in (Yefimov *et al.*, 2004), where - contrary to our boundary conditions - only outflow and no inflow of dislocations from the surface was allowed). In physical terms our boundary conditions imply that we assume that surface sources have no activation stress other than the yield stress that controls near-surface dislocation motion inside the sample.

6.3 Results

As initial condition for our simulated bending tests, we assume an isotropic dislocation distribution with zero mean curvature $k = 0$ and space-independent total dislocation density $\rho = 10^{13}\text{m}^{-2}$, i.e., initially dislocations of all orientations are present with equal density $\rho(x, \varphi) = (1/2\pi) \times 10^{13}\text{m}^{-2}$. This initial condition describes a statistically homogeneous and isotropic arrangement of straight dislocation lines threading the film at random points. We carry out bending tests for various prescribed bending moments. In physical terms, this corresponds to keeping an initially imposed curvature radius on the film. We solve the equations of motion during relaxing the system and simultaneously evaluating the increase of the plastic strain and the concomitant decrease of local stresses and increase in flow stress. Due to these changes in the internal stress state the strain rate gradually decreases towards zero. We trace this relaxation until the maximum strain rate has everywhere dropped below a prescribed low level and then record the bending moment M and strain profile $\gamma(x)$ as well as the dislocation and curvature patterns $\rho(x, \varphi)$ and $k(x, \varphi)$.

The following examples were computed using finite differences with an equidistant mesh. The resolution was about 700 spatial nodes and 100 angular nodes; a fifth-order Runge-

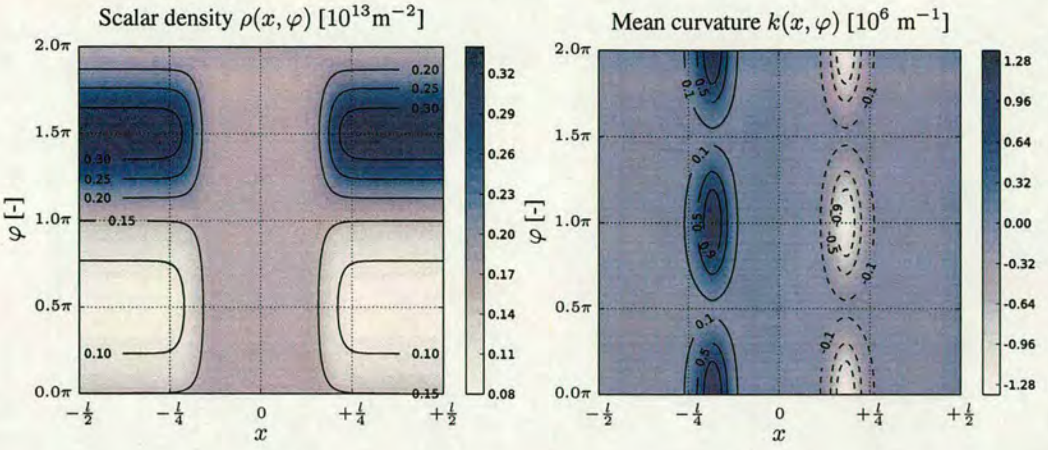

Figure 6.3: *Dislocation density and curvature patterns in* (x, φ) *configuration space for a film thickness of* $h = 3\mu$m *and bending moment (per unit length in* y*)* $M = 2 \cdot 10^{-13}$GPa m^2. *The modulus of the Burgers vector was* $b = 0.256$nm, *the shear modulus* $G = 48.3$GPa.

Kutta method with adaptive step size control turned out to be an effective time integration scheme: the computational cost on a 2.4 GHz quad core work station for each of the following simulations is about 20 minutes.

Streamlines of the velocity field As we did already in Section 5.2 (Fig. 6.4 and respective explanation) we can again investigate the behavior of an infinitesimal line segment in the configuration space. The main difference here is, that the velocity is changing in time, i.e. it approaches zero in the converged state. In Fig. 6.4[1] line segments 1-3 are moving towards the elastic zone (1 and 2 are surface sources), segment 7 is a dislocation with negative edge orientation and exits the film after $t = 0.6T_{\text{conv}}$ while segment 4 and 6 are subject to very strong rotations towards positive edge orientation. One can observe that in general dislocations with (near) edge orientation (e.g. $\varphi = 0.5\pi$ and $\varphi = 1.5\pi$) do not get rotated and simply translate in spatial direction. The bigger the screw-part of a dislocation the stronger the rotational effect on the dislocation.

Furthermore, the streamlines explain why the density plots in Fig. 6.5 exhibit a somewhat roundish shape towards the elastic core: the reason is that some dislocations 'get stuck' somewhere inside the film before they could reach the elastic core.

---

[1] for more details on the construction of the integral curves please refer to Fig. 5.13

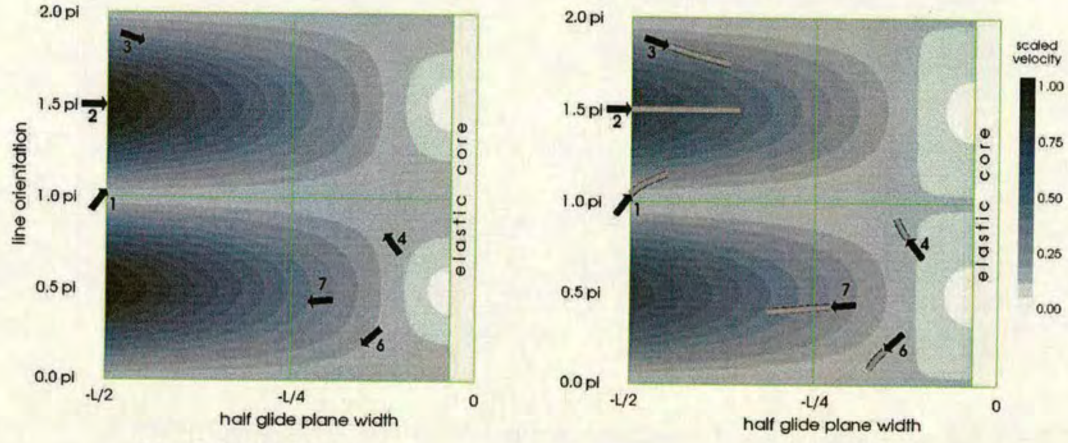

(a) $t = 0$ (initial state)

(b) $t = 0.2T_{\text{conv}}$

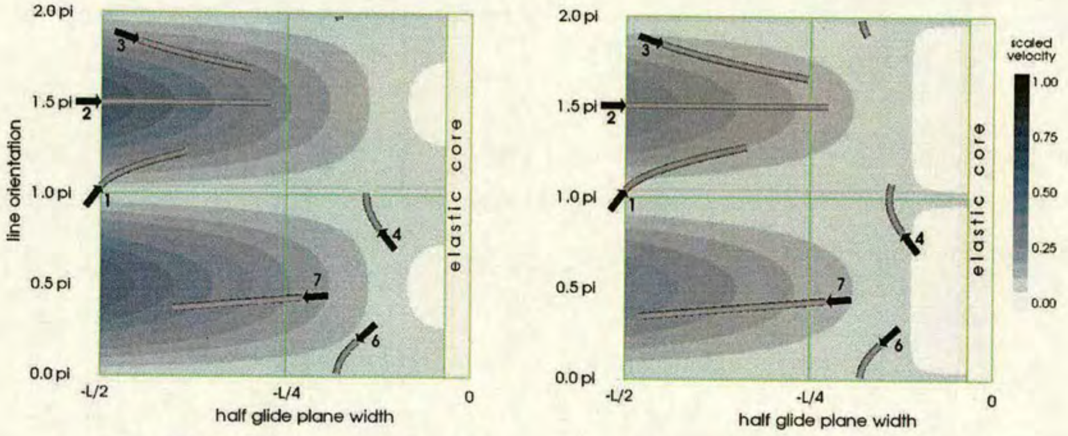

(c) $t = 0.4T_{\text{conv}}$

(d) $t = 0.6T_{\text{conv}}$

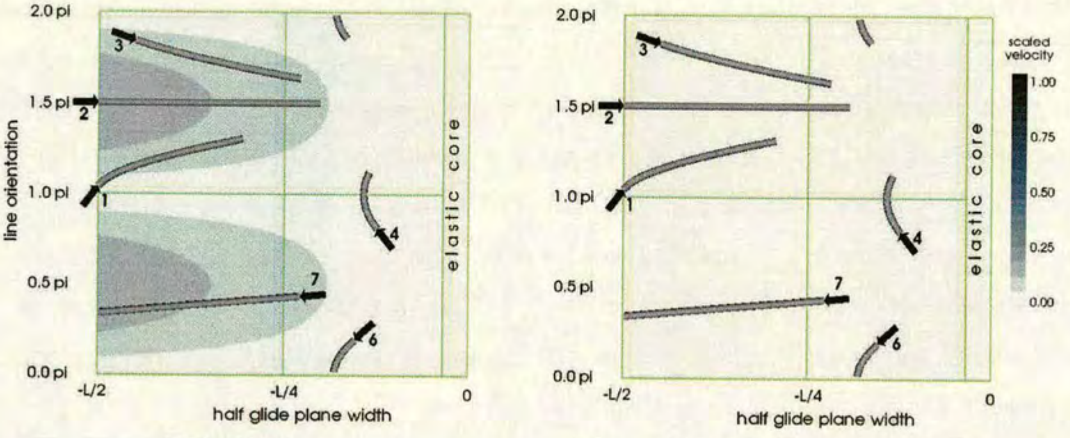

(e) $t = 0.8T_{\text{conv}}$

(f) $t = T_{\text{conv}}$ (converged state)

Figure 6.4: *Path of a infinitesimal density 'particles' inside one half of the film. The velocity field changes in time and reaches the converged state at* $t = T_{conv}$ *(Fig. 6.4(f)). This configuration corresponds to a system with film height* $h = 2\mu\text{m}$ *and* $M = 50000\text{GPa m}$.

Typical density and curvature patterns are shown in Fig. 6.3. These patterns are characterised by the presence of an elastic core region where the stress $\tau_0(x)$ is less than the yield stress corresponding to the initial dislocation density. No deformation activity takes place within this region and, hence, the dislocation density and curvature remain at their initial values. Curvature spatially localizes near the boundaries of the elastic core region which are moving inwards with increasing stress. Ideally the curvature maxima in x-direction would be restricted to a point only, which would be located at the border of the elastic core and mathematically has singular character. This singularity can not be treated by the numerical scheme which smoothes out the high gradients. As a consequence the curvature gets slightly smeared out in spatial direction. In physical terms this can be understood as assuming a smooth transition in velocity from the elastic core ($v = 0$) and the plastic regions instead of a sharp kink. In physical terms the very localised, sharp kink is not reasonable since it is not possible to bend a dislocation line with an arbitrarily high curvature. The smeared-out shape in φ-direction is correct and can be properly represented by our numerical scheme. In terms of the orientation coordinate, curvature is strongest for near-screw orientations while edge dislocations are only weakly bent. Density accumulates in the $\varphi = 3\pi/2$ direction, which is the orientation of edge dislocations required to accommodate the bending strain gradient. At the same time, the density of dislocations of other orientations decreases. The decrease is most pronounced for the $\varphi = \pi/2$ orientation, i.e. for edge dislocations of the opposite sign.

As the strain increases, we observe that the total dislocation density in the plastic regions increases strongly, as shown in Fig. 6.5. This increase goes along with an increase of the α_{11} component of the Kröner-Nye tensor, i.e. accumulation of 'geometrically necessary' dislocations required to accommodate the increasing plastic strain gradients around the narrowing central elastic core. This is illustrated in Fig. 6.6.

We note in passing that the values for γ are compatible with those of the Kröner-Nye tensor Eq. (4.13) in the sense that $\nabla_x \gamma$ exactly yields the shown α_{11}, which might not be obvious from Fig. 6.6 where γ appears to be piecewise straight. Nonetheless, there is a small transition from the range with linearly increasing γ to the the elastic core within which γ smoothly decays to zero.

The increase of total dislocation density that comes with the accumulation of geometrically necessary dislocations leads, according to the Taylor relation, to an increase in flow stress. As strain gradients are bigger in smaller specimens and therefore the accumulation

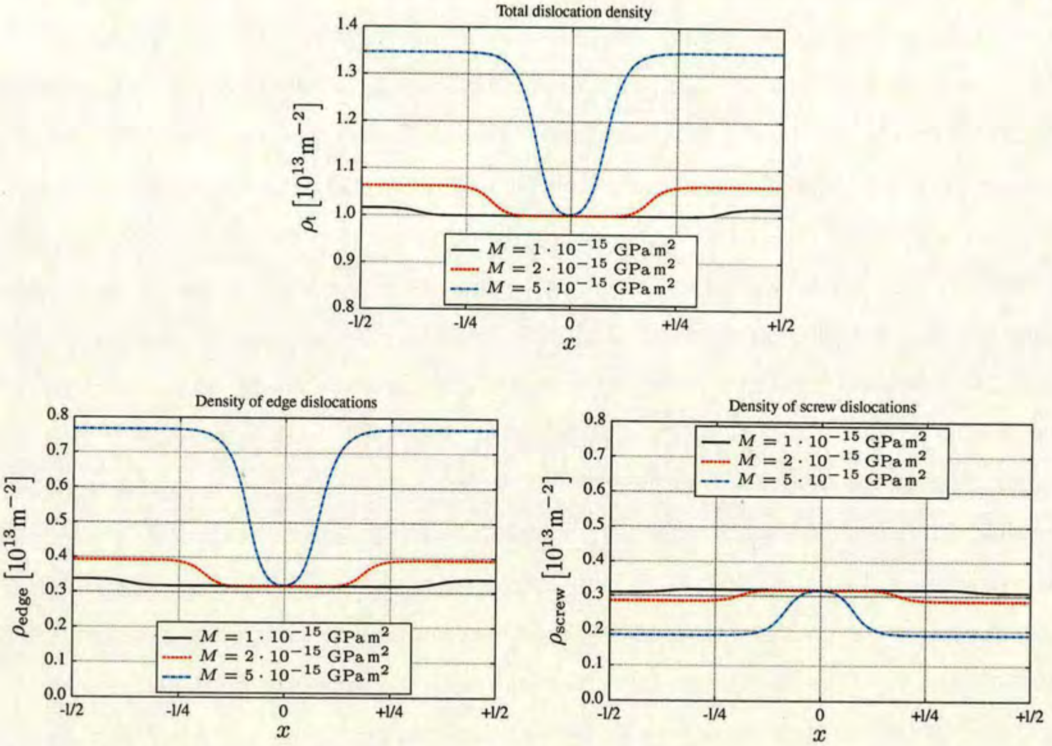

Figure 6.5: *The top diagram shows the total dislocation density* $\rho_t(x)$. *The left and right diagrams show the densities of edge and screw dislocation for* $h = 3\mu$m*:* $\rho_{\mathrm{edge}} = \rho(\varphi = 0.5\pi) + \rho(\varphi = 1.5\pi)$ *and* $\rho_{\mathrm{screw}} = \rho(\varphi = 0) + \rho(\varphi = \pi)$.

of geometrically necessary dislocations is more pronounced, this leads to a size dependent hardening. This is illustrated in Fig. 6.7 which shows the scaled bending moment M/h^2 as a function of the average plastic strain $\langle\gamma\rangle = (1/h)\int_{-h/2}^{+h/2} |\gamma(x)|\,\mathrm{d}x$. While the initial flow stress is size independent, the hardening rate and the flow stress at finite strain increase with decreasing film thickness.

6.4 Discussion

An often-repeated argument for analyzing this type of size-dependent behavior (see e.g. Gao *et al.* (1999)) runs as follows: The dislocation density in a material is the sum of a geometrically necessary density ρ_G (up to a geometrical factor η equal to the strain gradient divided by the Burgers vector modulus) and a so-called 'statistically stored' density ρ_S. (The latter is in fact nothing but the total dislocation density minus the geometrically necessary one, but the argument treats it like an independent physical variable.) From Taylor's relation

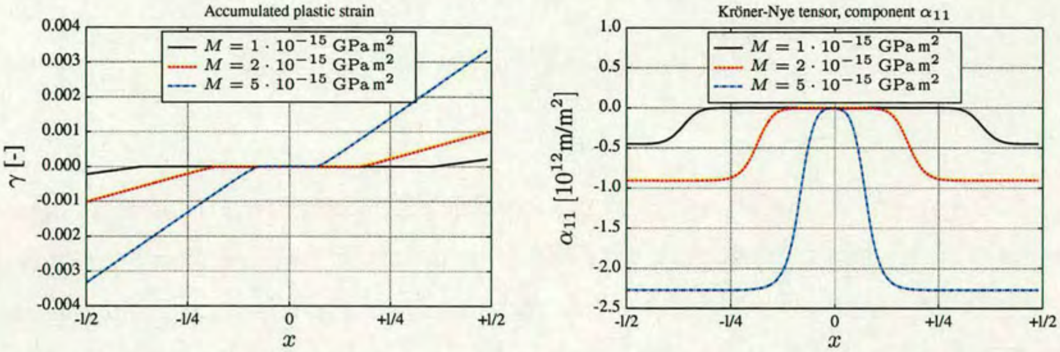

Figure 6.6: *Accumulated plastic strain and* α_{11} *component of the Kröner-Nye tensor for* $h = 3\mu$m *and different bending moments*

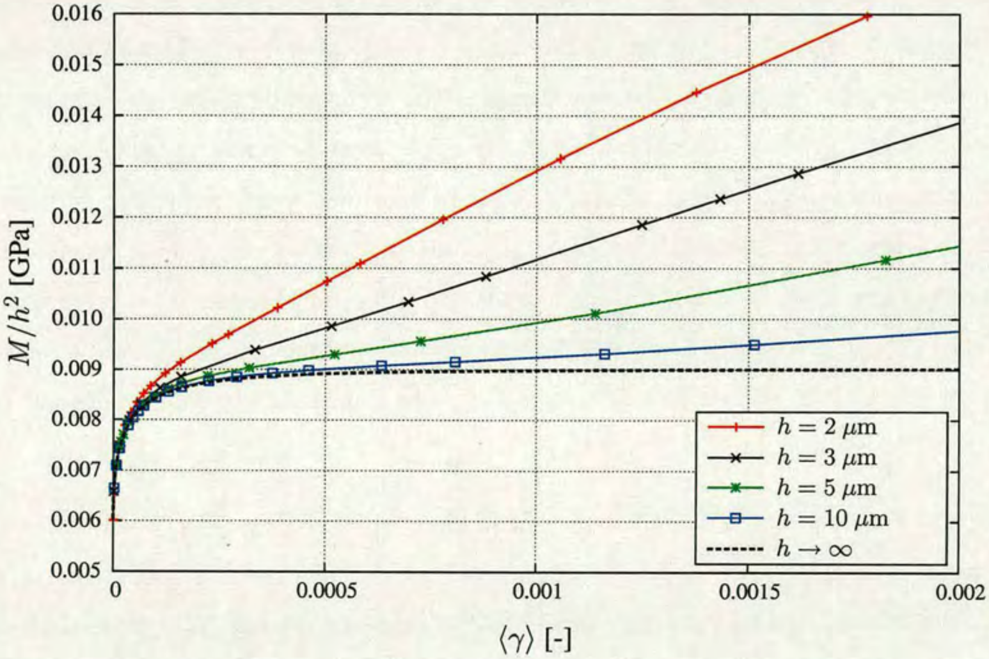

Figure 6.7: *Bending curves for various film thicknesses; the curve for infinite thickness has been calculated by assuming ideal plasticity and using the standard assumption of straight specimen cross-sections.*

for the flow stress one obtains

$$\tau_{\mathrm{y}} = aGb\sqrt{\rho_{\mathrm{t}}} = aGb\sqrt{\rho_{\mathrm{S}} + \rho_{\mathrm{G}}} = aGb\sqrt{\rho_{\mathrm{S}} + \frac{\eta}{b}|\nabla\gamma|}\,. \tag{6.6}$$

One then makes the crucial assumption that the strain dependence of the 'statistically stored' density $\rho_{\mathrm{S}}(\gamma)$ does not depend on the presence or absence of strain gradients. Estimating the characteristic strain gradient as $\langle\gamma\rangle/L$ where $\langle\gamma\rangle$ is a characteristic strain and L a characteristic dimension of the specimen then leads to a scaling relation for the characteristic flow stress τ:

$$[\tau_{\gamma,L}]^2 = [\tau_{\gamma,\infty}]^2 + a^2G^2\eta b\frac{\langle\gamma\rangle}{L}\,, \tag{6.7}$$

where $\tau_{\langle\gamma\rangle,\infty} = aGb\sqrt{\rho_{\mathrm{S}}(\gamma)}$. To test this scaling relation we have to translate the notations to our problem. The characteristic dimension L corresponds to the film thickness h, and the macroscopic flow stress corresponds to the scaled bending moment M/h^2. As strain measure we use the average plastic strain $\langle\gamma\rangle$ as defined above. The infinite-system limit is obtained by solving the bending problem for an ideally plastic material with flow stress corresponding to the initial dislocation density. The corresponding deformation curve is denoted as $[M_{\langle\gamma\rangle}/h^2]_\infty := \lim_{h\to\infty}[M_{\langle\gamma\rangle,h}/h^2]$. The total dislocation density $\langle\rho_{\mathrm{t}}\rangle$ in the specimen is obtained by averaging $\rho(x,\varphi)$ over the specimen cross section and integrating over all orientations φ, and the 'geometrically necessary' density $\langle\rho_{\mathrm{G}}\rangle$ is obtained as the minimum density of dislocations on each of the two slip systems required to accommodate the plastic strain gradient: We evaluate the component α_{11} of the dislocation density tensor, average this over the specimen cross section, divide by b and multiply with the geometrical factor $1/(2\sin\theta)$.

If the above argument would apply to our simulations, a plot of $[M_{\langle\gamma\rangle,h}/h^2]^2 - [M_{\langle\gamma\rangle}/h^2]^2_\infty$ versus the scaled plastic strain $\langle\gamma\rangle b/h$ should yield a straight line passing through the origin. The same should be true for a plot of the total dislocation density $\langle\rho_{\mathrm{t}}\rangle$ (reduced by the infinite-system value) versus the scaled plastic strain. Our simulations, however, indicate a different behavior. Even though the 'geometrically necessary' dislocation density increases approximately linearly with scaled plastic strain, the same is not true for the total dislocation density: the increase in total density initially lags behind the increase in the 'geometrically necessary' density and only catches up at large strains (Fig. 6.8). As a consequence, the scaling plot of the reduced bending moment vs. the scaled plastic strain (Fig. 6.9) fails to produce a straight line.

What are the reasons for the discrepancy between the simulation results and the naive scaling argument? Our investigation of dislocation density evolution indicates that the linear increase of the 'geometrically necessary' density with reduced strain is not matched by a concomitant increase of the total density, and hence of the flow stress. The reason is that we allow dislocations to change their orientation, besides freely entering or leaving through the specimen surface.

As a consequence, part of the increase of the 'geometrically necessary' density is not produced by additional dislocations entering through the surfaces, but rather by changes in orientation of existing dislocations and by the loss of dislocations of the 'wrong' sign.

Therefore the size effect manifests itself only after an 'incubation strain' during which the geometrically necessary density increase is mainly accommodated by the rotation of existing dislocations. Only after this is exhausted, additional dislocations have to enter from the surfaces and we observe a transition towards a linear increase of dislocation density with strain/strain gradient and a concomitant size dependent hardening as predicted by standard models. As a consequence, the total dislocation density increases, at least for small strains/large system sizes, much less than expected according to the simple scaling argument. This indicates that the assumption of a separate 'statistically stored' density that evolves in a size-independent manner is not warranted.

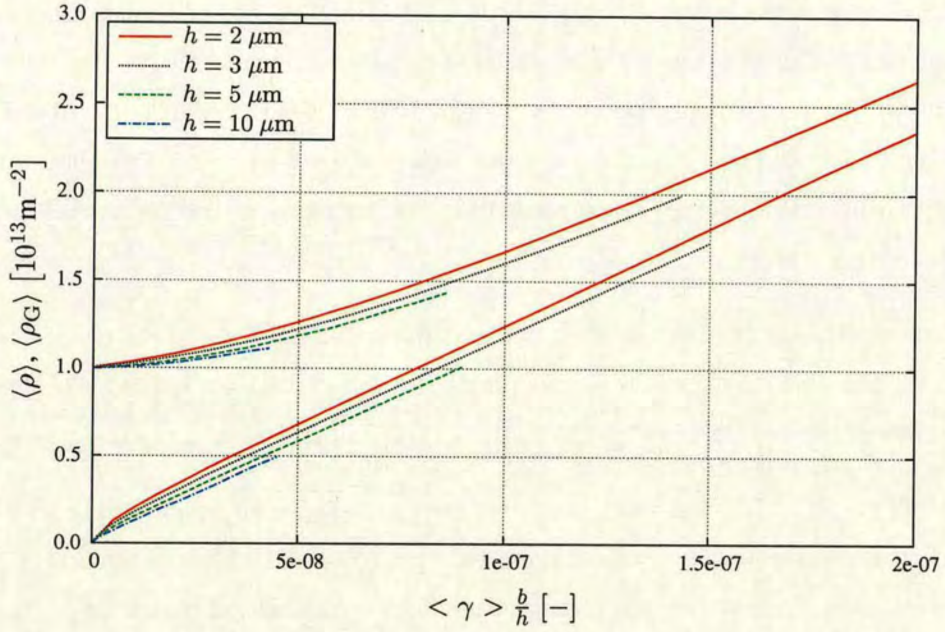

Figure 6.8: *Scaling plot of the total and 'geometrically necessary' dislocation density vs reduced strain $\langle\gamma\rangle b/h$. The upper line group is the plot for $\langle\rho\rangle$, the lower line group is the plot for $\langle\rho_G\rangle$.*

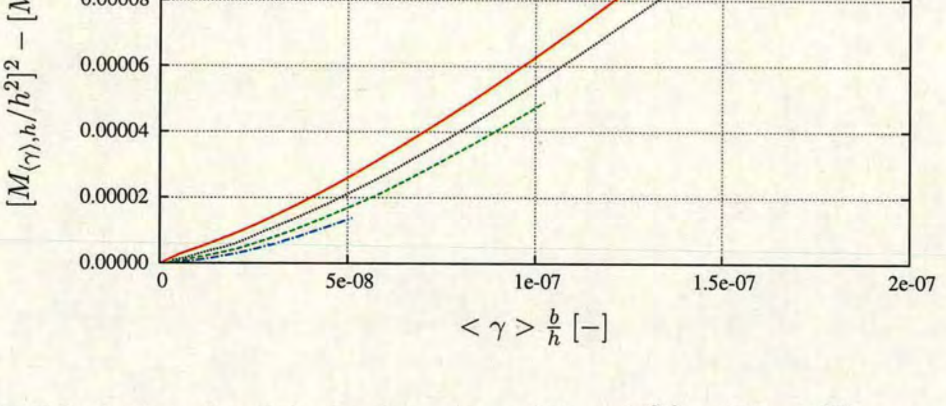

Figure 6.9: *Scaling plot of the bending curves: $[M_{\langle\gamma\rangle,h}/h^2]^2 - [M_{\langle\gamma\rangle}/h^2]^2_\infty$ vs reduced strain $\langle\gamma\rangle b/h$.*

Part III

Simplified Form of CDD

Chapter 7

Derivation of simplified equations

7.1 Motivation and introduction

Whilst exploring CDD in the previous chapters (Chapter 5 and Chapter 6) one could see that both simple benchmark problems and physically relevant problems can be tackled with this theory. However, when extrapolating the necessary computational effort and required memory storage to larger systems (e.g. a truly 3-dimensional polycrystal with multiple slip systems) it becomes evident that technical issues might become a limiting factor for the straightforward application of CDD: e.g., a two-dimensional glide plane in a three-dimensional single crystal as used in Chapter 6, *Application to Microbending*, would be discretised by about 1000 nodes in both spatial directions and about 100 nodes in angular direction. Each point of the glide plane needs to keep track of at least ρ, k, $\partial_t\rho$, $\partial_t k$ and v (neglecting the fields for plastic strain γ and stresses which have no angular components and thus require only a fraction of the memory needed by the other fields). This amounts to $5 \cdot 10^8 \cdot 8\text{bytes} \approx 4\text{GB}$ of computer memory for *one* glide plane, which can only just be handled on a workstation computer; increasing the number of glide planes and considering that the computational cost increases linearly with the number of glide planes indicates that the storage requirements become a true problem and thus gives rise to the question whether CDD could be simplified to reduce the number of degrees of freedom.

Hochrainer showed that this is indeed possible if one makes some simplifying assumptions (Hochrainer *et al.*, 2009, 2010) [1]. In the following we start by giving a slightly more detailed overview than presented in the afore mentioned publications over the necessary steps for the simplification along with comments on the required assumptions. Special emphasis is put on the rotational velocity and the consequences from the simplifications. Afterwards, we explore the evolution equations of the 'simplified Continuum Dislocation Dynamics' (abbreviated by sCDD) numerically and compare them to those of CDD.

---

[1] Although in Hochrainer *et al.* (2009) these derivations were first attempted and published, the evolution equation of mean curvature in this paper was later revised in Hochrainer *et al.* (2010)

7.2 Evolution Equations for the scalar field variables

Starting point of the derivation is CDD in the form as introduced in Part II. There, the evolution equations for density and curvature, Eq. (4.24) and Eq. (4.25), were obtained under the assumption that in the same spatial point dislocations of different orientation can have different velocity and curvature, while - in the same point - dislocations of the same orientation must have the same velocity and mean curvature. With the aim of reducing the number of degrees of freedom, this restriction was even enforced in Hochrainer *et al.* (2010) by assuming that all dislocations in a spatial point do have the same scalar velocity v, even though the velocity vectors $\boldsymbol{v} = v\boldsymbol{\nu}$ of course differ. Then the orientation coordinate φ is no longer needed. In sCDD the total dislocation density ρ_{t} and the geometrically necessary edge and screw components play an important role. The former can be derived from the higher order scalar density by integration (Eq. (4.16)). With the sign convention from Fig. 4.2 for the angle φ, the usual assumption of a constant Burgers vector $\boldsymbol{b} = b\boldsymbol{e}_1$ and Eq. (4.13) we define two scalar densities κ_x and κ_y as

$$\kappa_x := \frac{\alpha_{11}}{b} = \int_0^{2\pi} \rho(\varphi)\cos(\varphi)\,\mathrm{d}\varphi \qquad \text{and} \qquad \kappa_y := \frac{\alpha_{12}}{b} = \int_0^{2\pi} \rho(\varphi)\sin(\varphi)\,\mathrm{d}\varphi \tag{7.1}$$

which represent the averaged GND density of edge and screw dislocations, respectively. The Euclidean norm of $\kappa_x \boldsymbol{e}^1 + \kappa_y \boldsymbol{e}^2$ is exactly ρ_{G} from Eq. (3.15) with

$$\rho_{\mathrm{G}} = \sqrt{\kappa_x^2 + \kappa_y^2}. \tag{7.2}$$

As a preparation for the next steps we use these quantities to define the *average tangent vector of GND density* $\boldsymbol{l}$ (compare Eq. (3.14)):

$$\boldsymbol{l} = \boldsymbol{e}_x \cos\varphi_{\mathrm{G}} + \boldsymbol{e}_y \sin\varphi_{\mathrm{G}} \tag{7.3}$$

$$\text{where} \quad \tan\varphi_{\mathrm{G}} = \frac{\kappa_y}{\kappa_x}, \ \cos\varphi_{\mathrm{G}} = \frac{\kappa_y}{\rho_{\mathrm{G}}} \quad \text{and} \quad \sin\varphi_{\mathrm{G}} = \frac{\kappa_x}{\rho_{\mathrm{G}}}$$

Again, $\boldsymbol{\nu}$ is the vector perpendicular to the line direction $\boldsymbol{l}$.

Evolution of scalar density The evolution of the total dislocation density can be obtained by taking the time derivative of Eq. (4.16), interchanging differentiation and integration and inserting the evolution equation for the density Eq. (4.24)

$$\partial_t \rho_\mathrm{t} = \int\limits_0^{2\pi} \partial_t \rho \,\mathrm{d}\varphi = \int\limits_0^{2\pi} \left(-\left(\operatorname{div}\left(\rho \boldsymbol{v}\right) + \partial_\varphi\left(\rho \vartheta\right)\right) + \rho v k\right) \,\mathrm{d}\varphi. \tag{7.4}$$

The above assumption of a line orientation-independent scalar velocity reduces the second term of the integral - which governs the angular transport of density - to

$$\partial_\varphi\left(-\cos\varphi\rho\partial_x v + \sin\varphi\rho\partial_y v\right). \tag{7.5}$$

Here we used ϑ in the formulation given in Appendix A, Eq. (A.7). Integration over all orientations and substitution by Eq. (7.1) yields

$$\int\limits_0^{2\pi} \partial_\varphi\left(\rho\vartheta\right) \,\mathrm{d}\varphi = \int\limits_0^{2\pi} \partial_\varphi\left(-\cos\varphi\rho\partial_x v + \sin\varphi\rho\partial_y v\right) \,\mathrm{d}\varphi = 0. \tag{7.6}$$

We would like to point out that the vanishing integral does not imply that also the integrand vanishes. As a consequence, density still can change its orientation ('rotate') while the total amount of density in each point is conserved w.r.t. this term. This is for instance crucial for the conversion of SSD density into GND density and visa versa as was shown to be of importance in Chapter 6. Contrary to CDD the rotation/rotational velocity is no longer an explicitly visible component of the sCDD's evolution equations.

Now we can write the evolution equation for the total density Eq. (7.4) as

$$\begin{aligned} \partial_t \rho_\mathrm{t} &= -\operatorname{div}\left(v \int\limits_0^{2\pi} \rho(\boldsymbol{e}_x \sin\varphi - \boldsymbol{e}_y \cos\varphi)\,\mathrm{d}\varphi\right) + v\int\limits_0^{2\pi} \rho k \,\mathrm{d}\varphi \qquad (7.7)\\ &= -\left(\partial_x(v\kappa_y) - \partial_y(v\kappa_x)\right) + v\int\limits_0^{2\pi} \rho k \,\mathrm{d}\varphi \qquad (7.8) \end{aligned}$$

Integration of the (11)- and (12)-components of Eq. (4.23) yields the evolution equations for the GND density components

$$\partial_t \kappa_x = -\partial_y(\rho v) \quad \text{and} \quad \partial_t \kappa_y = +\partial_x(\rho v) \tag{7.9}$$

For brevity we will use the following definition

$$\nabla_{\kappa_\nu}(v) := \partial_x(v\kappa_y) - \partial_y(v\kappa_x). \tag{7.10}$$

Evolution of mean curvature As a convenient abbreviation we define

$$\overline{\rho k} := \int_0^{2\pi} \rho k \, \mathrm{d}\varphi \tag{7.11}$$

$$\overline{k} := \frac{\overline{\rho k}}{\rho_\mathrm{t}} = \frac{\int_0^{2\pi} \rho k \, \mathrm{d}\varphi}{\int_0^{2\pi} \rho \, \mathrm{d}\varphi}, \tag{7.12}$$

where both quantities do not have any φ dependency now. Note that $\overline{\rho k}$ is the averaged third component of the dislocation density tensor of second order Eq. (4.14). Using ρk instead of only k as a field is useful even in CDD: there the ρk term can be easily defined even for regions with (almost) zero density, while it is not clear how this should be done with k alone (what is a reasonable dislocation curvature if there is no dislocation?).

We would like to point out that the averaging in definition Eq. (7.12) is an additional averaging in the sense that already in CDD k is the mean curvature, i.e. the average curvature of line segments with the *same orientation*. $\overline{k}$ now is a further averaged value; it is the curvature of *all* line segments in one point regardless their orientation.

For obtaining the evolution of the curvature one has to make the additional assumption that the curvature (as well as the velocity) does not depend on the line orientation. In quasi-static situations where the curvature is determined by the requirement that the line tension compensates the local stress tantamount to assuming a line tension that does not depend on the line orientations.

$\partial_t\overline{k}$ can be obtained from Eq. (7.12) by taking the time derivative of the right equation and exchanging integration and differentiation in the denominator. In what follows we will derive an expression for the terms of $\partial_t(\rho k) = \rho\partial_t k + k\partial_t\rho$. Insertion of the evolution equations for scalar density and mean curvature, Eq. (4.24) and Eq. (4.25), gives us

$$\partial_t(\rho k) = -\rho\nabla_{\boldsymbol{L}}^2 v - \rho\nabla_{\boldsymbol{V}} k - k\,\mathrm{Div}(\rho\boldsymbol{V}) \tag{7.13}$$

where in the last term the definition of the generalised divergence according to Eq. (4.26) was used. The second and third term can be combined to $\mathrm{Div}(\rho k \boldsymbol{v}) = \rho \nabla_{\boldsymbol{V}} k + k\,\mathrm{Div}(\rho \boldsymbol{v})$ which gives us an expression for $\partial_t(\rho k)$

$$\partial_t(\rho k) = -\rho \nabla_{\boldsymbol{L}}^2 v - \mathrm{Div}(\rho k \boldsymbol{V}) \tag{7.14}$$

All quantities in Eq. (7.14) are quantities defined on the higher order configuration space. To obtain an expression for the averaged curvature within the framework of sCDD we integrate Eq. (7.14) and split the Div-term in spatial and angular derivatives

$$\partial_t(\overline{\rho k}) = -\underbrace{\int_0^{2\pi} \rho \nabla_{\boldsymbol{L}}^2 v \,\mathrm{d}\varphi}_{②} - \underbrace{\int_0^{2\pi} \nabla \cdot (\rho k \boldsymbol{v})\ \mathrm{d}\varphi}_{①} - \underbrace{\int_0^{2\pi} \partial_\varphi \left(\rho k \vartheta\right)\ \mathrm{d}\varphi}_{=0}, \tag{7.15}$$

where the third integral vanishes upon integration in analogy to Eq. (7.6). The other two integrals can be simplified as follows:

①: can be obtained by considering that $k_{(r,\varphi)}$ is assumed to have no angular dependency, i.e. $k_{(r,\varphi)} = \overline{k}$. Exchanging integration and differentiation and pulling out the variables that do not depend of φ yields

$$\int_0^{2\pi} \nabla \cdot (\rho k \boldsymbol{v})\ \mathrm{d}\varphi = \nabla \cdot \left(\overline{k} v \int_0^{2\pi} \rho \boldsymbol{\nu} \,\mathrm{d}\varphi \right) \tag{7.16}$$

where $\boldsymbol{\nu}$ is the unit vector perpendicular to the tangent of the GND density. Explicitly rewriting this with the definition of $\boldsymbol{\nu}$ results in th identity

$$\Rightarrow \int_0^{2\pi} \nabla \cdot (\rho k \boldsymbol{v})\ \mathrm{d}\varphi = \nabla \cdot \left(\overline{k} v \int_0^{2\pi} \rho_{(r,\varphi)}(-\sin\varphi, \cos\varphi) \,\mathrm{d}\varphi \right) \tag{7.17}$$

With the abbreviation Eq. (7.10) we obtain

$$\int_0^{2\pi} \nabla \cdot (\rho k \boldsymbol{v})\ \mathrm{d}\varphi = \nabla_{\boldsymbol{\kappa}_\nu}(kv) \tag{7.18}$$

②: We split the twofold gradient into a spatial and an angular component and use that

v has not angular dependency (i.e. $\partial_\varphi v = 0$)

$$\int_0^{2\pi} \rho \nabla_L^2 v \,\mathrm{d}\varphi = \int_0^{2\pi} \rho k \partial_\varphi \left(\cos\varphi \partial_x v + \sin\varphi \partial_y v\right) \,\mathrm{d}\varphi + \int_0^{2\pi} \rho \nabla_l^2 v \,\mathrm{d}\varphi \tag{7.19}$$

$$= \underbrace{k \int_0^{2\pi} \rho \left(-\sin\varphi \partial_x v + \cos\varphi \partial_y v\right) \,\mathrm{d}\varphi}_{\overline{k}\nabla_{\kappa_\nu}(v)} + \underbrace{\int_0^{2\pi} \rho(\varphi) \nabla_l^2 v \,\mathrm{d}\varphi}_{③} \tag{7.20}$$

What is missing is a formulation of integral ③ on the right hand of Eq. (7.20) in terms of averaged quantities. To this end we recall that after averaging we only can differentiate between homogeneously distributed ('statistically stored') dislocations with a constant density along orientation direction and a GND density ρ_G where the only available information concerning the distribution arrangement in angular space is the average GND line direction φ_G. Hence, expressing the averaged quantities of sCDD again in terms of the orientation space of CDD we have

$$\rho_\mathrm{S}(\varphi) = \frac{1}{2\pi}\left(\rho_\mathrm{t} - \rho_\mathrm{G}\right) \tag{7.21}$$

$$\rho_\mathrm{G}(\varphi) = \rho_\mathrm{G}\delta_{\varphi_\mathrm{G}} = \begin{cases} \rho_\mathrm{G} & \text{if} \quad \varphi = \varphi_\mathrm{G} \\ 0 & \text{otherwise} \end{cases} \tag{7.22}$$

In Eq. (7.22) $\delta_{\varphi_\mathrm{G}}$ is the Dirac delta function. Now we can proceed to derive an expression for integral ③:

③: With the definition $\rho(\varphi) = \rho_\mathrm{S}(\varphi) + \rho_\mathrm{G}(\varphi)$ and Eq. (7.22) we get the sum of two integrals

$$\int_0^{2\pi} \rho(\varphi) \nabla_l^2 v \,\mathrm{d}\varphi = \frac{\rho_\mathrm{t} - \rho_\mathrm{G}}{2\pi} \int_0^{2\pi} \nabla_l^2 v \,\mathrm{d}\varphi + \rho_\mathrm{G} \nabla_l^2 v, \tag{7.23}$$

where we used that $\rho_\mathrm{G}(\varphi)$ is non-vanishing only for a point φ_G. Explicitly writing the integrand of Eq. (7.23) and subsequent integration of the resulting terms yields

$$\int_0^{2\pi} \nabla_l^2 v \,\mathrm{d}\varphi = \int_0^{2\pi} \left(\cos^2\varphi \,\partial_{xx} v + \sin^2\varphi \,\partial_{yy} v + \sin\varphi\cos\varphi \,\partial_{xy} v\right) \,\mathrm{d}\varphi$$

$$= \pi\left(\partial_{xx} v + \partial_{yy} v\right) = \pi \nabla \cdot \nabla v \tag{7.24}$$

Now we can gather all expressions and insert them into Eq. (7.15) which gives us

$$\partial_t\left(\overline{\rho k}\right) = \frac{\rho_\mathrm{t} - \rho_\mathrm{G}}{2}\nabla\cdot\nabla v + \overline{k}\nabla_{\boldsymbol{\kappa}_\nu} v + \nabla_{\boldsymbol{\kappa}_\nu}(kv) + \rho_\mathrm{G}\nabla_{\boldsymbol{l}}^2 v. \tag{7.25}$$

The evolution of average curvature in sCDD is

$$\partial_t\overline{k} = \partial_t\left(\frac{\overline{\rho k}}{\rho_\mathrm{t}}\right) = \frac{1}{\rho_\mathrm{t}}\left(\partial_t\overline{\rho k} - \overline{k}\partial_t\rho_\mathrm{t}\right) \tag{7.26}$$

where we used $\overline{\rho k}/\rho_\mathrm{t} = \overline{k}$. Insertion of Eq. (7.8), Eq. (7.25) and applying the product rule to $\nabla_{\boldsymbol{\kappa}_\nu}(kv)$ yields the evolution of mean curvature

$$\begin{aligned}\partial_t\overline{k} = -v\overline{k}^2 &+ \frac{1}{2}\left(\frac{\rho_\mathrm{t} + \rho_\mathrm{G}}{\rho_\mathrm{t}}\nabla_{\boldsymbol{l}}^2 v + \frac{\rho_\mathrm{t} - \rho_\mathrm{G}}{\rho_\mathrm{t}}\nabla_{\boldsymbol{\nu}}^2 v\right) \\ &- \frac{1}{\rho_\mathrm{t}}\left(\overline{k}\nabla_{\boldsymbol{\kappa}_\nu} v - v\nabla_{\boldsymbol{\kappa}_\nu}\overline{k}\right).\end{aligned} \tag{7.27}$$

Here, the two successive gradient operators evaluate for instance for the first term as

$$\nabla_{\boldsymbol{l}}^2 v = \cos^2\varphi_\mathrm{G}\partial_{xx}v + 2\sin\varphi_\mathrm{G}\cos\varphi_\mathrm{G}\partial_{xy} + \sin^2\varphi_\mathrm{G}\partial_{yy}v. \tag{7.28}$$

$$= \frac{\kappa_x^2}{|\boldsymbol{\kappa}|^2}\partial_{xx}v + 2\frac{\kappa_x\kappa_y}{|\boldsymbol{\kappa}|^2}\partial_{xy} + \frac{\kappa_y^2}{|\boldsymbol{\kappa}|^2}\partial_{yy}v, \tag{7.29}$$

where we used Eq. (7.3) for the substitution of φ_G by the respective density ratios. Two extreme cases are represented by Eq. (7.27):

1. $\rho_\mathrm{t} = \rho_\mathrm{G}$: only GND density present, which implies a vanishing second term in the large bracketed formula such that

   $$\partial_t\overline{k} = -v\overline{k}^2 + \nabla_{\boldsymbol{l}}^2 v - \left(\overline{k}\nabla_{\boldsymbol{\nu}} v - v\nabla_{\boldsymbol{\nu}}\overline{k}\right), \tag{7.30}$$

   where we used that $\frac{1}{\rho_\mathrm{t}}\nabla_{\boldsymbol{\kappa}_\nu}(\cdot) = \nabla_{\boldsymbol{\nu}}(\cdot)$ for $\rho_\mathrm{t} = \rho_\mathrm{G}$.

   In the following section, Section 7.3, we show that this case is identical to the formulation Sedláček uses e.g. in Sedláček *et al.* (2003).

2. $\rho_\mathrm{G} = 0$: all dislocations are statistically homogeneous distributed, i.e.

   $$\kappa_x = \kappa_y \equiv 0. \tag{7.31}$$

We assume that $\nabla_{\boldsymbol{l}}^2 v + \nabla_{\boldsymbol{\nu}}^2$ results in the standard Laplace operator applied on v. Then Eq. (7.27) simplifies to

$$\partial_t \overline{k} = -v\overline{k}^2 + \partial_{xx} v + \partial_{yy} v. \tag{7.32}$$

Evolution of plastic distortion Here the density and velocity do not have the angular dependency. Thus, the integral in Eq. (4.27) vanishes and the equation for the plastic distortion simplifies to

$$\partial_t \beta^{\mathrm{pl}} = \rho_{\mathrm{t}} v \boldsymbol{n} \otimes \boldsymbol{b}, \tag{7.33}$$

which is exactly the Orowan equation in its original form.

7.3 Recovering Sedláček's theory from sCDD

The foundation of Sedláček's theory is a formulation for the evolution of so-called 'single-valued dislocation fields': those are fields of dislocations which are assumed to have the same orientation in an averaging volume (Sedláček *et al.*, 2003; Sedláček, 2004). This is essentially the same as in Kröner's classical continuum theory.

To circumvent the restriction of single-valued fields Sedláček introduces a density distribution function which is defined in a phase-space volume consisting of placement, orientation, curvature and time, similar to a function which is also used by El-Azab (2000). Sedláček's phase space essentially is a finite composition of single-valued dislocation fields. His theory is able to distinguish between a (geometrically necessary) distribution of loops and a distribution of parallel lines, which Kröner's density measure could not distinguish. One of the differences of this space with regard to our higher-dimensional configuration space is that it is rather a sum of single-valued fields, thus Sedláček's phase-space is not directly differentiable in e.g. φ direction. The main difference in terms of applicability is that in Hochrainer's theory - contrary to Sedláček's theory - the notion of 'geometrically necessary dislocation' and 'statistically stored dislocation' density becomes dispensable.

Sedláček's theory is governed by expressions for the GND dislocation density ρ_{G} and the line orientation φ. In this context, the curvature k is a derived quantity. The evolution is defined by the following equations (compare Eqns. (2.75) and (2.77) in Schwarz (2007))[2]:

$$\partial_t \rho_\mathrm{G} = \operatorname{div}(\rho_\mathrm{G} \boldsymbol{v}) + \rho_\mathrm{G} v k \tag{7.34}$$

$$\partial_t \varphi = v \operatorname{div}(\boldsymbol{l}) + \nabla_{\boldsymbol{l}} v. \tag{7.35}$$

Evolution of density Obviously, Eq. (7.34) is identical to Hochrainer's evolution equation Eq. (7.4) under the assumption that in each point only one line orientation prevails - the integrals vainshs and the term governing the angular transport as well.

Evolution of orientation The evolution of orientation is related to a gradient of velocity along the line direction (Schwarz, 2007) by

$$\rho_\mathrm{G} \partial_t \varphi = \nabla_{\boldsymbol{l}}(\rho_\mathrm{G} v). \tag{7.36}$$

We start the derivation at the equation of continuity ($\operatorname{div}(\rho \boldsymbol{l}) = 0$) which governs the solenoidality and assume that $\rho = \rho_\mathrm{G}$. Insertion of the definition of line orientation and multiplying by v we obtain

$$v \partial_x(\rho_\mathrm{G} \cos\varphi) + v \partial_y(\rho_\mathrm{G} \sin\varphi) = 0. \tag{7.37}$$

Application of the product rule gives

$$\partial_x(\rho_\mathrm{G} v \cos\varphi) - \rho_\mathrm{G} \partial_x(v \cos\varphi) + \partial_y(\rho_\mathrm{G} v \sin\varphi) - \rho_\mathrm{G} \partial_y(v \sin\varphi) = 0, \tag{7.38}$$

which can be rewritten as

$$\nabla_{\boldsymbol{l}}(\rho v) = \operatorname{div}(v \boldsymbol{l}). \tag{7.39}$$

Division by ρ_G and use of the identity $\operatorname{div}(a\boldsymbol{B}) = a \operatorname{div}(\boldsymbol{B}) + \operatorname{grad}(a) \cdot \boldsymbol{B}$ yields

$$\partial_t \varphi = \frac{1}{\rho_\mathrm{G}} \nabla_{\boldsymbol{L}}(\rho_\mathrm{G} v) = v \operatorname{div}(\boldsymbol{l}) + \nabla_{\boldsymbol{l}}(v), \tag{7.40}$$

which is identical to Eq. (7.35).

---

[2] Sedláček and Schwarz use slightly different notations and sign conventions; for ease of readability we already adjusted those to our conventions.

Evolution of curvature To proof that both theories are identical it was sufficient to show that the evolution equations for density and orientation are identical since the curvature is a dependent variable in Sedláček's concept. For the sake of completeness we give a derivation (originally by Hochrainer) and show that also the evolution of curvature is identical in both theories[3]. Point of departure is the relation $\partial_t \boldsymbol{l} = \boldsymbol{\nu}\partial_t \varphi$ and Eq. (7.40) giving

$$\partial_t \boldsymbol{l} = (\nabla_{\boldsymbol{l}} v + v \operatorname{div} \boldsymbol{l})\, \boldsymbol{\nu}. \tag{7.41}$$

From this we get the evolution of the normal as

$$\partial_t \boldsymbol{\nu} = -\,(\nabla_{\boldsymbol{l}} v + v \operatorname{div} \boldsymbol{l})\, \boldsymbol{l}. \tag{7.42}$$

Equation (10) in Sedláček *et al.* (2003) gives an expression for the curvature

$$k = -\operatorname{div} \boldsymbol{\nu}, \tag{7.43}$$

where we already used our sign convention. Taking the time derivative of k yields the desired evolution equations

$$\begin{aligned}
\partial_t k &= -\operatorname{div}(\partial_t \boldsymbol{\nu}) && (7.44)\\
&= -\nabla_{\boldsymbol{l}}^2 v - \nabla_{\nabla_{\boldsymbol{l}} \boldsymbol{l}} v + \nabla_{\boldsymbol{l}} v \operatorname{div} \boldsymbol{l} + v \nabla_{\boldsymbol{l}} \operatorname{div} \boldsymbol{l} - (\nabla_{\boldsymbol{l}} v - v \operatorname{div} \boldsymbol{l}) \cdot \operatorname{div} \boldsymbol{l} && (7.45)\\
&= -\nabla_{\boldsymbol{l}}^2 v + k \nabla_{\boldsymbol{\nu}} v + v\,(\nabla_{\boldsymbol{l}} \operatorname{div} \boldsymbol{l} + \operatorname{div} \boldsymbol{l} \cdot \operatorname{div} \boldsymbol{l})\,. && (7.46)
\end{aligned}$$

With the identity $\operatorname{div}(\operatorname{div} \boldsymbol{l} \cdot \boldsymbol{l}) = -\operatorname{div}(\operatorname{div} \boldsymbol{\nu} \cdot \boldsymbol{\nu}) = -\nabla_{\boldsymbol{\nu}} k - k^2$ (where we used that $|\boldsymbol{l}| = |\boldsymbol{\nu}| = 1$) we get

$$\partial_t k = -\nabla_{\boldsymbol{l}}^2 v + k \nabla_{\boldsymbol{\nu}} v - v \nabla_{\boldsymbol{\nu}} k - v k^2 \tag{7.47}$$

which is exactly the evolution equation for the curvature in sCDD from Eq. (7.27). Thus, both theories are fully identical.

---

[3] Schwarz (2007); Sedláček (2004) give an (erroneous) expression for the evolution of the mean curvature which coincides with Hochrainer's terms - except for the $\overline{k}\nabla_{\boldsymbol{\nu}} v$ term

Chapter 8
Comparison with CDD

8.1 Comparison with simple CDD test cases

It follows a brief comparison of the simplified variant of the CDD equations - in the following called sCDD - with the test cases shown in Section 5.2 for CDD.

Homogeneous distribution of expanding loops: sCDD can handle a homogeneous distribution of circular loops which expand with constant velocity (CDD test case Section 5.2): a homogeneous distribution in terms of sCDD amounts to a constant initial curvature k_0. Concerning the density, we have to prescribe three density fields: the total density $\rho_t \neq 0$ and $\kappa_x = \kappa_y = 0$. The evolution equation Eq. (7.27) simplifies to $\partial_t k = -vk^2$ in complete analogy to CDD. Instead of one evolution equation for the density in the configuration space, we now have to consider the evolution equation $\partial_t \rho_t$ in 2D space, while $\partial_t \kappa_x \equiv 0$ and $\partial_t \kappa_y \equiv 0$. This accounts for the fact that this system contains SSD density only. The evolution equation for the SSD density takes with $\partial_t \rho_t = \rho v k$ the same form as for CDD. Thus, both CDD and sCDD are fully equivalent for this test case.

Quasi-discrete expanding circular loop sCDD treats the expansion of a circular quasi-discrete loop correctly; the increase in line length is properly represented. No fragmentation as discussed for CDD in Section 5.2 occurs. The reason for this is that in sCDD no discretisation of the orientation space takes place. Again, CDD (with our remedy as introduced previously) and sCDD are equivalent.

Homogeneous distribution of expanding loops with anisotropic velocity A homogeneous distribution of e.g. elliptical loops (see Section 5.2) can not be represented by sCDD. This is due to one of the major assumptions of sCDD, namely that dislocations in the same spatial point must have the same scalar velocity.

Quasi-discrete expanding circular loop with anisotropic velocity The same argument as in the previous paragraph holds: sCDD in general cannot handle this case.

Distribution of loops and quasi-discrete loop in a constrained channel geometry As will be shown in Section 8.4, both theories yield nearly identical results for a loop distribution inside a constrained cell, which - as a two dimensional problem - already includes the one dimensional channel problem as a special case. The same holds for the quasi-discrete loop in a constrained channel, which is a special case of the loop distribution.

8.2 Comparison with CDD micro-bending

To see how the simplified model performs by comparison with CDD if applied to microbending (Chapter 6) we use the same material parameters, numerical setup and initial values: $k = 0$ and a density distribution that consists of SSD only, i.e. $\rho_\mathrm{t} = \mathrm{const}$, $\kappa_x = \kappa_y = 0$. Again, we assume a system that is homogeneous in y-direction. Therefore, the system now becomes truly one-dimensional and κ_y stays zero. As parameters we again use $h = 3000\mathrm{nm}$ and a constant bending moment $M = 5 \cdot 10^{13}$ GPa m^2 as in Section 6.

Field values at converged state

It is striking when comparing CDD to sCDD how good the match of basically all data is (Fig. 8.1). Only the curvature (Fig. 8.1(c)) exhibits some deviations.

To understand the reason for the good match *despite the differences in curvature* we note the fact that the curvature's influence on the evolution of density is basically nil: the curvature is non-vanishing only in regions where the velocity is almost zero and therefore does not give any contribution to the line production term $\rho v k$. Furthermore, for this particular bending problem the velocity does not depend on the line orientation. As a consequence the evolution equations for ρ and k (ρ_t, κ_x and κ_y for sCDD respectively) are essentially decoupled. The velocity used with this model problem fully conforms with the requirements for the sCDD, i.e. it has no variations in angular direction, which explains why the results are exactly the same.

Why is there a discrepancy in curvature (Fig. 8.1(c)) at all? The curvature distribution in the configuration space as shown in Fig. 6.3 is very inhomogeneous in direction of line orientation. This curvature increase directly at the elastic core is physically sound. It can however only be interpreted as the curvature of those screw dislocations which are located at the kink between the plastic and elastic regime. The φ dependency violates the simplifying assumption in sCDD that all segments - irrespective of orientation - share the same local curvature. This causes a slight discrepancy.

Resulting evolution equations

For the bending example the evolution equations can be further simplified:

For sCDD we have only purely spatial evolution equations, $\partial_t \rho_t$ Eq. (7.8), $\partial_t \kappa_x$, $\partial_t \kappa_y$ Eq. (7.9). The system under consideration is homogeneous in y-direction and thus all derivatives in this direction vanish. For this case the evolution equations become

$$\partial_t \rho_t = -\left(\partial_x \left(\kappa_y v\right) - \partial_y \left(\kappa_x v\right)\right), \tag{8.1}$$

$$\partial_t \kappa_x = -\partial_x(\rho v) \quad \text{and} \quad \partial_t \kappa_y = -\partial_y(\rho v) \tag{8.2}$$

Here we made the simplification by assuming that (i) the curvature is very small and (ii) the curvature is only nonzero in regions where very little dislocation activity takes place, i.e. directly at the beginning of the elastic core for density with screw orientation. This justifies to neglect the source term for density.

For CDD the term responsible for the angular transport component (cf. Appendix A for the explicit formulation of ϑ) becomes

$$\partial_\varphi(\rho\vartheta) = -\left(\cos\varphi \partial_\varphi \rho - \rho \sin\varphi\right) \partial_x v, \tag{8.3}$$

where we used that $\partial_\varphi v = 0$. For the spatially one-dimensional system we then obtain for the evolution equation of scalar density Eq. (4.24)

$$\partial_t \rho = -\partial_x(\sin\varphi v \rho) + \rho \cos\varphi \partial_\varphi v, \tag{8.4}$$

where the first term governs the spatial transport and the second term the angular transport.

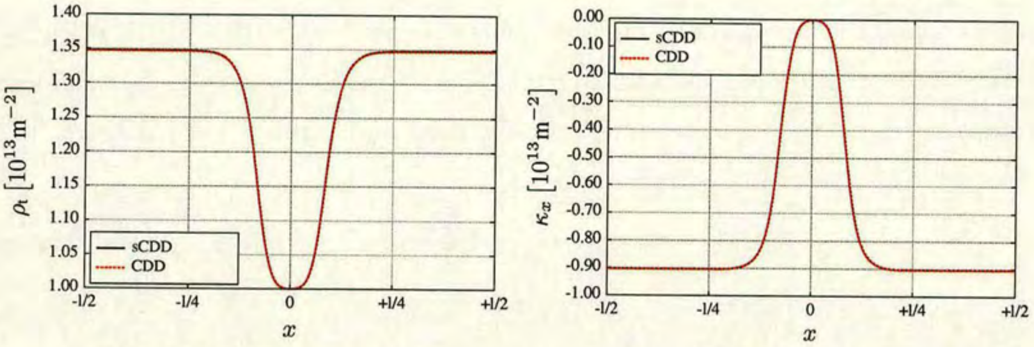

(a) total dislocation density ρ_t

(b) GND density κ_x

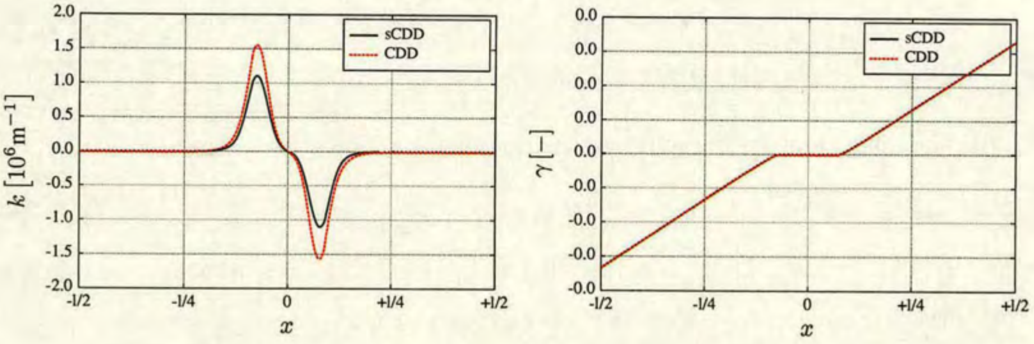

(c) Curvature

(d) Accumulated plastic strain

Figure 8.1: *Density, curvature and plastic strain profiles for CDD and sCDD*

Computational cost

Fig. 8.2 compares the adaptively chosen step sizes of the time integration schemes, which are necessary to achieve a constant prescribed accuracy. CDD's step size, Fig. 8.2, is slightly smaller due to the more complex configuration space. For reaching converged state it took CDD about 3300 steps and sCDD about 2500 steps.

The average computational cost per step on a 2.4 GHz quad core work station is about 8.7 seconds for CDD and 0.2 seconds for sCDD, which is a speedup factor of about 45. The memory requirement of sCDD is $1/50$-th of CDD. Comparing this to the speedup factor shows that the problem scales fairly well within our implementation[1].

---

[1] Our main objective, though, was not a highly efficient implementation but rather a versatile toolkit for running various numerical experiments

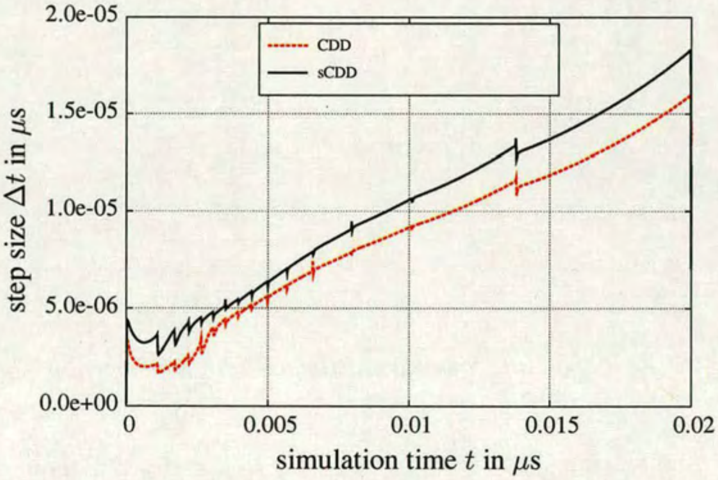

Figure 8.2: *Adaptively adjusted step sizes used for the time integration scheme for CDD and sCDD. At* $t = 0.02\,\mu s$ *both systems reached the quasi-static converged state where the dislocation velocity is approximately zero.*

8.3 Distribution of straight line segments in a constrained quadratic cell

In the following we investigate a two dimensional quadratic geometry with both CDD and sCDD. We assume the walls of the cell to be impenetrable for dislocations. This we model by a boundary layer within which the velocity drops from a constant value to zero directly at the wall as shown in Fig. 8.3(a) and Fig. 8.3(b). The velocity is constant for all φ.

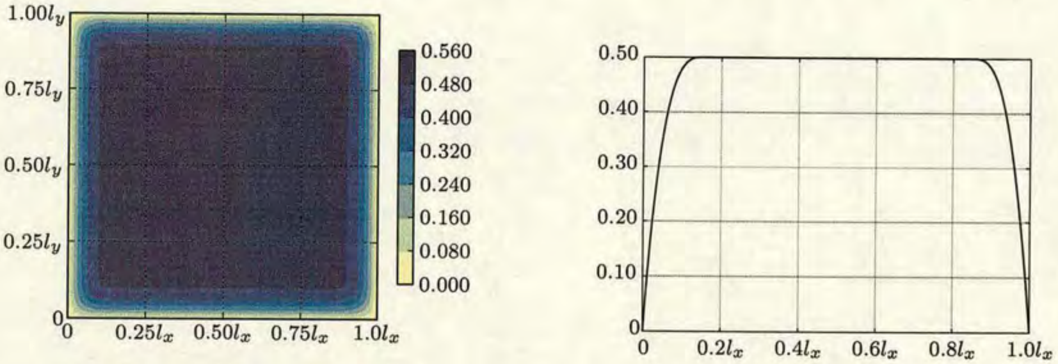

(a) sCDD and CDD: scalar velocity v.

(b) velocity profile: cut through the middle of Fig.8.3(a) at $0.5l_y$

Figure 8.3: *Velocity function for a quadratic cell with impenetrable boundaries.*

The velocity profile has the shape shown in Fig. 8.3 in x and y direction. To represent a statistically homogeneous distribution of straight line segments as our initial conditions we use a constant $\rho_t = 0.1$ and a zero κ_x and κ_y together with $k = 0$. Thus, initially we only have SSD density and no GND density. Evolving this system for a duration of $t = 2$ we obtain distributions as shown in Fig. 8.4 and Fig. 8.5.

Most striking is the good match of nearly all variables in the 'field area' (the region which has constant prescribed velocity). The reason is that in this region only convection of dislocations takes place. No change in curvature is expected due to the constant velocity. Approaching the boundary density gets hindered and accumulates at the impenetrable wall. Since only dislocations with orientation parallel to the wall may exist directly at the wall (compare the study of rotational velocity in a constrained channel for CDD in Section 5.2) the GND density increases towards the boundary - an effect which is also captured by sCDD although with some deviations from the values of CDD, cf. Fig. 8.4(e). Responsible for the deviation is the initial condition of the density: also in the boundary layer line segments of all directions are present which causes them to rotate faster or slower depending on their orientation. This, however, concerns the assumptions one had to make for sCDD: the assumption that dislocations of all orientations in one point have the same velocity and curvature is violated here. Thus, this example demonstrates the impact of the simplifying assumption: we do observe a deviation, which is however not severe.

The last features to be discussed here are the maxima of curvature in the corners (Fig. 8.5(a) and Fig. 8.5(c)): they correspond to line segments that bend when approaching the corner. This is quite nicely represented by sCDD.

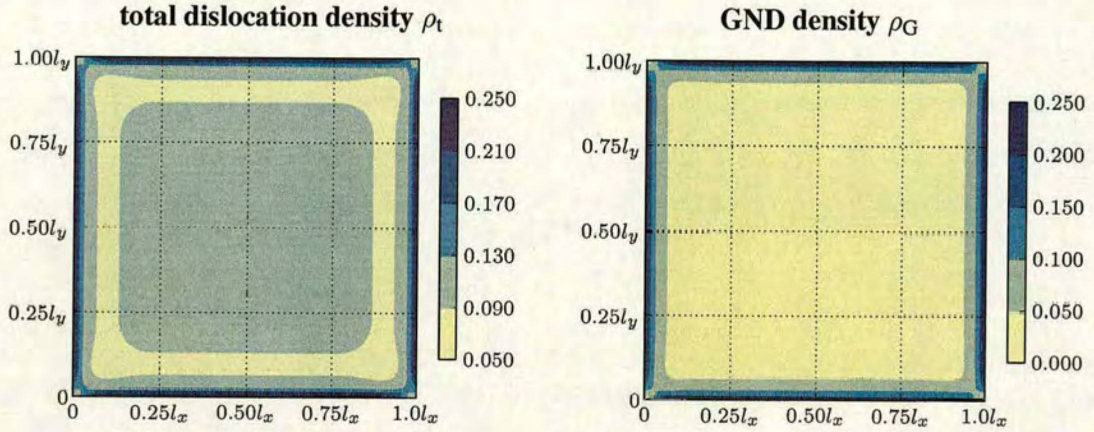

(a) sCDD

(b) sCDD

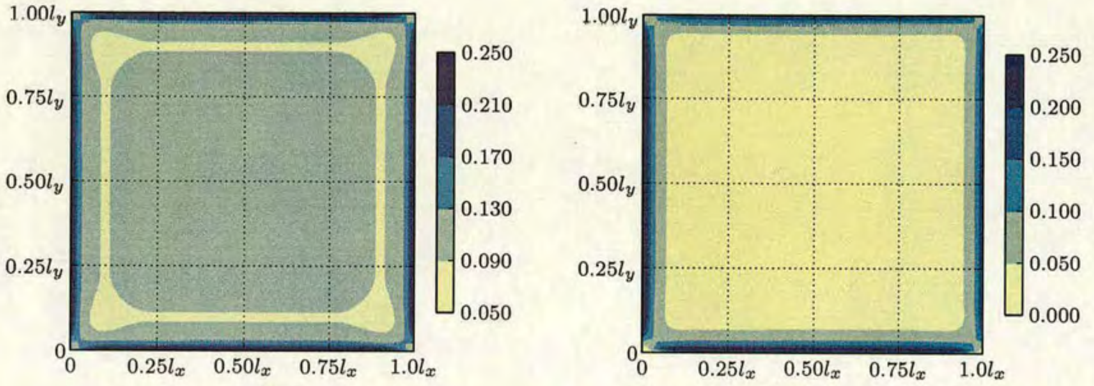

(c) CDD

(d) CDD

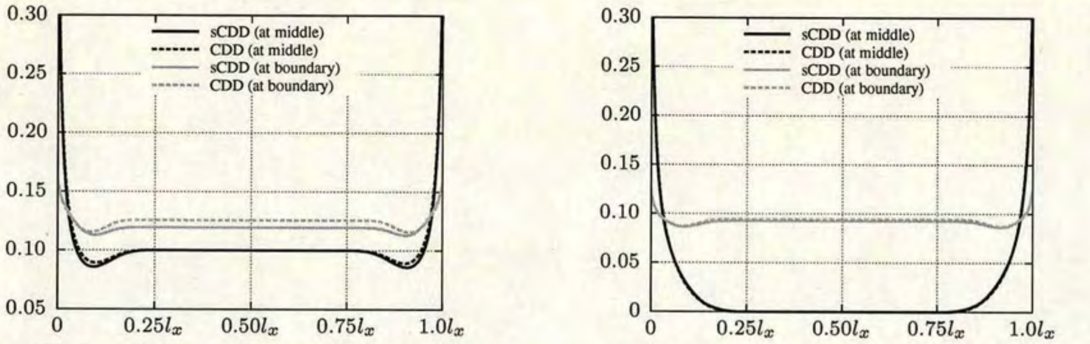

(e) Profile of ρ_S at $y = 0.033l_y$ (black lines) and at $y = 0.50l_y$ (grey lines).

(f) Profile of κ at $y = 0.033l_y$ (black lines) and at $y = 0.50l_y$ (grey lines),

Figure 8.4: *Scalar density (left column) and GND density (right column) at $t = 2$ for a quadratic cell with impenetrable boundaries. We compare the values obtained from CDD and sCDD.*

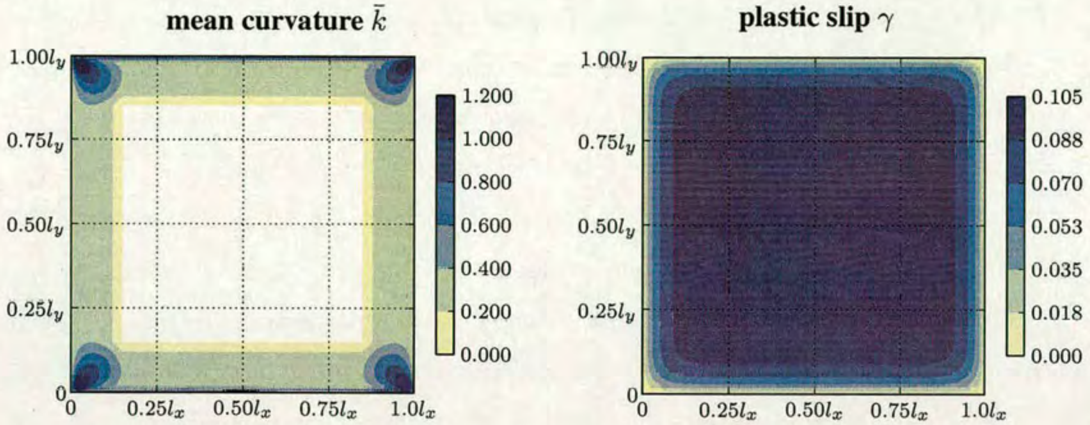

(a) sCDD

(b) sCDD

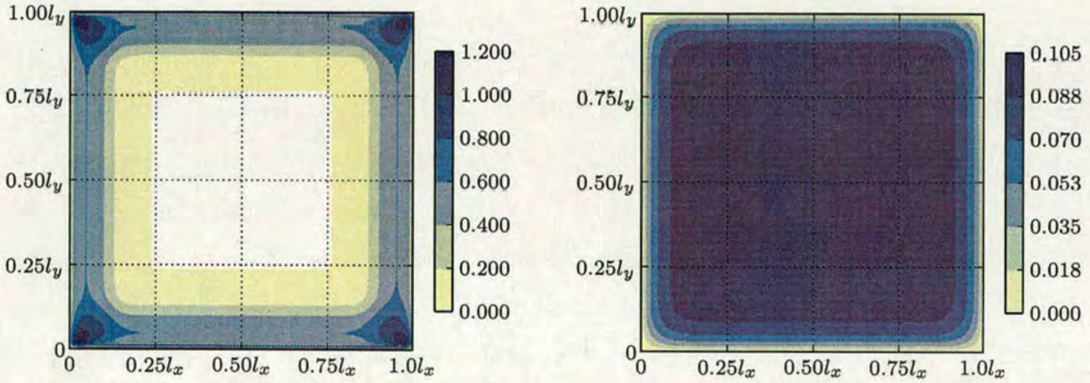

(c) CDD

(d) CDD

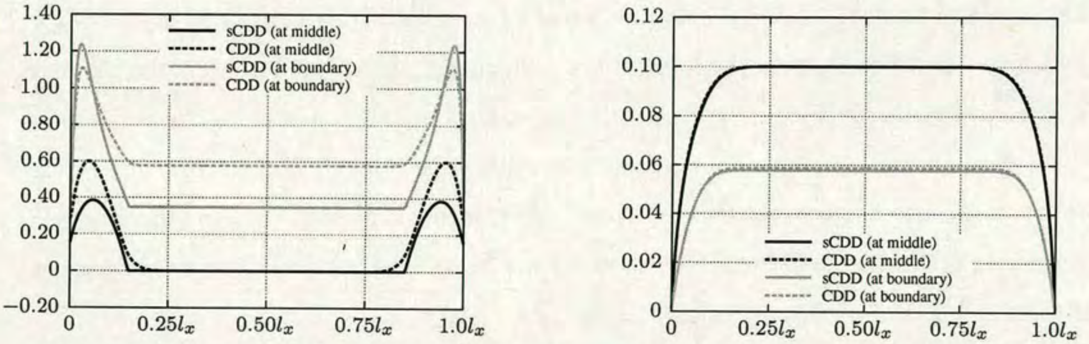

(e) Profile of $\bar{k}$ at $y = 0.033l_y$ (black lines) and at $y = 0.50l_y$ (grey lines).

(f) Profile of γ at $y = 0.033l_y$ (black lines) and at $y = 0.50l_y$ (grey lines),

Figure 8.5: *Curvature (left column) and plastic slip (right column) at $t = 2$ for a quadratic cell with impenetrable boundaries. We compare the values obtained from CDD and sCDD.*

8.4 Distribution of circular loops in a constrained quadratic cell

The second example with the same quadratic geometry shows the evolution of a distribution of initially circular dislocation loops. The initial values for the density fields were created by copying 'smeared out' circular loops. As a result, there is only density of a certain parallel orientation directly at the wall (or in the boundary layer). This procedure was explained in more detail in Section 5.2. The resulting initial values are shown in Fig. 8.6. Note that the density initially already has GND components. From these figures cannot be seen that the curvature in CDD is changing in some areas along the orientation axis similar to Fig. 5.14(d) (this figure represents about the same situation as found along the middle of the cell). The curvature variations in orientation direction cannot be represented by sCDD. The velocity function is the same as in the previous example.

Evolving the systems for $t = 3$ results in the values shown in Fig. 8.7 and Fig. 8.8. We find an excellent match of all data. The match of evolved mean curvature data Fig. 8.8(e) again is slightly worse than the other data. This again must be credited to the assumption of orientation independant curvature in sCDD, which is slightly violated in some areas right from the beginning, as mentioned before. To understand the cause of the two bumps in the curvature (Fig. 8.8(e), the line for the cut through the middle) we take a look at the curvature in the configuration space (x, φ). This is shown in Fig. 5.14 where we investigated the constrained channel for CDD (the middle of the quadratic cell is almost identical to the homogneous channel). The bumbs correspond to the smallish dark spots in Fig. 5.14(d), which we identified as corresponding to loops which get partially deposited at the channel wall and partially are rotating towards perpendicularly orientation w.r.t. to the wall, such that inbetween these two sections a localised kink has to be formed. This situation, however, is applicable only for very special situations/loop placements, which shows in the inhomogeneity in φ direction. These information are not being kept within sCDD and hence the difference between the two theories.

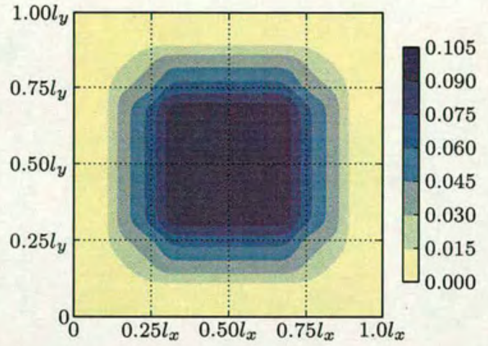

(a) scalar dislocation density max $\rho_t = 0.1$

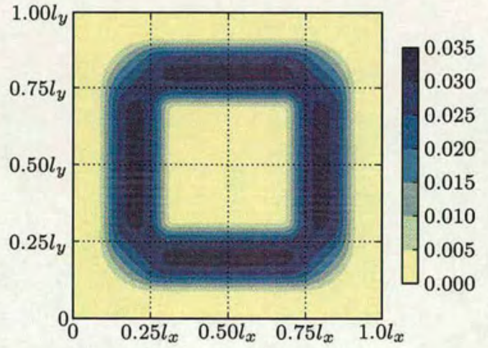

(b) ρ_G

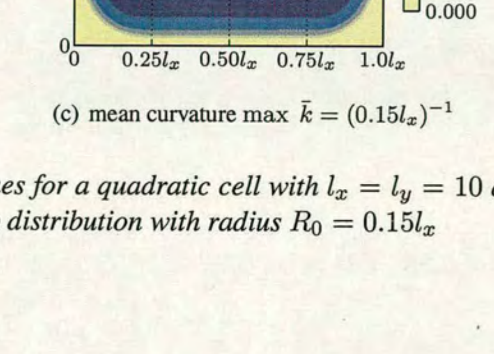

(c) mean curvature max $\bar{k} = (0.15l_x)^{-1}$

Figure 8.6: *Initial values for a quadratic cell with* $l_x = l_y = 10$ *and impenetrable boundaries: loop distribution with radius* $R_0 = 0.15l_x$

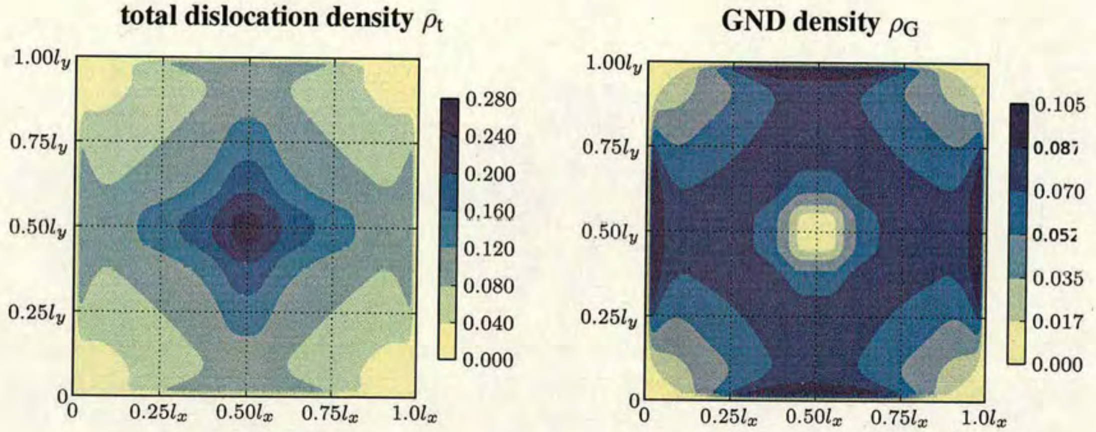

(a) sCDD

(b) sCDD

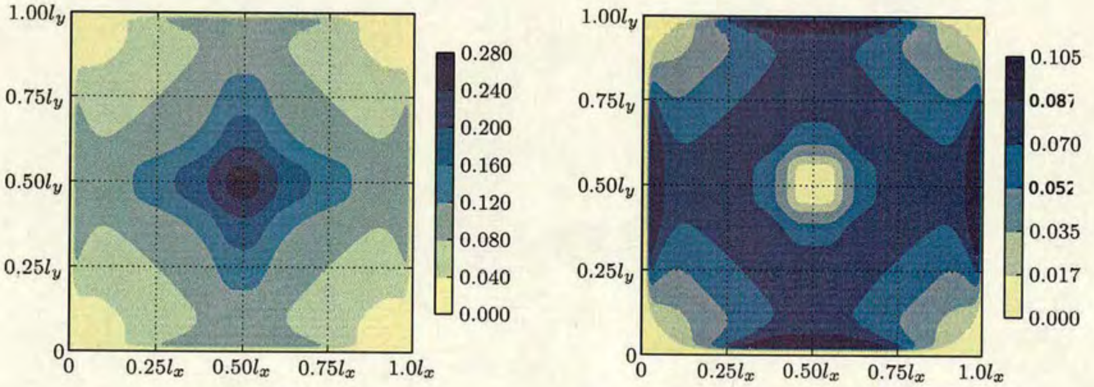

(c) CDD

(d) CDD

(e) Profile of ρ_t at $y = 0.033l_y$ (grey lines) and at $y = 0.50l_y$ (black lines).

(f) Profile of ρ_G at $y = 0.033l_y$ (grey lines) and at $y = 0.50l_y$ (black lines),

Figure 8.7: *Scalar density (left column) and GND density (right column) at* $t = 3$ *with* $v = 0.5$ *for a quadratic cell with impenetrable boundaries. We compare the values obtained from CDD vs. sCDD.*

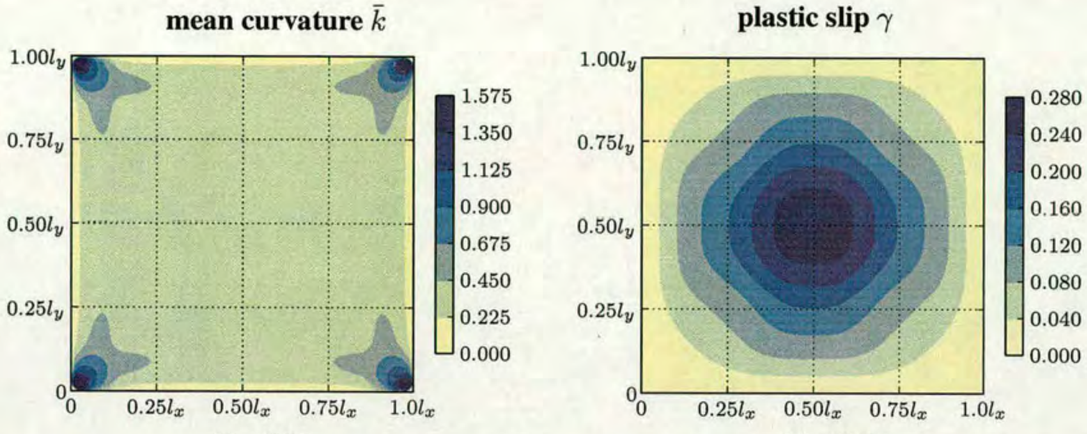

(a) sCDD

(b) sCDD

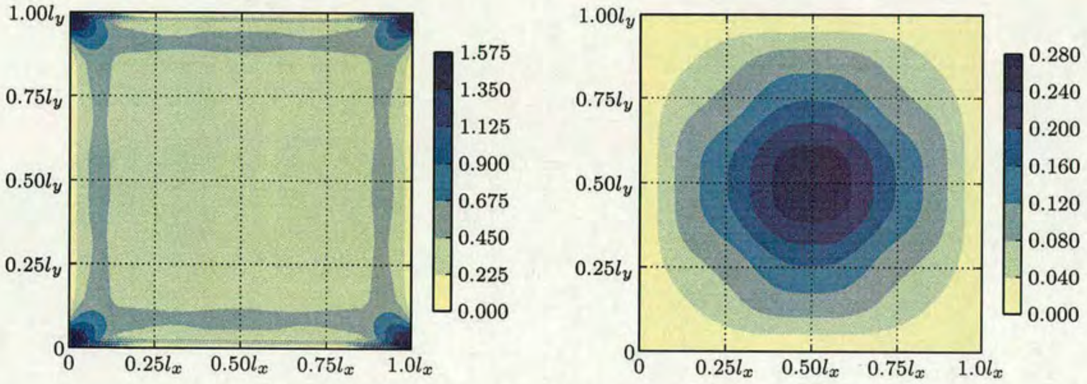

(c) CDD

(d) CDD

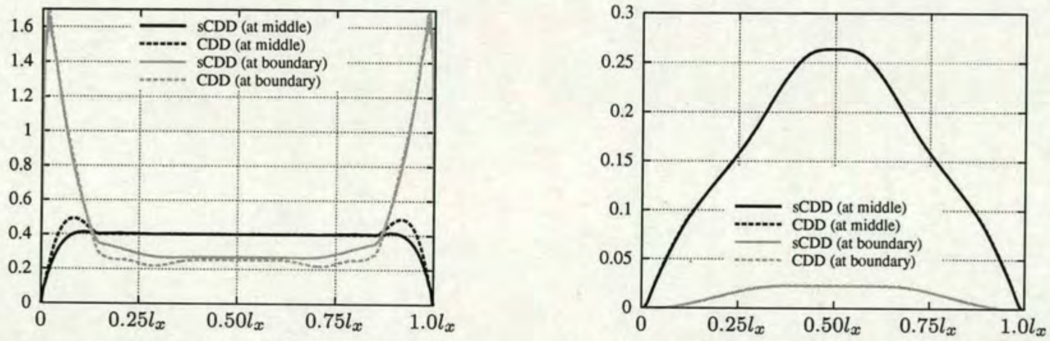

(e) Horizontal cut through $\bar{k}$ at $y = 0.033l_y$ (grez lines) and at $y = 0.50l_y$ (black lines).

(f) Horizontal cut through γ at $y = 0.033l_y$ (grez lines) and at $y = 0.50l_y$ (black lines),

Figure 8.8: *Curvature (left column) and plastic slip (right column) at $t = 2$ for a quadratic cell with impenetrable boundaries. We compare the values obtained from CDD vs. sCDD.*

Part IV

The Dynamics of CDD: Stress Fields and Dislocation Interaction

Chapter 9
Introduction: The problem of dynamic closure

CDD and sCDD represent systematically derived continuum theories for the kinematic evolution of continuous dislocation systems. A kinematic formulation, however, can only be the foundation for a physical continuum theory which in addition needs to describe the interactions between dislocations or the corresponding density distributions.

9.1 Dislocation interactions

There is a whole manifold of dislocation interactions. Among them are short range interactions, which are governed by atomistic processes in the dislocation cores, such as dislocation annihilation, jog formation, or the core interaction during dislocation intersection. Representation of those phenomena pose a very particular class of problems for a continuum theory, since generally in an efficient implementation (from the point of view of computational cost) one postulates that the discretisation of e.g. the density field is relatively coarse w.r.t. to the inter-dislocation spacing in real materials. Additionally, as opposed to dislocation movement, which is assumed to be continuous, intersections happen only at discrete moments of time, which necessitates a concept for temporal averaging. Within this thesis we do not consider these issues.

A different class of dislocation interactions is related to the elastic stress field emanating from dislocation lines. Stresses are for instance responsible for the line tension effect (i.e. self interaction of a dislocation loop), the dislocation forest hardening (i.e. junction formation) and formation of dislocation dipoles - both responsible for the yield stress, and the back stress due to repulsion of dislocations of the same sign.

In the following sections we shall discuss the treatment of dislocation interactions which can be represented by internal stress fields within our continuum theory. We first introduce the stress field of a single dislocation and then consider necessary steps leading to a field theory.

9.2 Stress fields of discrete dislocation lines

A dislocation line as introduced in Chapter 2 is the result of a Volterra cut. The resulting distortion causes a stress field inside the crystal which can be computed analytically for special cases (e.g. Hirth & Lothe, 1982; de Wit, 1967) or numerically for arbitrary dislocation arrangements (e.g. Ghoniem & Sun, 1999). Paradoxically, dislocation-based plasticity is thus strongly linked to elasticity theory as long as the influence of the dislocation core is neglected. Approaching the dislocation core one usually defines a cut-off distance in the range of few Burgers vectors in order to avoid the diverging behavior of the stress function. Below this cut-off distance standard elasticity breaks down and the influence of atomistic effects becomes pronounced. When moving further away from the core it is important to note that the stress field decays proportionally to $1/r$ and thus prevents any straightforward approximation which would use a cut-off. It is this long-ranged nature of the stress field which is responsible for the fact that computation of the elastic stress fields of dislocation micro-structures e.g. in discrete dislocation dynamic (DDD) simulation[1] is numerically very expensive (the computational time is proportional to the square of the number of interacting line segments). In fact, the number of interacting dislocations is one of the limiting factors which prevents DDD from being applied to specimens larger than a few microns with typical dislocation densities as observed in experiments.

9.3 The problem of dynamic closure

This gives rise to the question how stress fields of dislocation systems can be represented in our continuum theory. Or - in other words - how much and in particular which information gets lost through the averaging procedure that was applied in order to obtain a continuous density distribution? How can this information be recovered?

Already in Section 3.1 we pointed out that if the 'spatial resolution' were arbitrarily high the Kröner-Nye tensor would be a proper measure for the dislocation state of a crystal (since then all dislocations are separately resolved and thus 'geometrically necessary'). This

---

[1] The discrete dislocation dynamics simulation approach allows to describe the plastic flow of crystals based on tracking the glide of discrete line segments. Those are represented in simple models by pure screw and edge dislocation segments (Kubin & Canova, 1992; Fivel *et al.*, 1997; Verdier *et al.*, 1998), or by pure screw and edge segments with one intermediate orientation (Bulatov & Cai, 2006) In more recent models dislocations are represented by a decomposition into a sequence of straight and arbitrarily oriented segments (Weygand *et al.*, 2002; Bulatov & W., 2002; Arsenlis *et al.*, 2007) or by a higher order interpolation scheme such as cubic splines (Ghoniem & Sun, 1999).

averaging problem of kinematics could be solved by the specific higher-order averaging of CDD, which closes our continuum theory kinematically. When it comes to determining the stress fields within a continuum theory it is again the spatial resolution that it responsible for the *averaging problem of dynamics*. This problem can be formulated in the following way:

Closure Problem of Dynamics

① CDD is a purely kinematic theory

② Dislocation velocities depend on stresses

③ Stresses depend on the dislocation configuration (microstructural information) and boundary conditions

closure problem: express the stresses in terms of the same field variables that enter the kinematic description without losing relevant information

In previous chapters we closed the dynamic problem by making constitutive assumptions, e.g. for the expanding quasi-discrete loop in Chapter 5 we assumed a constant velocity in magnitude, which in fact implies a stress dependency on the kinematic field variables in the form $\tau(\rho, k) = \text{const}$; similarly in Chapter 6 where we investigated bending of a thin film prescribing a more elaborate but nonetheless constitutive kinematic relationship in Eq. (6.4).

In the following we propose a method for obtaining these stress fields, which is suitable for a continuum description of general dislocation configurations with arbitrary loading (e.g. stress or strain driven) and arbitrary boundary conditions. We start by assuming that the spatial resolution is such that we can resolve and distinguish between single dislocations. Subsequently, as we proceed to a coarser resolution we analyse which information has been lost upon averaging and show how this information can be recovered.

Chapter 10

Numerical method for stress fields of systems of dislocations

10.1 Numerical standard procedure

A dislocation is a discontinuity of the plastic distortion in form of a step change in the plastic shear strain γ on a certain crystallographic plane. Obtaining the resulting inhomogeneous stress and strain fields within the whole body which contains the dislocations poses a boundary value problem (BVP) which can in principle be solved by a standard method (e.g. Van der Giessen & Needleman, 1995; Weygand *et al.*, 2002). This requires to decompose the BVP into three separate problems: We start by considering the body as embedded into an infinite reference body and solve the problem of the internal stress state arising from the inhomogeneous shear strain field γ in the infinite body in special cases through analytical expressions or by evaluating an appropriate Green's function (e.g. Zaiser & Moretti, 2005). Subsequently, the free-surface boundary conditions have to be restored by applying the appropriate tractions on the actual surface of the deforming (non-infinite) reference body. Finally, one has to account for the stresses arising from these tractions as well as from any other displacements that are prescribed on the surface. Although in principle possible and well-established, this method in practice is rather difficult to implement for general geometries for which the computational cost is high.

10.2 A method of solving the BVP in a continuum setting

Alternatively, one can more directly consider the plastic distortion as an eigenstrain (see Eshelby (1951) and Weinberger *et al.* (2005) for an introduction) of the body: the plastic strain caused by the moving dislocation leaves the elastic continuum in a distorted although compact state (i.e. the total distortion is compatible as defined in Section 3.1). The solution of this elastic eigenstrain problem yields the desired stress state. Similar approaches were proposed in Lemarchand (1999); Lemarchand *et al.* (2001) for the context of DDD simulations. In the context of continuum theories Roy and Acharya proposed a 'Finite element approximation of field dislocation mechanics' (Roy & Acharya, 2004).

As a preparation for the solution of the BVP in a continuum setting we firstly introduce the general solution for a plastically deformed sub volume V in an elastic matrix. To evaluate the corresponding stress state we follow the steps as outlined in Fig. 10.1.

① We cut the volume V out of the surrounding matrix such that the surfaces ∂V are free. The volume is now stress free and has total deformation β^{pl}.

② To embed the volume V back into the matrix, we evaluate the surface tractions f_0 that would have acted on ∂V in order to produce the deformations β^{pl} in an elastic manner. Conversely, we can restore the undeformed shape of V by applying $-f_0$.

③ We can now embed V back into the matrix and restore connectivity. The surface forces f_0 which are needed to offset the previously applied surface forces $-f_0$ now cause an elastic relaxation of both the matrix and the embedded volume. For this elastic BVP the resulting stress state can be evaluated by using standard methods.

④ We add the stresses resulting from steps ② and ③.

Figure 10.1: *General solution for a plastically deformed sub volume*

To elucidate this method for our BVP under consideration we now consider a single edge dislocation which is moved from outside the crystal into the center of the crystal (Fig. 10.2). The generalisation to many, curved dislocations in three dimensions follows the same idea and does not pose any additional conceptual problems. We assume that the elastic problem will be solved by means of a standard Galerkin finite element method (e.g. Bathe, 2001) which introduces a discretisation of the volume. For the problem under consideration the

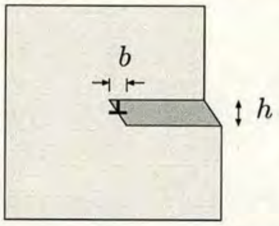

Figure 10.2: *Edge dislocation which was moved from the right into the center of a (originally quadratic) body*

edged dislocation causes the eigenstrain b/h in the dark shaded area in Fig. 10.2, where $h > b$ is the mesh width of the discretisation of the volume. The eigenstrain of the light shaded area is zero. All eigenstrains are prescribed at the respective Gauss points of the finite element from which equivalent nodal forces f_0 can be obtained (compare Fig. 10.3). The subsequent steps are the same as for the general solution. A numerical example where we study a single edge dislocation with our method is shown in Appendix B.

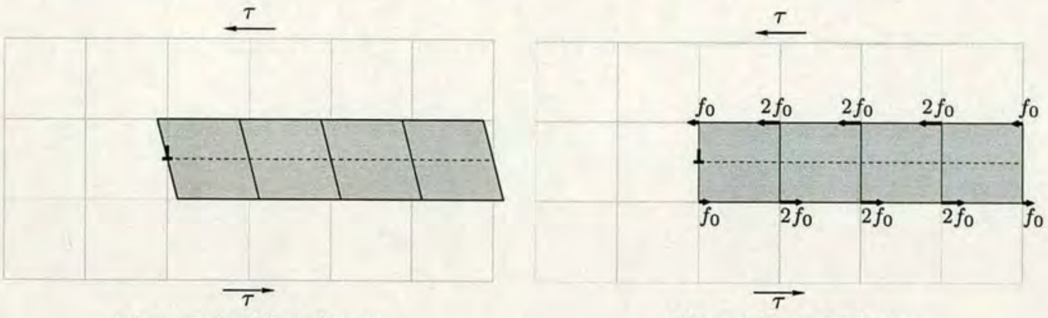

(a) prestrained free elements

(b) resulting nodal forces

Figure 10.3: *The plastic distortion due to a dislocation, which entered from the right, causes eigenstrains for free elements (a) which then can be applied as equivalent forces to the full system (b).*

The advantage of this procedure for obtaining stress fields of dislocations is that it can be applied to general strain fields and, due to the use of standard finite element solver, can be applied to arbitrary geometries. So far our eigenstrain-based method was used to describe stress fields on scales on which also the plastic distortion is resolved. If we resolve β^{pl} on scale b, we retain complete information about the internal stress field. However, if in a density based theory β^{pl} is resolved only on the scale of the field variables ρ and k (i.e. on scales well above the spacing of individual dislocations) then information about the interactions of individual dislocations is necessarily lost.

This gives rise to the question how we handle the situation where the resolution of the kinematic fields is such that single dislocations can not be resolved separately anymore but are represented by smooth density fields. The answer to this question will be given in the next chapter.

Chapter 11
Coarse-graining: towards continuous systems

This chapter considers the question which information exactly get lost upon coarse-graining and how they can be recovered.

11.1 Mean field stress

A very simplistic example elucidates the setting of the problem: imagine a statistically homogeneous distribution of slip planes in z direction. Each plane contains in the middle (x=$l_x/2$) a in y direction homogeneous distribution of dislocation sources, all of which simultaneously emit dislocations. They move in x direction only, parallel to the Burgers vector. Eventually, the dislocations' movement will be hindered by an impenetrable wall (possibly a grain boundary) located at each end of the slip planes. Dislocations interact elastically and pile up against the boundary. Fig. 11.1 shows the left part of one slip plane excluding the source, where dislocations entered from the right and moved towards the impenetrable wall at the left. There, the finely meshed areas contain the slip planes which are located at random positions. For this system we are not concerned whether an equilibrium state was reached or not but simply take the dislocation configuration as given. We are concerned about how the continuous pendant in Fig. 11.1(b) compares to the discrete situation shown on top of Fig. 11.1(b).

For this purpose we use the eigenstrain method from the previous chapter to compute the elastic stress fields of both configuration. Note, that both systems contain the same Net-Burgers vector. This can be achieved by first defining the density, e.g. by an inverse exponential function, $a_1 e^{-a_2 x}$ where a_1 and a_2 are positive constants and x denotes the distance from the left wall. Then, we integrate the density along the x-axis (this gives the Net-Burgers vector for this distance), until the Net-Burgers vector becomes exactly $1b$. This determines the ordinate of an edge dislocation of Burgers vector b. We restart integrating at this point and repeat the procedure for the whole slip plane width. We assume that all slip

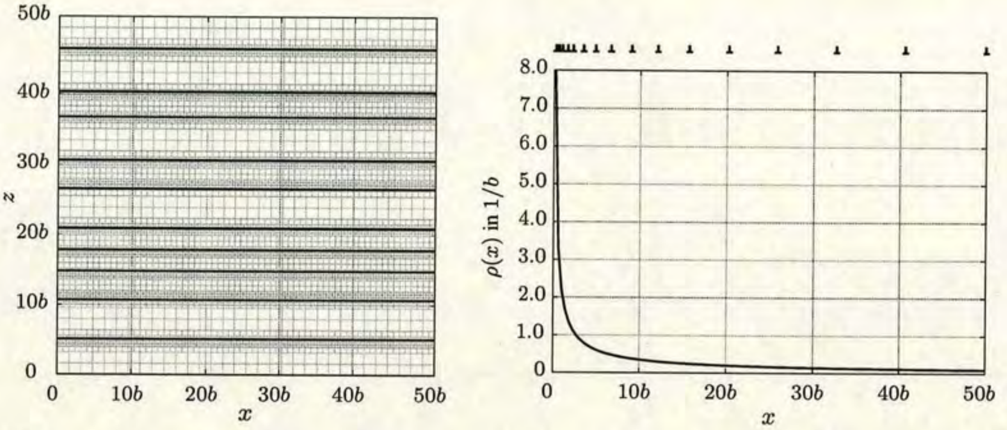

(a) FE mesh, perpendicular to the xy-slip planes (= dark lines)

(b) density distribution along *one* slip plane and position of 17 edge dislocations (on top of the diagram), both resulting in Net-Burgers vector $b = 4.774$nm

Figure 11.1: *Dislocation pile-up at impenetrable boundary (at $x = 0$). The finely meshed regions in (a) contain a slip plane each. The discrete system and continuous density is shown in (b) (position of edge dislocations symbolised by upside-down '*T*')*

planes have the same dislocation content. Now we choose the finite element mesh resolution for the discrete system such that individual dislocation can be resolved, i.e. the element size should be $\leq b$. The continuous system does not benefit from a fine resolution and we can use a significantly coarser mesh. The system is loaded by prescribing eigenstrains only, no external applied forces or prescribed displacement boundary conditions are present.

In Fig. 11.2 the resulting stresses for a system based on a distribution of single edge dislocations and the equivalent continuous density are compared. We observe that the level of stress of the coarse-grained system is always below the average stress of the discrete systems and tends to zero. The reason is the scale on which the stress is defined: it is defined on the same scale as the dislocation density and the plastic strain, which is much larger than the average dislocation spacing. As a result also this *mean field* stress τ_{mf}, caused by an inhomogeneous plastic strain γ, is defined on a scale much above the average dislocation spacing. Therefore, all information below this scale get lost (cf. Nikitas (2008); Zaiser & Seeger (2002) and references therein), which can be seen by the almost vanishing mean field stress in Fig. 11.2. In particular, fluctuations of the stress field of individually resolved dislocations (as shown by the dashed line in Fig. 11.2) get lost upon averaging.

Besides dislocation pile-ups there is another important test case, which can not be represented by the mean field stress: imagine a statistically homogeneous distribution of edge

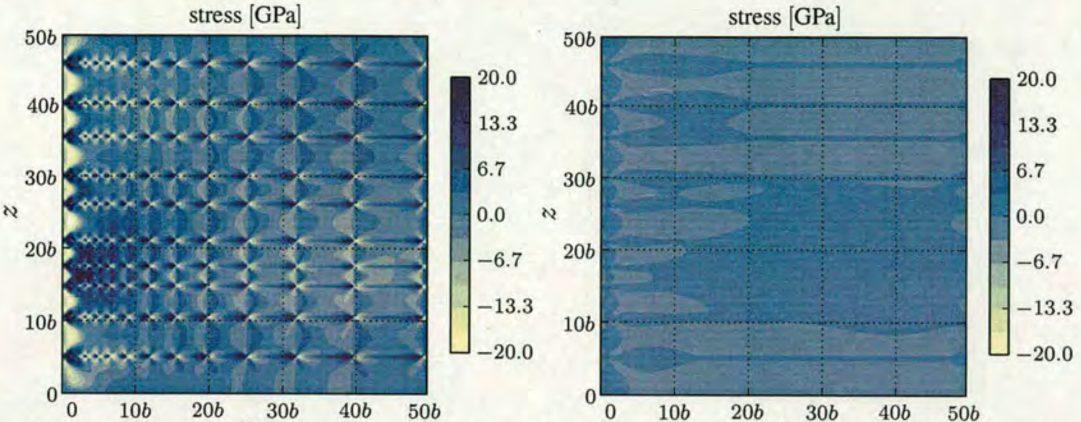

(a) discrete system

(b) continuous system

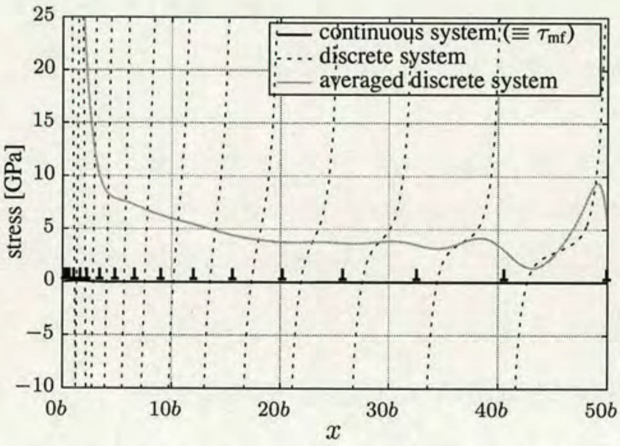

(c) stress profile along a slip plane ($z = 18b$): the mean field stress is almost zero

Figure 11.2: *Stresses for continuous and discrete system of edge dislocations. The averaged value was obtained from the dashed line by convolution with a gauss function. The elastic modulus was* $E = 72.7\text{GPa}$, *Poisson's ratio was* $\nu = 0.347$.

dislocations of positive and negative orientation which gives the stress field shown in Fig. 11.3. We used a number of 850 dislocations of each direction, the Burgers vector was $b = 0.2864\text{nm}$. Dislocations moving along a (dislocation free) path through the dislocation ensemble have to overcome the local stress peak values shown in Fig. 11.3(b) to be able to move, which governs the onset of plasticity. In a mean field description the corresponding dislocation density is constant and although the system is distorted due to non-zero shear strains, the resulting stresses are zero nonetheless. Therefore, dislocations immediately begin to move irrespective of the amount of resolved stress, which is quite contrary to experimental observations or results from DDD simulations where a certain level of stress has to be overcome prior to dislocation activity.

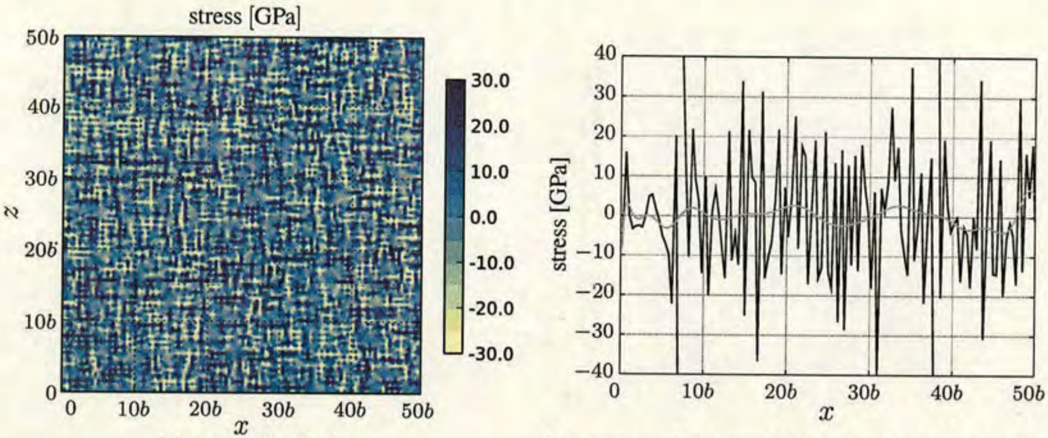

(a) stress distribution

(b) stress profile (along dislocation-free path) and average stress at $y = 25b$

Figure 11.3: *Stress field of statistically homogeneous distribution of edge dislocations*

In a mean field theory - as for instance CDD - the mean field stress τ_{mf} is the only direct (but very incomplete) information available about dislocation interaction. The next chapter will show how to complement the mean field stress with missing stress components.

11.2 Flow stress and back stress

As we saw, the mean field stress is not sufficient to obtain closure of the problem of dislocation dynamics. In the following we will introduce additional stresses that account for interaction phenomena which reside below the mean field resolution. For instance, 'dislocation jamming' has been recognised in the literature as being one of the key issues concerning stress fluctuations below the resolution of the mean field (e.g. Miguel *et al.*, 2002, 2008, 2001). The jamming behavior can be observed in dipole or multipole dislocation configurations (interaction through stress field) or junctions (core interaction). Zaiser *et al.* (2001) and Groma (1997); Groma *et al.* (2003) investigated these interaction effects numerically. For two dimensional systems of straight, parallel edge dislocations they could identify analytical approximations which make these interaction effects accessible for the framework of continuum dislocation models by means of so-called 'dislocation correlation functions'[1]. The key point is that all stress contributions which are not contained inside the mean field stress are extremely short-ranged (e.g. stresses arising from a dipole can be neglected after the distance of a few Burgers vectors). Then, in a continuous description with a resolution much coarser than the average dislocation spacing these interactions can be obtained as *lo-*

---

[1] First steps towards the generalisation to three dimensional systems were done in Zaiser & Hochrainer (2006) and Csikor *et al.* (2007)

cal quantities from dislocation density values and their respective gradients: Zaiser *et al.* (2001) and Groma *et al.* (2003) identified expressions for these missing terms, proportional to the square root of the total density and to the gradient of a 'signed density' (the 'geometrically necessary' density). They take the form

$$\tau_{\mathrm{y}} = aGb\sqrt{\rho_{\mathrm{t}}} \quad \text{and} \quad \tau_{\mathrm{b}} = \frac{DGb}{\rho_{\mathrm{t}}}\partial_x \rho_{\mathrm{G}} \tag{11.1}$$

where both $a \approx 0.3 \ldots 0.5$ and $D \approx 0.6 \ldots 1.0$ are constants which depend on the geometry of the glide system. τ_{y} is the 'friction stress' or flow stress which is phenomenologically described through the Taylor relationship, τ_{b} is a 'back stress' which governs the stress due to piling up of dislocations of the same sign e.g. against an impenetrable wall as in Fig. 11.1. The yield stress is the stress that has to be overcome in order to move a dislocation in the stress field of other dislocations, for instance when dislocations in dipole arrangements only move once a local stress greater than a dipole stress is reached.

If we go back to the simple pile-up example from the beginning of this chapter we now can 'patch up' the mean field stress with τ_{b}. In this example all dislocations are geometrically necessary. The resulting stress is shown in Fig. 11.4(a). The system now has non-zero stresses everywhere, very close to those of the averaged discrete stress values. Similarly, we obtain the flow stress from the average dislocation density as used for the system shown in Fig. 11.3(a) which amounts to a total dislocation density $\rho_{\mathrm{t}} = 8 \cdot 10^{-12} 1/\mathrm{m}^2$. With a factor $a = 0.4$ this system results in an equivalent flow stress of $\tau_{\mathrm{y}} = 21.83$GPa, which is exactly in the range of the maximum peak value of the stress along a (dislocation free) path

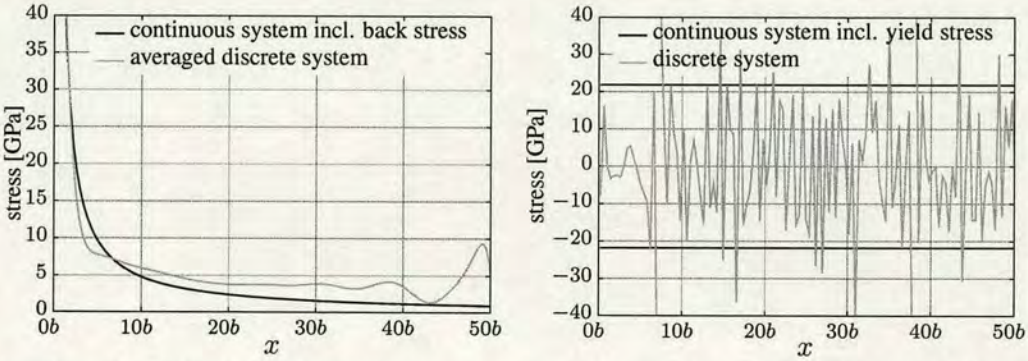

(a) dislocation pile up: stresses with back stress ($D = 0.6$)

(b) statistically homogeneously distributed edge dislocations: yield stress ($a = 0.4$) denoted by the two lines

Figure 11.4: *Mean field stresses with the additional local stress components τ_{y} and τ_{b} in comparison with the discrete system*

through the edge distribution.

11.3 Line tension

Throughout this thesis we do not consider a line tension. Nonetheless, it can be done in a straightforward manner. The line tension accounts for the fact that line segments of a dislocation loop interact with each other. It acts such as to minimize the strain energy of the dislocation by straightening the line with the line tension force T. In a *constant line tension approximation* orientation effects are neglected. Energetic considerations yield the static equilibrium stress

$$\tau_{\mathrm{lt}} = Tk/b, \tag{11.2}$$

where $T \approx Gb^2 = \text{const}$ is the dislocation line tension, also called 'self-force'. For a curved line with curvature k this stress is necessary to maintain its curved state.

It needs to be noted that the concept of the line tension is intuitive and simple in the discrete case. Contrary, in the continuous case again fluctuations of line curvature below the resolution of the governing kinematic fields cannot be accounted for. Those arise for instance from dislocations which bow out between junctions and other obstacles with a spacing smaller than the resolution of the density field. In a continuum description those effects are also considered in the flow stress approximation.

11.4 Equation of motion

In general we obtain the velocity field from the sum of all stresses, τ, under the assumption of a linear-viscous model of over damped dislocation motion by assuming

$$v = \begin{cases} \frac{b}{B}(\tau - \tau_{\mathrm{y}}) & \text{if } \tau > +\tau_{\mathrm{y}}, \\ \frac{b}{B}(\tau + \tau_{\mathrm{y}}) & \text{if } \tau < -\tau_{\mathrm{y}}, \ , \\ 0 & \text{otherwise.} \end{cases} \tag{11.3}$$

with $\tau = \tau_{\mathrm{mf}} - \tau_{\mathrm{b}} - \tau_{\mathrm{lt}}$, where τ_{mf} contains both contributions from external applied loading/prescribed displacements and the inhomogeneous strain state. τ_{b} is the back stress and τ_{lt} denotes the stresses from self interaction. The latter two stresses are conservative in nature and may recover upon unloading, while the yield stress as a 'friction stress' is dissipative in nature. B denotes the drag-coefficient for dislocations.

Now, our dislocation dynamics framework is dynamically closed and we can summarize all necessary solution steps in Fig. 11.5, where we assumed that the elastic problem is solved by means of a finite element method as outlined before.

```
1.   Initialize the system at $t = t_0$
1.1  for kinematics                              $\rho^i = \rho^0,\ k^i = k^0,\ \gamma^i = \gamma^0$
                                                 set velocity $v$ according to stresses
1.2  for dynamics                                prescribed external loading $\boldsymbol{f}^i$
                                                 prescribed external displacement $\boldsymbol{d}^i$

2.   Evolve dislocation micro-structure
2.1  compute evolution of micro-structure $\partial_t \rho,\ \partial_t k$ and $\partial_t \gamma$
2.2  time integration
     $\rho^{i+1} = \rho^i + \int_{t^i}^{t^{i+1}} \partial_t \rho \,\mathrm{d}t, \quad k^{i+1} = k^i + \int_{t^i}^{t^{i+1}} \partial_t k \,\mathrm{d}t, \quad \gamma^{i+1} = \gamma^i + \int_{t^i}^{t^{i+1}} \partial_t \gamma \,\mathrm{d}t$

3.   Transfer information from slip plane to body
3.1  plastic distorsion                          $\boldsymbol{\beta}^{\mathrm{pl}} = \sum_{\mathsf{s}} \frac{\gamma_{\mathsf{s}}}{b_{\mathsf{s}}} \mathcal{M}_{\mathsf{s}}$
3.2  plastic strains (small strain context)      $\boldsymbol{\varepsilon}^{\mathrm{pl}} := \mathrm{Sym}\left(\boldsymbol{\beta}^{\mathrm{pl}}\right) = \frac{1}{2}\left(\beta^{\mathrm{pl}}_{ij} + \beta^{\mathrm{pl}}_{ji}\right)$

for each finite element:
    4.   Solution of the eigenstrain problem
    4.1  strains to be balanced                  $\boldsymbol{\varepsilon}_0 = -\boldsymbol{\varepsilon}^{\mathrm{pl}}$ where all $\varepsilon^{\mathrm{pl}}_{ii}$ vanish
    4.2  equivalent nodal forces                 $\boldsymbol{f}_0 = \mathbf{B} : \mathbb{C} : \boldsymbol{\varepsilon}_0$
    4.3  FE solution yields displacements $\boldsymbol{d}$
    4.4  Postprocessing of displacements yields stresses for compatible
         deformation state                       $\boldsymbol{\sigma}$

    5.   Correction of doubly considered elements
    5.1  nodal displacements of a free element   $\boldsymbol{d}_0 = \mathbf{K}_{\mathrm{el}}^{-1} : (-\mathbf{B} : \mathbb{C} : \boldsymbol{\varepsilon}_0)$
    5.2  stress correction                       $\Delta\boldsymbol{\sigma} = \mathbb{C} : \mathbf{B}\boldsymbol{d}_0$

6.   Resolved shear stress
     on s-th slip plane                          $\tau_{\mathrm{mf}} = \mathcal{M}_{\mathsf{s}}^{-1}\left(\boldsymbol{\sigma}^* - \Delta\boldsymbol{\sigma}\right)$

7.   Update velocity $v = f(\boldsymbol{\tau}, \ldots)$
     e.g. with $\tau = \tau_{\mathrm{mf}} - \tau_{\mathrm{b}} - \tau_{\mathrm{lt}}$        $v = \begin{cases} \frac{b}{B}(\tau - \tau_{\mathrm{y}}) & \text{if } \tau > +\tau_{\mathrm{y}}, \\ \frac{b}{B}(\tau + \tau_{\mathrm{y}}) & \text{if } \tau < -\tau_{\mathrm{y}}, \\ 0 & \text{otherwise.} \end{cases}$ ,

8.   New step: goto 2.
```

Figure 11.5: *Algorithmic overview. Quantities used in a standard finite element context are the finite element operator matrix* $\mathbf{B} = \mathbf{L} \cdot \mathbf{N}$ *(with* $\mathbf{L}$ *the operator matrix of spatial derivatives and* $\mathbf{N}$ *the matrix of shape functions) and element stiffness matrix* $\mathbf{K}_{el}$.

11.5 Applications

In the following we explore some numerical examples which make use of the flow stress and back stress. We show which form the back stress takes in the frame work of CDD.

Deformation of a constrained channel

Groma *et al.* (2003) investigated the deformation of a constrained channel deforming in simple shear (Fig. 11.6) by use of Eq. (11.1).

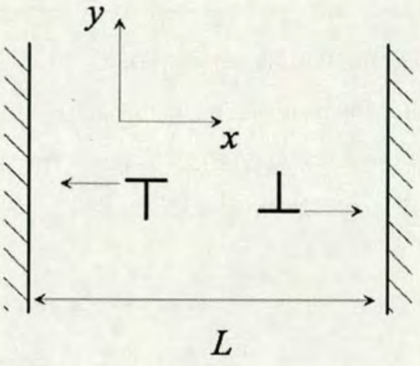

Figure 11.6: *Geometry of the constrained slip channel*

We tackle this simple system with CDD, where the configuration space essentially reduces to two points of different orientations: one for the orientation of positive and one for orientation of negative edges.

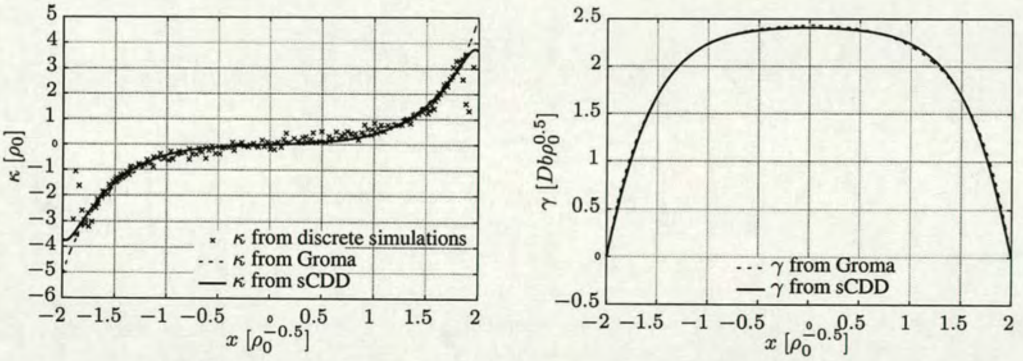

(a) GND density

(b) plastic strain

Figure 11.7: *Sign dislocation density and strain profile in comparison with data from Groma* et al. *(2003)*

The resulting density distribution and plastic strain profile, Fig. 11.7, are almost identical and they should be, since for this example the evolution equations in CDD simplify to those of Groma. We used a different kind of boundary conditions, namely the decaying velocity within a boundary layer as outlined before. This is responsible for the difference at the channel walls. Note that without a back stress the density layer at the walls would collapse into an infinite density peak of vanishing thickness directly at the wall. In this case, the mean field stress would be zero.

Back stress in the higher-order configuration space of CDD

For two dimensional dislocation systems one can try to generalise these expressions by accounting for different line orientations in one point. The back stress then also is not restricted to one direction only: the resulting back stress function becomes two dimensional and gets contributions from lines with (almost) all line directions.In the configuration space of CDD the back stress (Hochrainer, 2006) can be explicitly written as

$$\tau_{\mathrm{b}}(x,\varphi) = \frac{DGb}{\rho_{\mathrm{t}}} \nabla_{\nu} \left(e_x \alpha^x + e_y \alpha^y \right), \tag{11.4}$$

where we used the abbreviations

$$\alpha^x := \int_0^{2\pi} \rho \cos \tilde{\varphi} \, \mathrm{d}\varphi \quad \text{and} \quad \alpha^y := \int_0^{2\pi} \rho \sin \tilde{\varphi} \, \mathrm{d}\varphi. \tag{11.5}$$

It then follows

$$\begin{aligned} \tau_{\mathrm{b}}(x,\varphi) = {} & \frac{DGb}{\rho_{\mathrm{t}}} \sin\varphi \, \nabla_x \left(\cos\varphi \int_0^{2\pi} \rho \cos\tilde{\varphi} \, \mathrm{d}\tilde{\varphi} + \sin\varphi \int_0^{2\pi} \rho \sin\tilde{\varphi} \, \mathrm{d}\tilde{\varphi} \right) \\ & + \frac{DGb}{\rho_{\mathrm{t}}} \cos\varphi \, \nabla_y \left(\cos\varphi \int_0^{2\pi} \rho \cos\tilde{\varphi} \, \mathrm{d}\tilde{\varphi} + \sin\varphi \int_0^{2\pi} \rho \sin\tilde{\varphi} \, \mathrm{d}\tilde{\varphi} \right). \end{aligned} \tag{11.6}$$

Fig. 11.8 qualitatively shows the influence of the back stress for a one dimensional channel problem as outlined in Section 5.2, where we assumed a homogeneous loop distribution in y direction and impenetrable walls at $x = 0$ and $x = l_x$.

In Fig. 11.8(c) the blue area corresponds to the 'forward stress', which can be interpreted as the stress which is pressing the dislocation against the wall. The darker red areas are the back stress. The back stress is here only very small since most of the density is not yet in the influence area of the boundary.

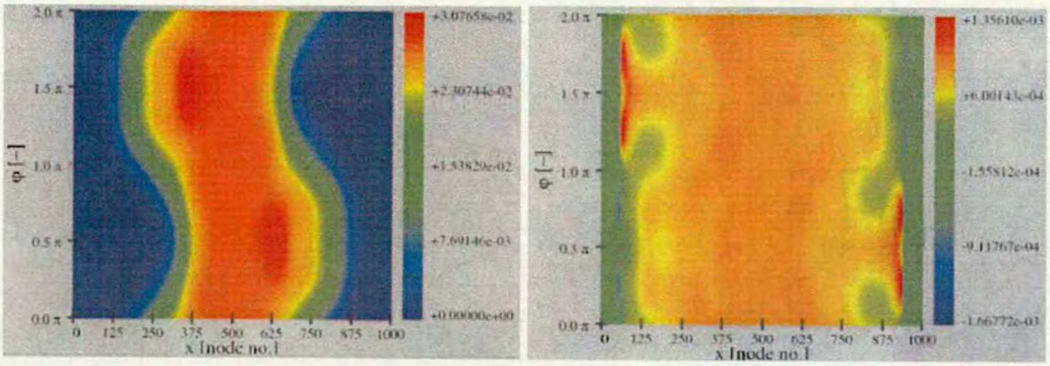

(a) density

(b) curvature

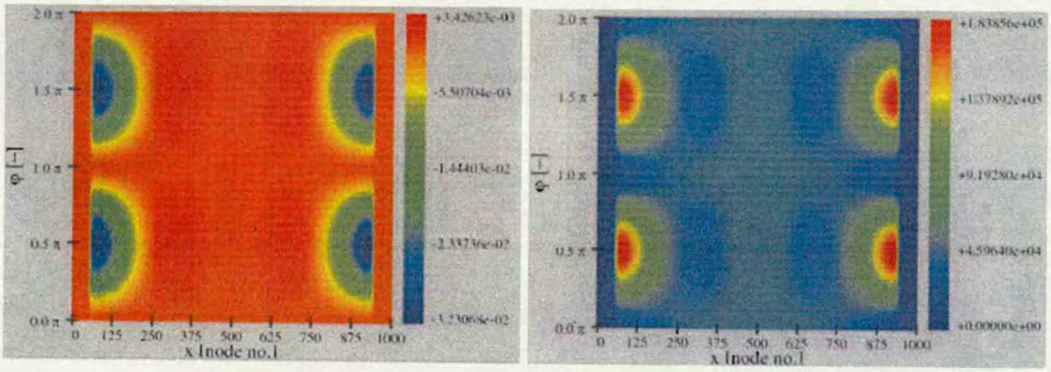

(c) back stress

(d) velocity

Figure 11.8: *Influence of back stress on a loop distribution in a slip channel*

Line tension formulation in a simple 1d system of CDD

Assuming a homogeneous system in y-direction the evolution equation for the curvature, Eq. (4.25), can be explicitly written as

$$\partial_t k_{(x\varphi)} = -vk^2 - \left(\cos^2\varphi\partial_{xx}v + 2k\cos\varphi\partial_{x\varphi}v + k^2\partial_{\varphi\varphi}v\right) + \dots \\ \dots + \sin\varphi\left(k\partial_x v - v\partial_x k\right) - \cos\varphi\left(\partial_x k\partial_\varphi v - \partial_x v\partial_\varphi k\right). \tag{11.7}$$

Assuming only a constant resolved shear stress τ, open boundary conditions, and a line tension as outlined in Eq. (11.2) the equation of motion takes the simple form

$$v_{(r,\varphi)} = B^{-1}(\tau_{(r)}b - Tk_{(r,\varphi)}), \tag{11.8}$$

Note, that v also may have a dependency on the line orientation due to the definition of the curvature. For brevity we will abbreviate the first term as $v_0 := B^{-1}\tau b$. With this Eq. (11.7) becomes

$$\partial_t k_{(x,\varphi)} = -\left(v_0 - \frac{Tk}{B}\right) k^2 - v_0 \sin\varphi \partial_x k + \frac{T}{B}\left(\cos^2\varphi \partial_{xx} v + 2k\cos\varphi \partial_{x\varphi} v + k^2 \partial_{\varphi\varphi} v\right) \tag{11.9}$$

The first term is a production term for curvature, reduced by the line tension influence. The second term - which also could be written as $\mathrm{div}(k\boldsymbol{v})$ - can be interpreted as a transport term for curvature in spatial direction.

Micro-bending without and with back stress

In the case of simple geometrical relations the mean field stress can be analytically determined - as we did in Section 6. The left column of Fig. 11.9 shows three snapshots in time of the stress components for a bending system ($h = 2\mu\mathrm{m}$ and $M = 180000\mathrm{GPa\,m}^2$) without back stress.

τ^{res} denotes the resulting stress (the sum of all contributions of the equation of motion). The elastic zone is defined by the yield stress $\pm\tau_{\mathrm{y}}$. The density dependency of τ_{y} shows in the 'dip' around $x = 0$.

To make the previous system more realistic we now also consider a back stress ($D = 1.0$) while retaining open boundary conditions as we did before. The right column in Fig. 11.9 shows three snapshots in time of the stress components for a bending system in the aforementioned section. We observe that for the system with back stress no elastic core persists anymore (e.g. Fig. 11.9(f)) which is due to the back stress. The reason becomes clearer in Fig. 11.10, when we take a look at the GND density, Fig. 11.10(b). Dislocation must have entered the elastic core causing a non-zero density in the center region of the film. Without back stress the yield stress level could not be overcome in this region. With back stress, however, this level can be reached due to dislocations piling up against the boundary of the elastic core and eventually dislocations are forced into the (previously) elastic core.

Since in this chapter we only wanted to introduce and demonstrate the influence of stresses and their specific treatment within CDD we will not further analyse the behavior of for instance the bending system with back stress in terms of a size effect.

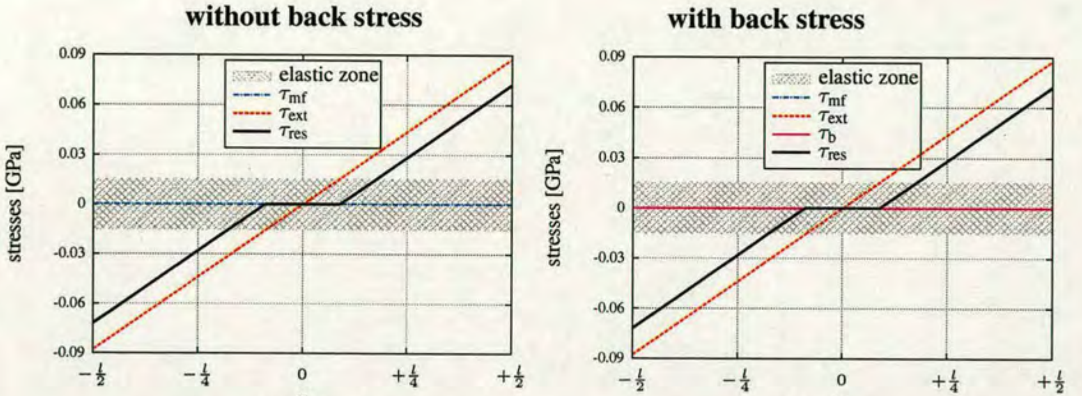

(a) initial state $t = 0$ $(D = 0.0)$

(b) initial state $t = 0$ $(D = 1.0)$

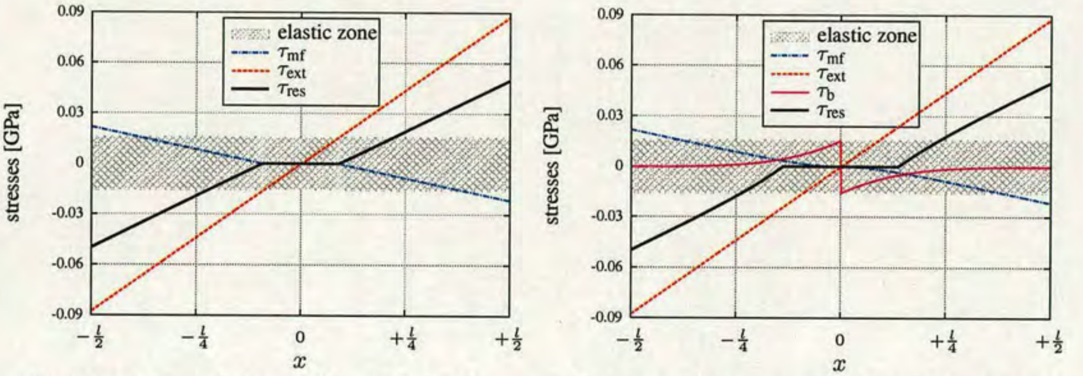

(c) intermediate state $t = 0.001\mu s$ $(D = 0.0)$

(d) intermediate state $t = 0.001\mu s$ $(D = 1.0)$

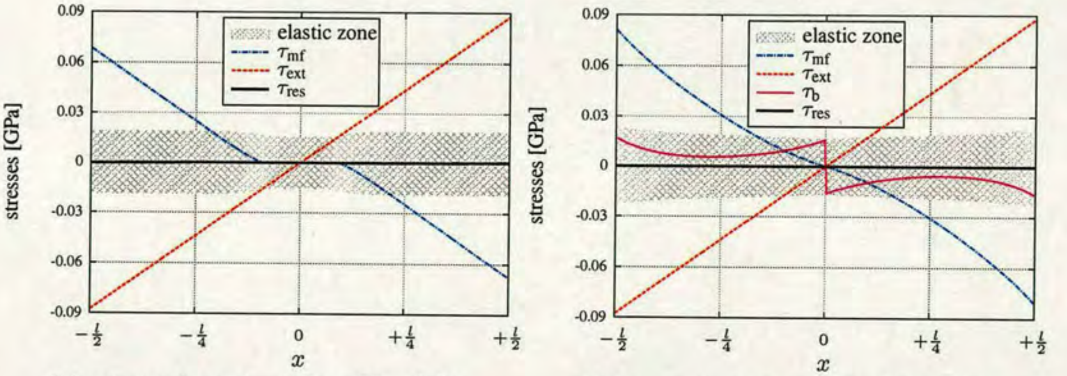

(e) converged state $t = 0.1\mu s$ $(D = 0.0)$

(f) converged state $t = 0.1\mu s$ $(D = 1.0)$

Figure 11.9: *Temporal evolution of stress profiles for a bending system without and with back stress (left and right column).*

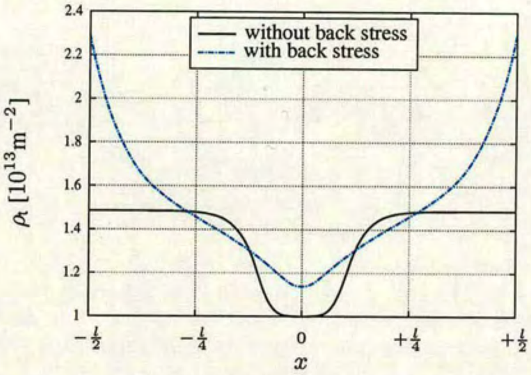

(a) total density ρ_t

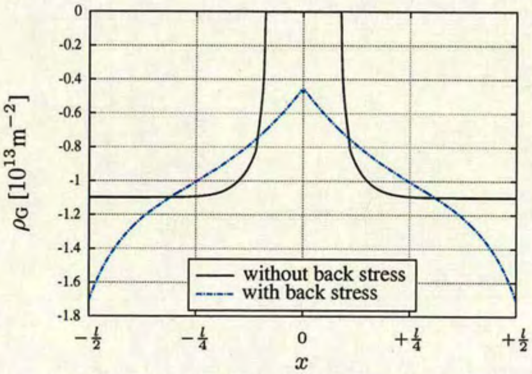

(b) GND density

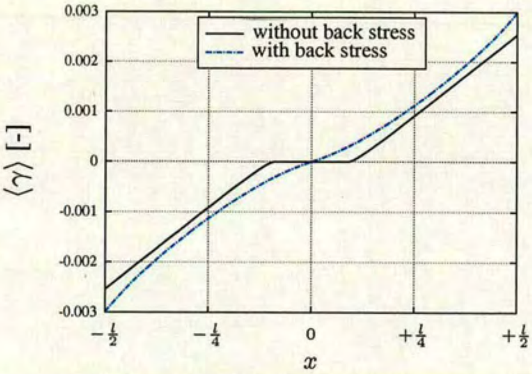

(c) accumulated plastic strain

Figure 11.10: *Comparison of density and plastic strain values for a bending system with and without back stress*

Part V

Summary and Outlook

We demonstrated that CDD as a generalisation of the classical Kröner theory can capture several fundamental phenomena of the evolution of systems of curved dislocations which cannot be recovered from other dislocation based continuum theories. In particular, the simple benchmark problem of an ensemble of expanding loops showed that the averaging process underlying CDD conserves important kinematic properties of dislocation loops. Studying the expansion of a single quasi-discrete loop served to elucidate certain numerical problems arising from the discretisation of orientation space and to find appropriate remedies.

An important problem in generalised continuum theories (e.g. gradient plasticity theories) concerns the definitions of boundary conditions. CDD allows to relate boundary conditions to the physical properties of dislocation motion at surfaces and interfaces. For instance, the problem of a plastically non-deformable boundary corresponds to zero dislocation velocity and thus zero dislocation flux. This is one of the big advantages of CDD by comparison with gradient plasticity models, where boundary conditions cannot easily be based on the physics of the problem under consideration. Nonetheless, boundary conditions do pose a numerical challenge since the accumulation of density of only one orientation (i.e. line segments parallel to an impenetrable wall) leads to steep gradients. Further work concerning the numerical method on a non-uniform grid has to be done in the future. A finite element method, in particular a discontinuous Galerkin method might help to ensure non-flux conditions at the boundary while conserving density where it is being convected.

We showed that the evolution of dislocation densities in orientation space may be a key factor in the description of inhomogeneous deformation processes, as changes in dislocation orientation may be an important mechanism for providing the 'geometrically necessary' dislocations needed to accommodate strain gradients. Accordingly, simulations of microbending using a simple Taylor-based flow rule yielded results that differ substantially from the predictions of gradient plasticity theories that assume strain gradients to be accommodated exclusively by the introduction of additional excess dislocations.

We explored a new branch of CDD, which can be obtained by making simplifying assumptions about the velocity and curvature of dislocations in one point. We derived the governing equations of sCDD in a notation which is consistent with that of CDD and proved that a special case of sCDD is identical with Sedláček's continuum theory. Several benchmark problems were simulated and compared to results obtained from CDD. We found in almost all cases excellent agreement between the two theories. Therefore, future work concerning the simulation of large systems will heavily make use of this simplified theory since the reduced dimensionality saves a lot computational resources.

In the last part we tackled the problem of stresses, which is necessary for the closure of the dynamics. A numerical method based on the eigenstrain concept was proposed which is suitable for the continuum settings of CDD and sCDD and can be applied to arbitrary system geometries and general boundary conditions. Based upon this method we demonstrated the necessity to introduce 'back stress' and 'flow stress' terms into the dynamics framework and subsequently studied various systems numerically. Since the main emphasis of this thesis is on the kinematics of CDD (and its simplified form) those examples were only very simple and at times comprised of special cases where the stresses even could be obtained analytically. Hence, a next step towards more realistic systems will be the embedding of the dislocation kinematics into a crystal plasticity context.

An important tool for further development of the theory will be comparative simulation work with discrete dislocation dynamics simulations (DDD) and CDD or sCDD calculations performed in parallel on systems of similar geometry. This is essential for obtaining initial data (dislocation micro-structure), judging their statistical content and for gauging further developments of CDD and its numerical implementation. For instance, up to now sources and their activation have not been treated, as well as dislocation annihilation and various other reactions. This requires a deeper understanding of the underlying statistics together with a robust implementation.

In one of Kröner's last publications, 'Benefits and shortcomings of the continuous theory of dislocations' (Kröner, 2001) he finished with the open question

> *The greatest shortcoming is that the dislocation density tensor* α, *[...] measures the* average *dislocation density only and therefore, regards the internal mechanical state utmost incomplete. In principle, this shortcoming could be overcome by reorientation of dislocation theory towards a statistical theory, but only with highest expenditure of computation. Is it worthwhile to try that?*

Today, the answer to this question is clear for us: yes, it is worthwhile; all foundations are already there.

Part VI

Appendix

Appendix A

CDD's directional derivatives $\nabla_{\boldsymbol{L}}$, $\nabla^2_{\boldsymbol{L}}$, and $\nabla_{\boldsymbol{V}}$

Tangents and velocities As already introduced in Section 4.3 we use the following convention for the spatial line direction and velocity

$$\boldsymbol{l} = \cos\varphi \boldsymbol{e}_x + \sin\varphi \boldsymbol{e}_y \tag{A.1}$$

$$\boldsymbol{v} = v\sin\varphi \boldsymbol{e}_x - v\cos\varphi \boldsymbol{e}_y \tag{A.2}$$

$\boldsymbol{L}$ and $\boldsymbol{V}$ denote the "generalized line direction" and "generalized velocity". As introduced in Chapter 4 they consist of the components (cf. Eq. (4.8))

$$\boldsymbol{L}_{(\mathrm{r},\varphi)} = \left(\cos\varphi, \sin\varphi, k_{(\boldsymbol{r},\varphi)}\right) = \left(\boldsymbol{l}, k_{(\mathrm{r},\varphi)}\right) \tag{A.3}$$

$$\boldsymbol{V}_{(\mathrm{r},\varphi)} = \left(v\sin\varphi, -v\cos\varphi, \vartheta\right) = \left(\boldsymbol{v}, \vartheta\right), \tag{A.4}$$

where $\vartheta = -\nabla_{\boldsymbol{L}} v$ is the rotational velocity.

Directional derivatives along $\boldsymbol{L}$ and $\boldsymbol{V}$ take the following form

$$\nabla_{\boldsymbol{L}}(\cdot) = \left[\boldsymbol{l}_{(\varphi)} \;\; k_{(\mathrm{r},\varphi)}\right] \cdot \begin{bmatrix} \nabla_{\boldsymbol{r}}(\cdot) \\ \nabla_{\varphi}(\cdot) \end{bmatrix} = \cos\varphi\partial_x(\cdot) \; + \; \sin\varphi\partial_y(\cdot) \; + \; k_{(\mathrm{r},\varphi)}\partial_\varphi(\cdot). \tag{A.5}$$

and

$$\nabla_{\boldsymbol{V}}(\cdot) = \left[\boldsymbol{v}_{(\mathrm{r},\varphi)} \;\; \vartheta_{(\mathrm{r},\varphi)}\right] \cdot \begin{bmatrix} \nabla_{\boldsymbol{r}}(\cdot) \\ \nabla_{\varphi}(\cdot) \end{bmatrix} = v\sin\varphi\partial_x(\cdot) \; - \; v\cos\varphi\partial_y(\cdot) \; + \; \vartheta_{(\mathrm{r},\varphi)}\partial_\varphi(\cdot). \tag{A.6}$$

CDD's gradients Of particular interest in CDD are the directional derivatives $\nabla_{\boldsymbol{L}} v$, $\nabla^2_{\boldsymbol{L}} v$ and $\nabla_{\boldsymbol{V}} k$, since they occur in the evolution equations for scalar density and mean curvature.

Explicitely writing down all components gives

$$\nabla_{\boldsymbol{L}}(v)_{(r,\varphi)} = \cos\varphi\partial_x v_{(r,\varphi)} \,+\, \sin\varphi\partial_y v_{(r,\varphi)} \,+\, k_{(r,\varphi)}\partial_\varphi v_{(r,\varphi)} = -\vartheta_{(r,\varphi)} \tag{A.7}$$

$$\nabla_{\boldsymbol{V}}(k)_{(r,\varphi)} = v\sin\varphi\partial_x(k_{(r,\varphi)}) \,-\, v\cos\varphi\partial_y(k_{(r,\varphi)}) \,+\, \vartheta_{(r,\varphi)}\partial_\varphi(k_{(r,\varphi)}), \tag{A.8}$$

Note that gradient operator as well as its argument are both evaluated at the same point $(\boldsymbol{r},\varphi)$ in the configuration space. Thus, for brevity we only write the point of evaluation once. The same also holds for the twofold gradient $\nabla^2_{\boldsymbol{L}}(v)$:

$$\begin{aligned}
\nabla^2_{\boldsymbol{L}}(v) \;&=\; \cos\varphi\;\partial_x(\cos\varphi\partial_x v + \sin\varphi\partial_y v + k\partial_\varphi v)\\
&+\; \sin\varphi\;\partial_x(\cos\varphi\partial_x v + \sin\varphi\partial_y v + k\partial_\varphi v)\\
&+\; k\;\partial_\varphi(\cos\varphi\partial_x v + \sin\varphi\partial_y v + k\partial_\varphi v)
\end{aligned} \tag{A.9}$$

$$\begin{aligned}
&=\; \cos^2\varphi\partial_x\partial_x v + \cos\varphi\sin\varphi\partial_x\partial_y v + \cos\varphi\big((\partial_x k)(\partial_\varphi v) + k\partial_x\partial_\varphi v\big)\\
&+\; \sin\varphi\partial_y\cos\varphi\partial_x v + \sin^2\varphi\partial_y\partial_y v + \sin\varphi\big((\partial_y k)(\partial_\varphi v) + k\partial_y\partial_\varphi v\big)\\
&+\; k\big(-\sin\varphi\partial_x v + \cos\varphi\partial_\varphi\partial_x v\big)\\
&+\; k\big(+\cos\varphi\partial_y v + \sin\varphi\partial_\varphi\partial_y v\big)\\
&+\; k\big((\partial_\varphi k)(\partial_\varphi v) + k\partial_\varphi\partial_\varphi v\big)
\end{aligned} \tag{A.10}$$

$$\begin{aligned}
&=\; \cos^2\varphi\partial_x\partial_x v + \sin^2\varphi\partial_y\partial_y v + k^2\partial_\varphi\partial_\varphi v\\
&+\; 2\sin\varphi\cos\varphi\partial_x\partial_y v + 2k\cos\varphi\partial_x\partial_\varphi v + 2k\sin\varphi\partial_y\partial_\varphi v\\
&-\; k\big(\sin\varphi\partial_x v - \cos\varphi\partial_y v\big)\\
&+\; \underbrace{\big(\cos\varphi\partial_x k + \sin\varphi\partial_y k + k\partial_\varphi k\big)}_{\nabla_{\boldsymbol{L}}(k)}\partial_\varphi v
\end{aligned} \tag{A.11}$$

Appendix B
Eigenstrain solution for a single edge dislocation

As demonstration of the procedure for obtaining the mean stress field proposed in Section 10 we compute the stress field of an edge dislocation. A single edge dislocation brought into a volume represents a distorted state, which can be obtained by loading the system by prescribed eigenstrains ε^* for all elements' Gauss points at $y = l_y/2$ and $x = l_x/2 \ldots l_x$ (Fig. B.1). The elastic body in this figure was discretised by 100 elements in each direction, the total dimensions are $l_x = l_y = 10$, further material parameters are $E = 1.0$, $\nu = 0.3$, $b_x = 0.05$. The difference in horizontal displacements u_x on the right face of Fig. B.1(b) is exactly the modulus of the Burgers vector. No displacement boundary conditions are necessary, since there are no external applied forces to be balanced; all stresses and nodal displacements are caused by the eigenstrain $\varepsilon^* = b/h_y$, where h_y is the height of one finite element. The plots of the normal stresses in Fig. B.2 and B.3 are in very good agreement with the analytical solution (e.g. Hirth & Lothe, 1982)

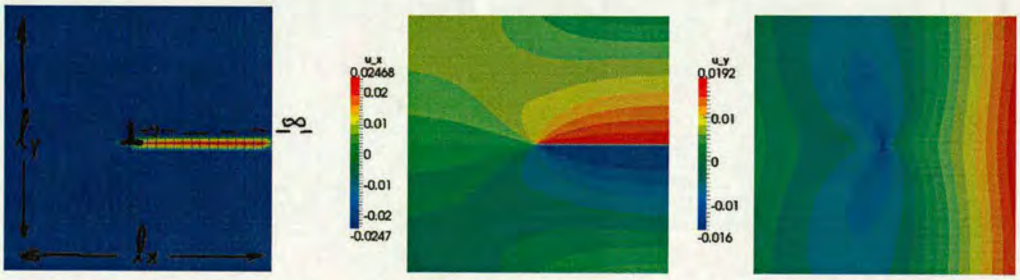

(a) prescribed strain ε^* (red=ε^*, blue=no eigenstrain) (b) horizontal displacement u_x (c) vertical displacement u_y

Figure B.1: *Dislocation brought into the center of the body causes an eigenstrain ε^* for each element on the dislocations' path (a). After solution of the elastic problem we obtain the displacements (b) and (c).*

$$\sigma_{xx} = -\frac{Gb}{2\pi(1-\nu)} \frac{y(3x^2+y^2)}{(x^2+y^2)^2} \tag{B.1}$$

$$\sigma_{yy} = +\frac{Gb}{2\pi(1-\nu)} \frac{y(x^2-y^2)}{(x^2+y^2)^2}. \tag{B.2}$$

Responsible for the growing deviations towards the boundary are boundary effects: the analytical solution is valid only for an infinite elastic domain. The boundedness of the volume causes surface stresses, which are not considered in the analytical solution but are already included in our solution. Thus, it is not necessary to include them through 'image forces' as e.g. necessary in the 'standard procedure' described in Section 10.1.

Fig. B.4 shows the shear stress, therein Fig. B.4(a) shows the stresses without adding the correction (i.e. after step ③ in Fig. 10.1), Fig. B.4(a) shows the stress after adding the correction (i.e. after step ④ in Fig. 10.1). The numerically obtained stresses match the analytical solution

$$\sigma_{xy} = +\frac{Gb}{2\pi(1-\nu)}\frac{x(x^2-y^2)}{(x^2+y^2)^2} \tag{B.3}$$

very well.

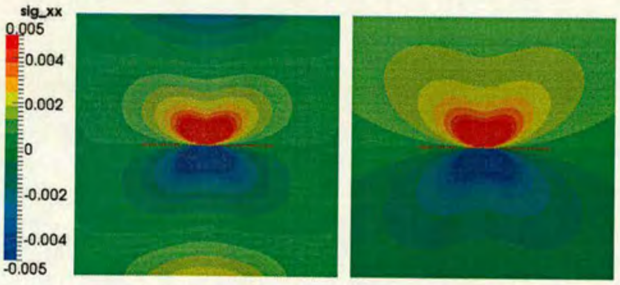

(a) numerical (b) analytical

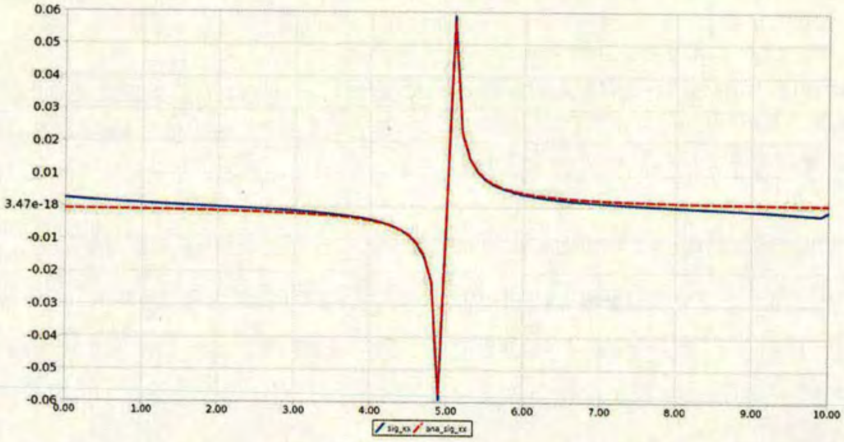

(c) Line plot along the vertical line at $x = l_x/2$. The dashed line shows the analytical solution.

Figure B.2: *Normal stress σ_{xx} obtained from out method in comparison with the analytical solution*

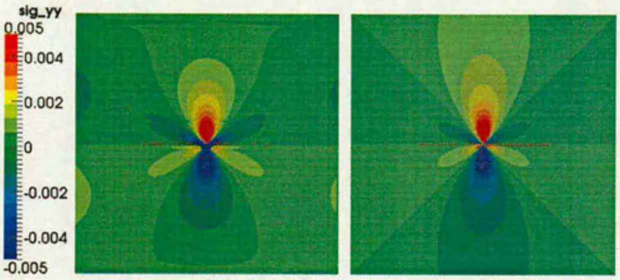

(a) numerical

(b) analytical (for infinite volume))

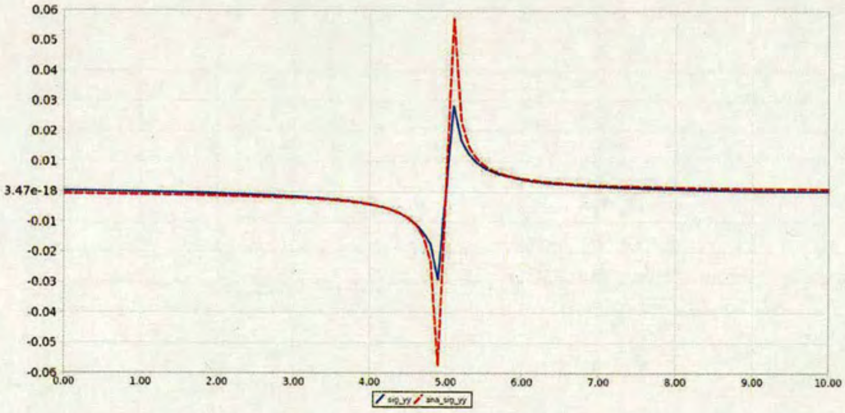

(c) Line plot along the horizontal line at $y = l_y/2$. The dashed line shows the analytical solution.

Figure B.3: *Normal stress σ_{yy} obtained from out method in comparison with the analytical solution*

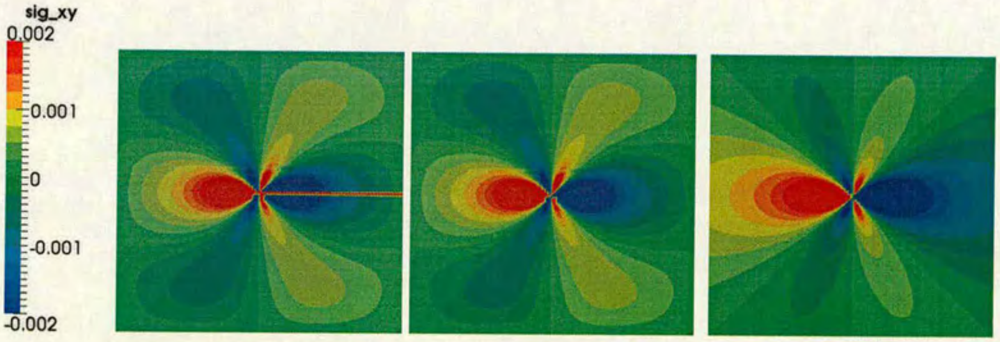

(a) σ_{xy} - numerical

(b) σ_{xy} - numerical with post processing of stresses

(c) σ_{xy} - analytical

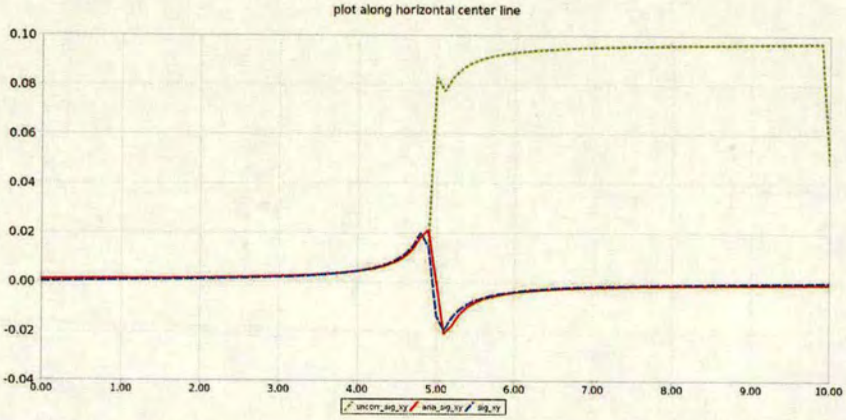

(d) Line plot along the horizontal line at $y = l_y/2$. The dotted line corresponds to (a), the dashed line to (b) and the continuous line shows the analytical solution as in (c)

Figure B.4: *Shear stress σ_{xy} for System A. Without taking into account that plastic slip does not cause any stresses we obtain the picture at the top left. The top middle picture shows the numerical solution with 'post processing' of the stresses, the top right picture shows the analytical solution without taking boundaries into account.*

Appendix C
Comments on the simulation program

For our simulation we chose the use of C++[1]. Especially the object oriented features of this language are very attractive if one wants to reuse parts of the code. Among others, inheritance offers the possibility to use slightly different implementations for different problems (e.g. bending and slip channel), while the core of the simulation code stays the same. There is some overhead and the architecture of the program has to be planned more in advance and more strictly than in typical structured programming languages but we found that it was well worth it.

The code was parallelised using openMP throughout, although cutting edge performance was not our aim. Optimisation of the program structure for use of openMP was e.g. done by using a `SlipPlane` object as container for all field variables such that iteration over them can be done simultaneously.

In the following we briefly list some of the used features which can be seen in the main program:

- `bending1D::SystemParameter spara(argc,argv);`
  `bending1D` is a namespace which unifies all routines for 1D bending (homogeneous in y direction). `bending1D::SystemParameter spara(argc,argv)` is derived from `SystemParameter spara(argc,argv)` and contains e.g. additional information concerning the orientation of slip planes, bending moment etc.
- `Grid1D` is a specialisation of the base class `Grid2d`, which defines the discretisation. Therefore, in all places where a `Grid2D` object is expected we can just as well pass a `Grid1d` object, automatically implying that the y direction is homogeneous.
- `SlipPlane` is an abstract base class and contains the density, curvature, velocity and plastic stran fields along with the respective functionality. Some of `SlipPlane`'s

---

[1] More information on C++ for scientific programmic can be found in various text books, e.g. in Yang (2001).

methods are virtual and will be implemented in the derived classes `SlipPlane1d`, `SlipPlane2d`, `SlipPlane1dsimpl` etc. This allows for easy extension while prescribing the structure of the classes. `SlipPlane` instances instead of separate grid, density, curvature and strain objects can easily be passed to other objects.

- All information and functionality concerning boundary conditions is contained in the `BoundaryConditions` class, which e.g. offers functionality for efficient extrapolation of 'ghost node values'. Furthermore, this class is closely related to `SlipPlane`'s velocity member since e.g. impenetrable boundaries are implemented using a smooth function which decays to zero.

- Completely separated from these classes are the output routines. Postprocessing can be quite time consuming and thus we provide with the `OutputManager` and the `xxxSelection` classes a framework for organising and processing the output.

- The `EvoEqnSolver` does the actual time integration of the evolution equations. By using smart pointers we can 'inject' various post- and pre-processors which can be defined 'on the fly' and only need to be derived from an abstract base class in order to ensure a certain form which can be used from the solver.

```
// ----------------------------------------------------------------------
// ------- SYSTEM'S GEOMETRY --------------------------------------------
// ----------------------------------------------------------------------
const int fn_x   = 1001;      // number of nodes in x direction
const int fn_phi = 100;       // number of nodes in phi direction
const int gn     = 2;         // number of ghostnodes
// ----------------------------------------------------------------------


// ----------------------------------------------------------------------
// ------- INITIAL VALUES and other -------------------------------------
// ----------------------------------------------------------------------
bending1D::SystemParameter spara(argc,argv);

spara.theta  = M_PI/6.;        // angle slip plane and vert. axis
spara.h      = 3.0e3;          // film height in nm
                               // inclined length of slip plane

spara.k0 = 0.;                 // initial loop curvature, [k0]=1/nm
spara.M  = 5e5;                // bending moment in GPa m^2

BC_TYPE::val_t bc_type = BC_TYPE::open;  // boundary condition type

const double deltaX   = spara.l/(fn_x-1.);
const double deltaPHI = 2.*M_PI/double(fn_phi);
Grid1D grid(fn_x, fn_phi, gn, deltaX);

spara.rho_max = 1.e13;          // initial scalar density in 1/(m^2)
```

```
// - - - - - - - - - - - - - - - - - - - - - - - - - - - - - - - - - - -

spara.t_begin = 0.0;              // start time
spara.t_end   = 0.02;             // total time in mu s
spara.dt      = 1.e-6;            // initial step size
spara.dt_min  = 1.e-12;           // min. step size

NumericalDetails num;
num.atol = 1.0e-11;              // absolute tolerance
num.rtol = num.atol;             // rel. tol.

INIVALS::val_t rho_shape = INIVALS::constant;

const string base_dir = "bending_data";
const string work_dir = "tmp";
// ---------------------------------------------------------------------


// ---------------------------------------------------------------------
// ------- MATERIAL PARAMETER ------------------------------------------
// ---------------------------------------------------------------------
MaterialParameter mpara;
mpara.bx      = 0.256;           // Burgers vector in nm
mpara.B       = 5.e-8;           // Drag coefficient in GPa mu_s
mpara.E       = 128.4;           // Young's Modulus E in GPa
mpara.nu      = 0.33;            // Poisson's Ratio nu
mpara.alpha   = 0.4;             // factor for yield stress
mpara.T       = 0.0;             // line tension
mpara.D       = 0.0;             // backstress coefficient
mpara.G       = mpara.get_shear_modulus_from_E_and_nu();
// ---------------------------------------------------------------------


try {
        // -------------------------------------------------------------
        // ------- SlipPlane -------------------------------------------
        // -------------------------------------------------------------
        SlipPlane1D sp(grid,mpara);
        sp.initCurvature_const( spara.k0 );
        sp.initDensity        ( rho_shape );
        // -------------------------------------------------------------


        // -------------------------------------------------------------
        // ------- Boundary Conditions ---------------------------------
        // -------------------------------------------------------------
        BoundaryConditions bc( grid );

        bc.set_x_start_and_end_open();
        bc.set_y_direction_periodic();

        bc.apply_BCs_to_GhostNodes( sp );
        // -------------------------------------------------------------


        // -------------------------------------------------------------
        // ------- Evolution Equations ---------------------------------
        // -------------------------------------------------------------
        EvolutionEquations1D derivs( sp, bc );
```

```
// ------------------------------------------------------------


// ------------------------------------------------------------
// ------- Stress State of the Slip Plane ---------------------
// ------------------------------------------------------------
BackStress1D bckst( grid, mpara );

LineTension lt( mpara );

bending1D::StressState1D stressState ( grid, spara, bckst,lt);
stressState.update_stress_components( sp );
// ------------------------------------------------------------


// ------------------------------------------------------------
// ------- Setup Paths and Directory Tree ---------------------
// ------------------------------------------------------------
PathNames paths;
paths.set_base_dir( base_dir );
paths.set_work_dir( work_dir );

FileNames files;
// ------------------------------------------------------------


// ------------------------------------------------------------
// ------- Define Outputs and Output Manager ------------------
// ------------------------------------------------------------
SDplotSelection SDplot_list( grid );
GPlotSelection  GPlot_list ( grid );
SCubeSelection  SCube_list ( grid );

const int cutnodeX=0, cutnodeY=0, cutnodePHI=int(3./4.*fn_phi);
GPlot_list.set_all_cutnodes( cutnodeX, cutnodeY, cutnodePHI );
const int n_gplots=10,  n_sdplots=n_gplots,  n_scubes=n_gplots;

GPlot_list.enable_all_output();
SCube_list.enable_all_output();
SDplot_list.enable_only_main_output();

paths.setup_directory_structure( SDplot_list);

bending1D::OutputManager out( n_gplots, n_sdplots, n_scubes,
                              SDplot_list, GPlot_list, SCube_list,
                              paths, files,
                              spara, num );
// ------------------------------------------------------------


// ------------------------------------------------------------
// ------- Time Integration -----------------------------------
// ------------------------------------------------------------
EvoEqnSolver1D solver( sp, spara, num, out );

// solver.force_output_every_n_steps ( 1000 );
// solver.disable_adaptive_stepsize();

// inject post processor
```

```
        PostProc_ptr postp_ptr( new Proc_ensureSolenoidality() );
        solver.add_post_processor( postp_ptr );

        solver.integrate( derivs, stressState );
        // ------------------------------------------------------------
}
catch(string e)
        { cerr << "Caught␣an␣exception␣:␣" << string(e) << endl; }
catch(out_of_range e)
        { cerr << "Caught␣an␣out_of_range␣exception:␣" << e.what() << endl;
}
catch(runtime_error e)
        { cerr << "Caught␣an␣runtime_error␣exception:␣" << e.what() << endl;
}
catch(...)
        { cerr << "Caught␣an␣unknown␣exception.␣" << endl; }
}
```

References

ACHARYA, A., ROY, ANISH, & SAWANT, A. 2005. Continuum theory and methods for coarse-grained, mesoscopic plasticity. *Scripta Mater.*, **54**, 705–710.

ACHARYA, AMIT. 2001. A model of crystal plasticity based on the theory of continuously distributed dislocations. *J. Mech. and Phys. Solids*, **49**(4), 761–784.

ACHARYA, AMIT. 2003. Driving Forces and Boundary Conditions in Continuum Dislocation Mechanics. *Proc. R. Soc. A*, **459**(2034), 1343–1363.

ARSENLIS, A., CAI, W., TANG, M., RHEE, M., OPPELSTRUP, T., HOMMES, G., PIERCE, T. G., & BULATOV, V. V. 2007. Enabling strain hardening simulations with dislocation dynamics. *Model. Simul. Mater. Sci. Eng.*, **15**, 553–595.

ARZT, E. 1998. Size effects in materials due to microstructural and dimensional constraints: a comparative review. *Acta Mater.*, **46**(16), 5611 – 5626.

ASHBY, M.F. 1970. The Deformation of Plastically Non-homogeneous Materials. *Phil. Mag.*, **21**, 399–424.

BATHE, K.-J. 2001. *Finite-Elemente-Methoden.* 2 edn. Springer, Berlin.

BILBY, B. A., BULLOUGH, R., & SMITH, E. 1955. Continuous Distributions of Dislocations: A New Application of the Methods of Non-Riemannian Geometry. *Proc. Roy. Soc. London Ser. A*, **231**, 263–273.

BULATOV, V. V., & CAI, W. 2006. *Computer Simulations of Dislocations.* Oxford University Press.

BULATOV, V. V., & W., CAI. 2002. Nodal Effects in Dislocation Mobility. *Phys. Rev. Lett.*, **89**(11), 115501 1–4.

CLEVERINGA, H.H.M., VAN DER GIESSEN, E., & NEEDLEMAN, A. 1999. A discrete dislocation analysis of bending. *Int. J. Plast.*, **15**, 837–868.

COTTRELL, A.H. 1961. *Dislocations and plastic flow in crystals.* Oxford University Press, Amen House, London E.C.4.

CSIKOR, F. F., GROMA, I., HOCHRAINER, T., WEYGAND, D., & ZAISER, M. 2007. On the range of 3D dislocation pair correlations. *Pages 271–276 of:* JEULIN, DOMINIQUE, & FOREST, SAMUEL (eds), *Proceedings of the 11th International Symposium on Continuum Models and Discrete Systems.* Paris: Mines ParisTech Les Presses.

DE WIT, R. 1967. Some relations for straight dislocations. *Phys. Stat. Sol.*, **20**(2), 567.

EL-AZAB, A. 2000. Statistical mechanics treatment of the evolution of dislocation distributions in single crystals. *Phys. Rev. B*, **61**(18), 11956 – 11966.

ESHELBY, J.D. 1951. The force on an elastic singularity. *Philos. Trans. R. Soc. Lond., Ser A*, **244**(877), 87–112.

FARRELL, P.A., HEGARTY, A.F., MILLER, J.J.H., O'RIORDAN, E., & SHISHKIN, G.I. 2000. *Robust Computational Techinques for Boundary Layers*. Vol. 16 (Applied Mathematics). Chapman & Hall.

FIVEL, M., VERDIER, M., & GANOVA, G. 1997. 3D simulation of a nanoindentation test at a mesoscopic scale. *Mat. Sci. Eng. A*, **234-236**, 923–926.

FLECK, NA, MULLER, GM, ASHBY, MF, & HUTCHINSON, JW. 1994. Strain gradient plasticity - theory and experiment. *Acta Metall. et Mater.*, **42**(2), 475–487.

GAO, H, HUANG, Y, & NIX, WD ET AL. 1999. Mechanism-based strain gradient plasticity I. Theory. *J. Mech. and Phys. Solids*, **47**, 1239–1263.

GAO, HUAJIAN, & HUANG, YONGGANG. 2003. Geometrically necessary dislocation and size-dependent plasticity. *Scripta Mater.*, **48**(2), 113 – 118.

GHONIEM, NASR M., & SUN, L. Z. 1999. Fast-sum method for the elastic field of three-dimensional dislocation ensembles. *Phys. Rev. B*, **60**(1), 128–140.

GROMA, I. 1997. Link between the microscopic and mesoscopic length-scale description of the collective behavior of dislocations. *Phys. Rev. B*, **56**(10), 5807–5813.

GROMA, I., CSIKOR, F.F., & ZAISER, M. 2003. Spatial correlations and higher-order gradient terms in a continuum description of dislocation dynamics. *Acta Mater.*, **51**, 1271–1281.

GURTIN, MORTON E. 2002. A gradient theory of single-crystal viscoplasticity that accounts for geometrically necessary dislocations. *J. Mech. Phys. Sol.*, **50**(1), 5 – 32.

HARTEN, A. 1987. Uniformly high order accurate essentially non-oscillatory schemes, III. *J. Comput. Phys.*, **71**(2), 231–303.

HIRTH, J.P., & LOTHE, J. (eds). 1982. *Theory of Dislocations*. Krieger Publishing Company.

HOCHRAINER, T. 2006. *Evolving systems of curved dislocations: Mathematical foundations of a statistical theory*. Ph.D. thesis, University of Karlsruhe, IZBS.

HOCHRAINER, T., ZAISER, M., & GUMBSCH, P. 2007. A three-dimensional continuum theory of dislocation systems: kinematics and mean-field formulation. *Phil. Mag.*, **87**(8-9), 1261–1282.

HOCHRAINER, T., ZAISER, M., & GUMBSCH, P. 2009. Dislocation Transport and Line Length Increase in Averaged Descriptions of Dislocations. *AIP Conference Proceedings*, **1168**(1), 1133–1136.

HOCHRAINER, T., SANDFELD, S., ZAISER, M., & GUMBSCH, P. 2010. Dislocation transport and line length increase in averaged descriptions of dislocations. *in preparation*.

HULL, D., & BACON, D. J. 2002. *Introduction to dislocations*. Butterworth Heinemann.

KONDO, K. 1952. On the geometrical and physical foundations of the theory of yielding. *Proc. 2. Japan Nat. Congress of Appl. Mech.*, 41–47.

KOSEVICH, A.M. 1979. The Elastic Theory. *Dislocations in Solids*, **1**, 33–141.

KRATOCHVÍL, JAN, & SEDLÁČEK, RADAN. 2008. Statistical foundation of continuum dislocation plasticity. *Phys. Rev. B*, **77**(13), 134102.

KRÖNER, E. 1980. *Continuum theory of defects*. North Holland publishing company, Amsterdam - New York - Oxford.

KRÖNER, E. 2001. Benefits and shortcomings of the continuous theory of dislocations. *Int. J. Sol. Struct.*, **38**, 1115–1134.

KRÖNER, EKKEHART. 1958. *Kontinuumstheorie der Versetzungen und Eigenspannungen*. Springer.

KUBIN, L. P., & MORTENSEN, A. 2003. Geometrically necessary dislocations and strain-gradient plasticity: a few critical issues. *Scripta Mater.*, **48**(2), 119 – 125.

KUBIN, LP, & CANOVA, G. 1992. The Modeling of Dislocation Patterns. *Scripta Metall. Mater.*, **27**(8), 957–962.

LEMARCHAND, C. 1999. *De la dynamique des dislocations a la mechanique des milieux continus: developpement et application d'une simulation micro-macro*. Ph.D. thesis, l'Universite Pierre et Marie Curie.

LEMARCHAND, C., DEVINCRE, B., & KUBIN, L. P. 2001. Homogenization method for a discrete-continuum simulation of dislocation dynamics. *J. Mech. Phys. Sol.*, **49**(9), 1969 – 1982.

LOVE, A. E. H. 1927. *The Mathematical Theory of Elasticity*. Cambridge University Press.

MA, A., ROTERS, F., & RAABE, D. 2006. A dislocation density based constitutive model for crystal plasticity FEM including geometrically necessary dislocations. *Acta Mater.*, **54**(8), 2169 – 2179.

MIGUEL, M.-CARMEN, VESPIGNANI, ALESSANDRO, ZAISER, MICHAEL, & ZAPPERI, STEFANO. 2002. Dislocation Jamming and Andrade Creep. *Phys. Rev. Lett.*, **89**(16), 165501.

MIGUEL, M. CARMEN, LAURSON, L., & ALAVA, M. J. 2008. Material yielding and irreversible deformation mediated by dislocation motion. *Europ. Phys. J. B*, **64**(3-4), 443–450.

MIGUEL, MC, VESPIGNANI, A, ZAPPERI, S, WEISS, J, & GRASSO, JR. 2001. Intermittent dislocation flow in viscoplastic deformation. *Nature*, **410**(6829), 667–671.

MORTON, KEITH W. 1996. *Numerical solution of convection diffusion problems*. 1st edn. Chapman & Hall.

NIKITAS, N. 2008 (February). *Dislocation-based continuum models of crystal plasticity on the micron scale*. Ph.D. thesis, The University of Edinburgh.

NIX, W. D., & GAO, H. 1998. Indentation size effects in crystalline materials: A law for strain gradient plasticity. *Journal of the Mechanics and Physics of Solids*, **46**(3), 411–425.

NYE, J.F. 1953. Some geometrical relations in dislocated crystals. *Acta Metall.*, **1**, 153–162.

OROWAN, E. 1934. Zur Kristallplastizität. *Z. Phys.*, **89**, 605–659.

POLANYI, M. 1934. Über eine Art Gitterstörung, die einen Kristall plastisch machen könnte. *Z. Phys.*, **89**, 660–664.

ROY, ANISH, & ACHARYA, AMIT. 2004. Finite element approximation of field dislocation mechanics. *J. Mech. and Phys. Solids*, **53**(1), 143–170.

SANDFELD, S., ZAISER, M., & HOCHRAINER, T. 2009a. Expansion of Quasi-Discrete Dislocation Loops in the Context of a 3D Continuum Theory of Curved Dislocations. *AIP Conference Proceedings*, **1168**(1), 1148–1151.

SANDFELD, S., HOCHRAINER, T., ZAISER, M., & GUMBSCH, P. 2010. Numerical Implementation of a 3D Continuum Theory of Dislocation Dynamics and Application to Microbending. *Phil. Mag.* accepted for publication.

SANDFELD, STEFAN, ZAISER, MICHAEL, & HOCHRAINER, THOMAS. 2009b. Application of a 3D-Continuum Theory of Dislocations to Problems of Constrained Plastic Flow: Microbending of a Thin Film. *Mater. Res. Soc. Symp. Proc.*, **1224**.

SCHWARZ, C., SEDLÁČEK, R., KREMPASZKY, C., & WERNER, E. 2007. Dislocation-based modeling of size effects in microscale plasticity. *PAMM*, **7**, 4080003 – 4080004. Proceedings of the GAMM Annual Meeting 2007, Zürich.

SCHWARZ, CORNELIA. 2007. *Numerical implementation of continuum dislocation-based plasticity.* Ph.D. thesis, Lehrstuhl für Werkstoffkunde und Werkstoffmechanik mit Materialprüfamt für den Maschinenbau, Technische Universität München.

SEDLÁČEK, R. 2004. Curved dislocations in continuum crystal plasticity (Professorial dissertation). *TU München.*

SEDLÁČEK, R. 2005a. Bending of thin crystalline strips: Comparison of continuum dislocation-based models. *Mater. Sci. Eng. A*, **400-401**, 439–442.

SEDLÁČEK, R. 2005b. Orowan-type size effect in plastic bending of free-standing thin crystalline strips. *Mater. Sci. Eng. A*, **393**, 387–395.

SEDLÁČEK, R., KRATOCHVÍL, J., & WERNER, E. 2003. The importance of being curved: bowing dislocations in a continuum description. *Phil. Mag.*, **83**(31-34), 3735–3752.

SEDLÁČEK, RADAN, & WERNER, EWALD. 2004. Constrained shearing of a thin crystalline strip: Application of a continuum dislocation-based model. *Phys. Rev. B*, **69**(13), 134114.

STOLKEN, J.S., & EVANS, A.G. 1998. A microbend test method for measuring the plasticity length scale. *Acta Materialia*, **46**, 5109–5115.

STRIKWERDA, JOHN C. 2004. *Finite difference schemes and partial differential equations.* 2nd edn. SIAM.

Taylor, G.I. 1934. The mechanism of plastic deformation of crystals. *Proceedings of the Royal Society of London. Series A, Mathematical and Physical Sciences*, **145**, 362–415.

Van der Giessen, E., & Needleman, A. 1995. Discrete dislocation plasticity: a simple planar model. *Modelling Simul. Mater. Sci. Eng.*, **3**, 689–735.

Varadhan, S. N., Beaudoin, A.J., Acharya, A., & Fressengeas, C. 2006. Dislocation transport using an explicit Galerkin/least-squares formulation. *Modelling Simul. Mater. Sci. Eng.*, **14**, 1245–1270.

Verdier, M., Fivel, M., & Groma, I. 1998. Mesoscopic scale simulation of dislocation dynamics in fcc metals: Principles and applications. *Model. Simul. Mater. Sci. Eng.*, **6**, 755–770.

Volterra, V. 1907. Sur L'equilibre des corps elastiques multiplement connex‘es. *Ann. Ec.norm. (Ser.3)*, **24**, 401–517.

von Mises, R. 1913. Mechanik der Festen Körper im plastisch deformablen Zustand. *Göttin. Nachr. Math. Phys.*, **1**, 582–592.

Weertmann, Johannes, & Weertman, Julia R. 1982. *Elementary Dislocation Theorie.* Oxford University Press, New York - Oxford.

Weinberger, C., Cai, W., & Barnett, D. 2005 (Sept.). *Lecture Notes - Elasticity of Microscopic Structures.* `http://micro.stanford.edu/~caiwei/me340b/content/me340b-notes_v01.pdf`.

Weygand, D., Friedman, L. H., van der Giessen, E., & Needleman, A. 2002. Aspects of boundary-value problem solutions with three-dimensional dislocation dynamics. *Modelling Simul. Mater. Sci. Eng.*, **10**, 437–468.

Yang, Daoqi. 2001. *C++ and object-oriented numeric computing for scientists and engineers.* Springer.

Yefimov, S, Van der Giessen, E, & Groma, I. 2004. Bending of a single crystal: discrete dislocation and nonlocal crystal plasticity simulations. *Modelling Simul. Mater. Sci. Eng.*, **12**, 1069–1086.

Zaiser, M, & Aifantis, E. 2003. Geometrically necessary dislocations and strain gradient plasticity a dislocation dynamics point of view. *Scripta Mater.*, **48**, 133–199.

Zaiser, M, & Hochrainer, T. 2006. Some steps towards a continuum representation of 3D dislocation systems. *Scripta Mater.*, **54**(5), 717–721.

Zaiser, M., & Moretti, P. 2005. Fluctuation phenomena in crystal plasticity - a continuum model. *J. Stat. Mech.*, P08004.

Zaiser, M., Miguel, M.-C., & Groma, I. 2001. Statistical dynamics of dislocation systems: The influence of dislocation-dislocation correlations. *Phys. Rev. B*, **64**(Nov), 224102.

Zaiser, M., Nikitas, N., Hochrainer, T., & Aifantis, E.C. 2007. Modelling size effects using 3D density-based dislocation dynamics. *Phil. Mag.*, **87**, 1283–1306.

ZAISER, MICHAEL, & SEEGER, ALFRED. 2002. Chapter 56 Long-range internal stresses, dislocation patterning and work-hardening in crystal plasticity. Dislocations in Solids, vol. 11. Elsevier.